2005

Electromagnetic methods for measuring material properties of cylindrical rods and array probes for rapid flaw inspection

Haiyan Sun
Iowa State University

Electromagnetic methods for measuring material properties of cylindrical rods and array probes for rapid flaw inspection

by

Haiyan Sun

A dissertation submitted to the graduate faculty

in partial fulfillment of the requirements for the degree of

DOCTOR OF PHILOSOPHY

Major: Electrical Engineering (Electromagnetics) and (Microelectronics)

Program of Study Committee:
John Bowler, Major Professor
Nicola Bowler
David Hsu
Marcus Johnson
Ronald Roberts
Gary Tuttle

Iowa State University

Ames, Iowa

2005

Graduate College
Iowa State University

This is to certify that the doctoral dissertation of

Haiyan Sun

has met the dissertation requirements of Iowa State University

Signature was redacted for privacy.

Major Professor

Signature was redacted for privacy.

For the Major Program

To my son Jeffrey Xuzhi Chen and my husband Feng Chen

TABLE OF CONTENTS

LIST OF TABLES vii

LIST OF FIGURES viii

ABSTRACT xiv

CHAPTER 1. ALTERNATING CURRENT POTENTIAL DROP ON A CONDUCTING CYLINDRICAL ROD 1

1.1 Introduction 1

1.2 Review of potential drop method and alternating current field measurement 2

1.2.1 DCPD 3

1.2.2 ACPD 4

1.2.3 Alternating current field measurement (ACFM) 5

1.3 Alternating current potential drop (ACPD) theory for homogeneous cylindrical rods 6

1.4 ACPD theory for two-layer cylindrical rods 8

1.5 ACPD theory for three-layer cylindrical rods 13

1.6 Comparison for the different ACPD models 17

1.7 Application: using ACPD models to evaluate case hardened steel rods 25

1.8 ACPD experiment on cylindrical rods 27

1.8.1 Conductivity measurements 27

1.8.2 Multi-frequency measurements on homogeneous steel rods 29

1.8.3 Multifrequency ACPD measurements on casehardened steel rods . . . 30

1.9 Improvements on the ACPD experimental system 30

1.10 Conclusions 31
1.11 Future work 32
CHAPTER 2. EDDY CURRENTS INDUCED IN A FINITE LENGTH LAYERED ROD BY A COAXIAL COIL 34
2.1 Introduction 34
2.2 Magnetic vector potential 35
2.2.1 Odd parity solution 37
2.2.2 Even parity solution 41
2.3 Impedance 43
2.4 Tube 44
2.5 Eigenvalue calculations 45
2.6 Results 45
2.7 Discussion of the system equations 48
2.8 Conclusion 51
2.9 Future Work 52
CHAPTER 3. HALL SENSOR ARRAY AND CRACK DETECTION: EXPERIMENT AND SYSTEM 53
3.1 Introduction 53
3.2 Hall effect and Hall sensors 54
3.3 Hall sensor fabrication and testing 57
3.3.1 Fabrication of Hall sensors 57
3.3.2 Testing of the Hall sensors 60
3.4 Eight-element linear Hall array probe 63
3.4.1 Probe design 63
3.4.2 System and electric hardware design 65
3.4.3 Test results 68
3.5 High density linear Hall array probe 71

3.5.1 Design of the Hall sensor arrays 71
3.5.2 Probe design 74
3.5.3 Circuit system design 75
3.5.4 Modulation of Hall signal 83
3.6 Conclusion 86
3.7 Future work 86
APPENDIX A. EDDY CURRENT MEASUREMENTS ON CASE HARDENED STEEL 87
APPENDIX B. ALTERNATING CURRENT POTENTIAL DROP ON A CONDUCTING ROD AND ITS USE FOR EVALUATION OF CASE HARDENED STEEL RODS 101
BIBLIOGRAPHY 118
ACKNOWLEDGEMENTS 128

LIST OF TABLES

Table 1.1 Conductivity of a copper rod measured at low frequency using the ACPD measurement system. 28

Table 1.2 Conductivity of a soft steel rod measured at low frequency using the ACPD measurement system. 28

Table 2.1 Coil and rod parameters that are the same for Figure 2.2 (Aluminum tube) and Figure 2.3 (two-layer steel rod). 47

Table 2.2 Coil and rod parameters that are different for Figure 2.2 (Aluminum tube) and Figure 2.3 (two-layer steel rod). 48

Table 3.1 Parameters for some commercial available Hall sensors. 58

Table 3.2 Measurement results for Hall sensors VDP1 and VDP2. 60

Table 3.3 Dimensions of the racetrack coil. 65

Table 3.4 Characteristics of the P2 Hall sensors. 72

Table B.1 Measured dimensions of six cylindrical rods. The last four rows are for case hardened steel rods with nominal case depth of 0.5mm, 1.0mm, 1.5mm and 2.0mm respectively. 113

Table B.2 Surface layer parameters found by data fitting between ACPD measurements and theoretical models. Their substrate parameters are fixed at $\sigma_1 = 4.84\text{MS/m}, \mu_{r1} = 64.2$. Effective case depth d_e is obtained from the hardness profile 116

LIST OF FIGURES

Figure 1.1 Arrangement of a potential drop system. 3

Figure 1.2 Schematic diagram of the four-point ACPD measurement system. . . 8

Figure 1.3 Cross-sectional diagram of a three-layer rod. 9

Figure 1.4 Electromagnetic property profiles for induction hardened steel. Reprint with permission by Marcus Johnson. 13

Figure 1.5 Cross-sectional diagram of a three-layer rod. 14

Figure 1.6 Comparison of different ACPD models (real part) for two rods (rod 1 and rod 2) with different layer depths. Conductivity and permeability for both rods are the same. The radius for the inner layer in the two-layer model is equal to the smaller interface radius, r_1, in the three-layer model. Curves are normalized by dividing by the real part of the impedance of a homogeneous rod with radius 5.5 mm, conductivity $\sigma_1 = 4.9$ MS/m and relative permeability $\mu_{r1} = 65$. 21

Figure 1.7 Comparison of different ACPD models (imaginary part) for two rods (rod 1 and rod 2) with different layer depths. Conductivity and permeability for both rods are the same. The radius for the inner layer in the two-layer model is equal to the smaller interface radius, r_1, in the three-layer model. Curves are normalized by dividing by the imaginary part of the impedance of a homogeneous rod with radius 5.5 mm, conductivity $\sigma_1 = 4.9$ MS/m and relative permeability $\mu_{r1} = 65$. 22

Figure 1.8 Comparison of different ACPD models (real part) for two rods (rod 1 and rod 2) with different layer depths. Conductivity and permeability for both rods are the same. The radius for the inner layer in the two-layer model is equal to the larger interface radius, r_2, in the three-layer model. Curves are normalized by dividing by the real part of the impedance of a homogeneous rod with radius 5.5 mm, conductivity $\sigma_1 = 4.9$ MS/m and relative permeability $\mu_{r1} = 65$. . . 23

Figure 1.9 Comparison of different ACPD models (imaginary part) for two rods (rod 1 and rod 2) with different layer depths. Conductivity and permeability for both rods are the same. The radius for the inner layer in the two-layer model is equal to the larger interface radius, r_2, in the three-layer model. Curves are normalized by dividing by the imaginary part of the impedance of a homogeneous rod with radius 5.5 mm, conductivity $\sigma_1 = 4.9$ MS/m and relative permeability $\mu_{r1} = 65$. 24

Figure 1.10 Comparison between theory prediction and experimental data for the multi-frequency ACPD measurements on a homogenous steel rod to determine its relative permeability. 29

Figure 2.1 Coil coaxial with a two-layer finite rod. 36

Figure 2.2 Normalized coil resistance (left) and reactance (right) variation with position due to the the two-layer steel rod at 1kHz: comparison between TREE method (solid line) and FEMLAB result (solid circles). 46

Figure 2.3 Normalized coil resistance (top) and reactance (bottom) variation with position due to the short aluminum tube at 1kHz: comparison between TREE method (solid line) and FEMLAB result (solid circles). 47

Figure 2.4 Normalized coil impedance variation with frequency (6.3 Hz — 1995.3 Hz) due to the two-layer steel rods with different outer layer depths of 0 mm, 2 mm, and 4 mm respectively. The coil center is placed at the end of the rod. 49

Figure 2.5 Normalized coil impedance variation with frequency (584 Hz to 858 Hz) due to the two-layer steel rods with different outer layer depths of 0 mm, 2 mm, and 4 mm respectively. The coil center is placed at the end of the rod. 50

Figure 3.1 Diagram illustrating the Hall effect in a p-type sample. 54

Figure 3.2 (a) Bridge-type Hall sample, (b) lamella-type van der Pauw Hall sample. 57

Figure 3.3 Basic photolithography process. 59

Figure 3.4 Van der Pauw Hall sensor made of GaAs square. 60

Figure 3.5 Relation between Hall voltage and magnetic flux density for Hall sensor VDP1 and VDP2. 61

Figure 3.6 Linear array probe with racetrack coil and eight Hall sensors. 63

Figure 3.7 Picture of the racetrack coil. 64

Figure 3.8 Picture showing the PCB with 8 HW105A Hall sensors mounted on its edge. 64

Figure 3.9 Diagram of the test system for the eight-element Hall sensor array probe. 66

Figure 3.10 Zero crossing detector circuit schematic. 67

Figure 3.11 Ramp generator circuit schematic. 68

Figure 3.12 Ramp signal (A) and probe signal (C) when the probe was placed along the radius of a circular coil. X-axis is time with a grid of 0.2 second. Y-axis is the signal level. The grid for the ramp signal (C) is 50 mV and the grid for the probe signal is 2V. 69

Figure 3.13 Signal displayed on the screen of the oscilloscope when the array probe is placed on an aluminum plate with a long EDM slot. The lowest step represents the location of the slot. 70

Figure 3.14 Epitaxial structure of the Hall effect sensor (P2) 72

Figure 3.15 Part of the design for a 2-inch wafer, which contains 16- element Hall arrays connecting in series or parallel in the central region and some individual Hall sensors near the boarder. 73

Figure 3.16 Geometries of the Hall sensor arrays. The dimensions shown in the figure are $a = 400\mu m$, $b = 90\mu m$, $c = 70\mu m$, $d = 80\mu m$, $e = 50\mu m$, $f = 100\mu m$, $W = 70\mu m$, $L = 210\mu m$. Note that the tracks connecting between sensors are not shown. 74

Figure 3.17 A printed circuit board (PCB) with a long slot in the center. To minimize pick-up voltages in the track loops, pairs of copper tracks associated with an individual Hall sensor are routed directly opposite one another on two different layers. 76

Figure 3.18 Dimensions for two Hall arrays in the PCB slot. The two Hall arrays, each having 16 Hall sensors, are wire bounded with the pads on the PCB. Note that connections between Hall sensors are not shown in the figure. 77

Figure 3.19 Different coils and Hall sensor array arrangements. 78

Figure 3.20 Block diagram of the Hall array circuit system. 78

Figure 3.21 Block diagram of the detector circuit for one channel. 79

Figure 3.22 Schematic for one channel of Hall signal processing circuit which consists of input amplifier, phase demodulator, low pass filter and sample/hold circuit. 80

Figure 3.23 Schematic diagram for the sample and hold circuit. 81

Figure 3.24 Illustration of modulation and demodulation of Hall signal in frequency domain. (a) Hall signal together with induction signal, (b) reference signal at 68 kHz, (c) output signal from the multiplier (AD633), where the reference signal is multiplied by the Hall signal, (d) low pass filter with -3dB frequency at 50 Hz, (e) output signal from the low pass filter. After demodulation, only DC signal remains which represents the level of the upper sideband of the modulated Hall signal while the induction signal is removed. 85

Figure A.1 Schematic diagram of the four-point conductivity measurement system. 91

Figure A.2 Comparison between theory and experiment for eddy-current impedance measurements on a copper rod with conductivity $\sigma = 58.6$ MS/m. . 94

Figure A.3 Comparison between theory and experiment for eddy-current impedance measurements on a soft steel rod with conductivity $\sigma = 3.9$ MS/m and relative permeability 70. 96

Figure A.4 Comparison between theory and experiment for eddy-current impedance measurements on a case-hardened steel rod. The theoretical curves shown here are obtained by fixing the conductivity and permeability values of the substrate to be the same as those found for the soft steel rod (FIGURE 3). The thickness, permeability and conductivity of the layer are then adjusted to obtain the best fit to the experimental data, as shown. 97

Figure A.5 Root mean square error between experimental and calculated values of coil resistance and reactance as a function of layer depth, for fixed conductivity and permeability values in the steel substrate and case-hardened layer. 98

Figure B.1 Schematic diagram of the four-point ACPD measurement system. . . 109

Figure B.2 Comparison between theory and the ACPD measurements on a copper rod with conductivity of 58.4MS/m. 110

Figure B.3 Comparison between theory and the ACPD measurements on a homogeneous steel rod with $\sigma = 4.84$MS/m and $\mu_r = 70$ determined by data fitting of theoretical model predictions to multi-frequency ACPD measurements. 112

Figure B.4 Hardness profile of the four case hardened steel rods. 113

Figure B.5 Real part of experimental data and theoretical fit curve for case hardened steel rods. Numbers in the legend are the nominal case depth in mm. 114

Figure B.6 Imaginary part of experimental data and theoretical curve fit by using real part of experimental data for case hardened steel rods. Numbers in the legend are the nominal case depth in mm. 115

ABSTRACT

The case-hardening process modifies the near-surface permeability and conductivity of steel, as can be observed through changes in alternating current potential drop (ACPD) along a rod. In order to evaluate case depth of case hardened steel rods, analytical expressions are derived for the alternating current potential drop on the surface of a homogeneous rod, a two-layered and a three-layered rod. The case-hardened rod is first modeled by a two-layer rod that has a homogeneous substrate with a single, uniformly thick, homogeneous surface layer, in which the conductivity and permeability values differ from those in the substrate. By fitting model results to multi-frequency ACPD experimental data, estimates of conductivity, permeability and case depth are found. Although the estimated case depth by the two-layer model is in reasonable agreement with the effective case depth from the hardness profile, it is consistently higher than the effective case depth. This led to the development of the three-layer model. It is anticipated that the new three-layered model will improve the results and thus makes the ACPD method a novel technique in nondestructive measurement of case depth.

Another way to evaluate case depth of a case hardened steel rod is to use induction coils. Integral form solutions for an infinite rod encircled by a coaxial coil are well known, but for a finite length conductor, additional boundary conditions must be satisfied at the ends. In this work, calculations of eddy currents are performed for a two-layer conducting rod of finite length excited by a coaxial circular coil carrying an alternating current. The solution is found using the truncated region eigenfunction expansion (TREE) method. By truncating the solution region to a finite length in the axial direction, the magnetic vector

potential can be expressed as a series expansion of orthogonal eigenfunctions instead of as a Fourier integral. Closed-form expressions are derived for the electromagnetic field in the presence of a finite a two-layer rod and a conductive tube. The results are in very good agreement with those obtained by using a 2D finite element code.

In the third part, a new probe technology with enhanced flaw detection capability is described. The new probe can reduce inspection time through the use of multiple Hall sensors. A prototype Hall array probe has been built and tested with eight individual Hall sensor ICs and a racetrack coil. Electronic hardware was developed to interface the probes to an oscilloscope or an eddy current instrument. To achieve high spatial resolution and to limit the overall probe size, high-sensitivity Hall sensor arrays were fabricated directly on a wafer using photolithographic techniques and then mounted in their unencapsulated form. The electronic hardware was then updated to interface the new probes to a laptop computer.

CHAPTER 1. ALTERNATING CURRENT POTENTIAL DROP ON A CONDUCTING CYLINDRICAL ROD

1.1 Introduction

Alternating current potential drop (ACPD) is usually used for crack measurements. A review of this topic will be given in the next section. In this chapter, however, an ACPD method is described for estimating electromagnetic properties of conducting cylindrical rods.

The alternating current can only be carried in the surface layer of a conducting material, a phenomenon usually called "skin effect". The penetration depth is determined by the skin depth δ,

$$\delta = \frac{1}{\sqrt{\pi \mu \sigma f}} \tag{1.1}$$

where f is the excitation frequency, σ is the electrical conductivity of the conductor and μ is its magnetic permeability. The skin depth varies with frequency, causing changes in the electrical field distribution and the potential drop on the specimen surface. Thus, by making multi-frequency ACPD measurements and comparing the experimental data with theoretical predictions, material properties can be assessed. When applied on case hardened steel, the ACPD measurements provide a way to estimate case depth, which is of great practical value for quality control of surface-hardened steel products.

Section 1.2 is a brief review of potential-drop and alternating-current-field-measurement methods. In sections 1.3 — 1.5, analytical ACPD models are developed for homogeneous, two-layer and three-layer cylindrical rods respectively. Electrical field intensity distribution

in the rods, and the potential drop on the rod surface are derived by solving boundary value problems. Section 1.6 compares the three different models and shows their relations with each other. Section 1.7 shows how to evaluate case hardened steel rods using ACPD models. In section 1.8, the design of an experiment system is described for taking multi-frequency ACPD measurements on cylindrical rods. Results are given for copper and untreated steel rods. Strategies are explained for estimating the case depth of hardened steel rods from multi-frequency ACPD data and a model-based inversion technique. Improvements on the ACPD experimental system are mentioned in section 1.9. Conclusions and suggestions for future work are given in sections 1.10 and 1.11.

1.2 Review of potential drop method and alternating current field measurement

Potential drop method is a nondestructive testing method often used for wall thickness measurements or crack measurements. Basically, there are two types of potential drop technique: one is direct current potential drop (DCPD), the other is alternating current potential drop (ACPD). Figure 1.1 shows the basic experimental arrangement for either DCPD or ACPD measurements. Contacts are made to the metal through four electrodes, A_1, A_2, B_1, B_2. Current I is passed through the metal by a current source, between current electrodes A_1 and A_2. In DCPD, I is a direct current. In ACPD, I is an alternating current. The potential V between electrodes B_1 and B_2 is measured using a potentiometer. Changes in the V/I ratio are used to determine wall thickness or size and position of cracks. The distance and configuration for the electrodes vary for different applications. The potential drop method is extensively used for cracks measurements. A review of research in this area is given below.

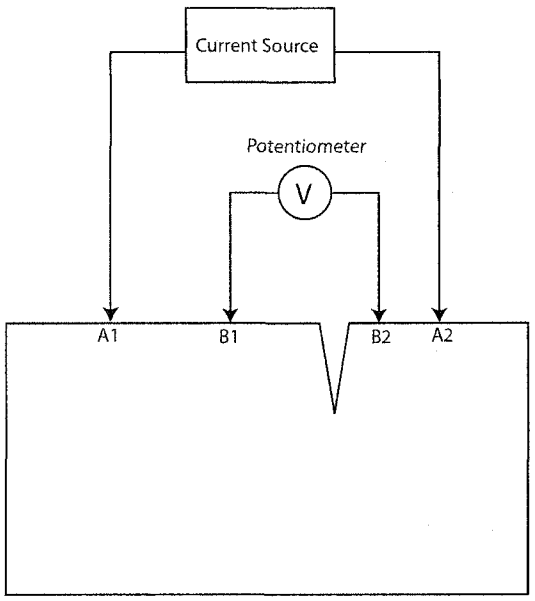

Figure 1.1 Arrangement of a potential drop system.

1.2.1 DCPD

The procedure of measuring cracks using the DCPD method is briefly described here. First, apply current I and measure the potential V_{normal} in the area remote from the crack. Then place the electrodes centrally over the crack, balance out the thermal electromotive force and measure V_{crack} by using the same current I as before. Finally, obtain crack depth from the ratio of the two potentials $V_{\text{crack}}/V_{\text{normal}}$.

The advantages of the DCPD method over the ACPD method include: easier to derive analytical expressions for the potential drop for various configurations of electrodes, different shapes and dimensions of a specimen; easier to interpret measurement data; stable, reproducible and insensitive to movements of cables and no inductive pick up due to the connecting cables [1]. For these reasons, the DCPD technique has interested a number of researchers [2–6].

In order to obtain a good sensitivity for small changes in the crack size, the traditional

DCPD method involves the application of a large uniform direct current to set up a uniform electric field throughout the material volume. However, this will cause specimen heating, a safety problem and the need for expensive precision high-capacity current source. Other problems in DCPD include thermal electromotive forces and contact voltages of the electrodes. To address these problems, instead of using constant direct current, pulse current or rapid reversal current can be used to reduce sample heating and remove both thermal and contact voltage [7]. Another approach is called closely coupled probes potential drop (CCPPD) technique [8–10]. This technique places the input current leads close to the crack plane, thus concentrating the electric field created into this region and achieving the same sensitivity with a smaller input current.

Another technique similar to DCPD is called the Four-point probe method, which uses DC current to measure resistivity of a metal or semiconductor material [11–15]. It is usually applied on rectangular solids or circular disks. Recent research also extends this method to cylindrical materials [16].

1.2.2 ACPD

ACPD applies alternating current to a conducting specimen to establish a uniform thin-skin electric field on the surface of the specimen. Unlike a direct current which is transmitted through the entire volume of a specimen, an alternating current is carried only in a thin layer at the surface whose depth is given by equation (1.1). Therefore, the ACPD technique is more sensitive to surface breaking cracks than its DC counterpart. The depth of penetration of the AC fields into the metal is determined by the electromagnetic "skin depth", which is a function of the AC frequency, magnetic permeability and conductivity of the material. A lot of research work has been carried out to investigate the ACPD method in crack measurements [17–25].

In practice, comparisons are made between measured voltages and predicted voltages from models, allowing estimation of crack depth and shape without calibration. In cases

where the material is homogeneous and the electric field remains uniform on the specimen surface and the crack faces, the crack depth can be calculated using a simple one-dimensional calculation [17]. Non-uniformity of the electric field can lead to errors. Improvements in both probe design and theoretical interpretation have been made which allow for correction of field non-uniformity [17, 18]. More elaborate models than the simple one-dimensional model have been used successfully to measure crack depth in a transition weld [19].

ACPD system is subject to inductive pick up voltage caused by the connecting cables. The pickup voltage increases linearly with the frequency of the supply current. Compared with DCPD, ACPD requires lower measuring current to be applied for a given sensitivity. It is easier to design instrumentation for ACPD because it is easier to measure a small alternating voltage and achieve a high signal to noise ratio. Alternating current measurements inherently require that the crack be open and that the test contacts be applied on the cracked surface. Direct current measurements can, in principle, be used to detect cracks or voids that are not connected to the surface being tested but the interpretation of the measurements can be very complex.

1.2.3 Alternating current field measurement (ACFM)

One of the limitations of both the DCPD and the ACPD techniques is the requirement of good electrical contact with the metal surface by the pick-up points, which is not always easy to achieve. This led to the development of alternating current field measurement (ACFM), a non-contacting technique. The ACFM technique involves inducing a locally uniform current into a test object and measuring the magnetic flux density above the test object surface with nonconducting coils. The presence of a surface breaking discontinuity perturbs the induced current and the magnetic flux density. Mapping of the perturbation of this magnetic field provides an alternative means of measuring crack depth and crack length without the requirement for a contacting probe. The large perturbation of the magnetic field that occurs at the end of a defect also allows this method to be used for crack detection.

Therefore ACFM offers the capability of both detection and sizing of surface breaking defects without the need for calibration and without the requirement for cleaning the metal surface [24, 26]. The ACFM technique has been used in different areas to detect cracks and size surface breaking defects in a wide range of structural materials [27–32].

1.3 Alternating current potential drop (ACPD) theory for homogeneous cylindrical rods

Suppose an alternating current is applied along an infinitely long cylindrical rod with a radius a. The current varies sinusoidally with time as the real part of $e^{\jmath\omega t}$. The electromagnetic field inside the rod is governed by Maxwell's equations, which in the quasi-static limit, i.e., in the limit of negligible displacement current, can be written as:

$$\nabla \times \mathbf{H} = \mathbf{J} \tag{1.2}$$

$$\nabla \times \mathbf{E} = -\frac{\partial \mathbf{B}}{\partial t}. \tag{1.3}$$

In addition, Ohm's Law can be written as

$$\mathbf{J} = \sigma \mathbf{E}. \tag{1.4}$$

It is assumed that there exists linear isotropic constitutive relation $\mathbf{B} = \mu\mathbf{H}$. In these equations, μ and σ are the magnetic permeability and electrical conductivity of the metal rod respectively. Equations (1.2), (1.3) and (1.4) can be used to give the following equation for $\mathbf{E}$

$$\nabla \times \nabla \times \mathbf{E} = -\mu\sigma \frac{\partial \mathbf{E}}{\partial t}. \tag{1.5}$$

Note $\nabla \times \nabla \times \mathbf{E} = \nabla(\nabla \cdot \mathbf{E}) - \nabla^2\mathbf{E}$. Since there are no free charges in the rod, $\nabla \cdot \mathbf{E} = 0$. Using the fact that $\mathbf{E}$ varies with time t as $e^{\jmath\omega t}$, (1.5) can be written as

$$\nabla^2\mathbf{E} = \jmath\omega\mu\sigma\mathbf{E} = -k^2\mathbf{E} \tag{1.6}$$

where $k^2 = -\jmath\omega\mu\sigma$, $k = (1-\jmath)/\delta$ and δ is the electromagnetic skin depth defined as $\delta = \sqrt{2/(\omega\mu\sigma)}$. Due to the symmetry of the rod, $\mathbf{E}$ is a function of radial coordinate ρ only. Putting $\mathbf{E} = \hat{z}E(\rho, k)$, equation (1.6) gives

$$\frac{\partial^2 E}{\partial \rho^2} + \frac{1}{\rho}\frac{\partial E}{\partial \rho} + k^2 E = 0. \tag{1.7}$$

This is a modified form of the equation for the zeroth order Bessel function. By applying the boundary condition on the rod surface that $E = E_0$ where $\rho = a$, equation (1.7) has the following solution:

$$E(\rho, k) = E_0 J_0(k\rho)/J_0(ka). \tag{1.8}$$

The total current passing through the rod can be expressed as

$$I = 2\pi\sigma \int_0^a E(\rho, k)\rho \, d\rho. \tag{1.9}$$

Using equation (1.8) and the following integration

$$\int_0^a J_0(k\rho)\rho \, d\rho = \frac{a}{k} J_1(ka). \tag{1.10}$$

Equation (1.9) gives

$$I = \frac{2\pi\sigma \, aE_0}{kJ_0(ka)} J_1(ka). \tag{1.11}$$

Hence the surface electric field is related to the total current by

$$E_0(k) = \frac{kIJ_0(ka)}{2\pi\sigma \, aJ_1(ka)}. \tag{1.12}$$

Letting l be the length measured along the rod between the two contact points of the voltage electrodes (shown in Figure 1.2), the potential drop between these two points is given by

$$V(k) = E_0(k)l = \frac{klIJ_0(ka)}{2\pi\sigma \, aJ_1(ka)}. \tag{1.13}$$

The measured voltage includes a contribution from the electromotive force (emf) induced in the voltage measurement circuit due to changing of magnetic flux linking this circuit. Expressing the induced emf V_{ind} in terms of the self inductance L, where L is defined as $L = \frac{V_{ind}}{\jmath\omega I}$, the total voltage, V_T, sensed across a length l of the rod is

$$V_{\text{T}} = \frac{klIJ_0(ka)}{2\pi\sigma \, aJ_1(ka)} + \jmath\omega LI. \tag{1.14}$$

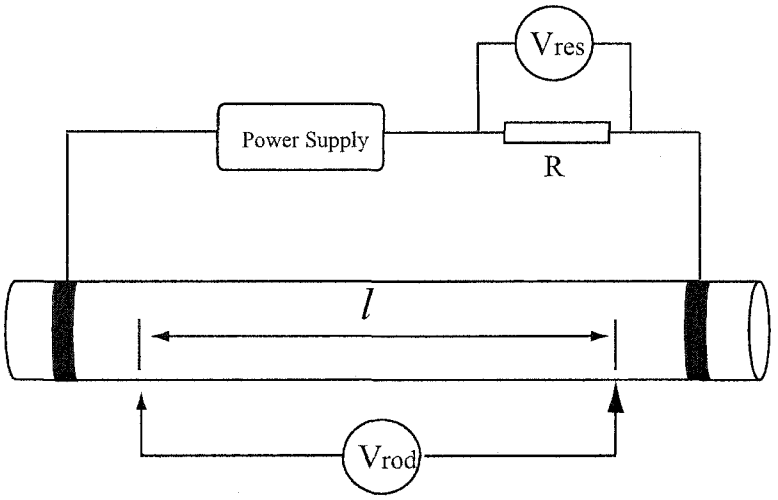

Figure 1.2 Schematic diagram of the four-point ACPD measurement system.

The rod impedance is defined as

$$Z_{\text{rod}} = \frac{klJ_0(ka)}{2\pi\sigma\, aJ_1(ka)} + j\omega L. \tag{1.15}$$

Equation (1.15) can be used to estimate material properties of a homogeneous rod from multi-frequency potential drop measurements.

1.4 ACPD theory for two-layer cylindrical rods

Consider a two-layered cylindrical rod with outer radius b and inner radius a, Figure 1.3. The conductivity and relative permeability are σ_2, and μ_2 in its outer layer, σ_1, and μ_1 in the inner layer. Using a cylindrical polar coordinate system, putting the axis of the rod as z direction, one can define the coordinates of ρ and ϕ consequently.

When applying an alternating current down the axis of the case hardened steel rod (z direction), the electric field intensity in the rod is governed by equations similar to (1.7),

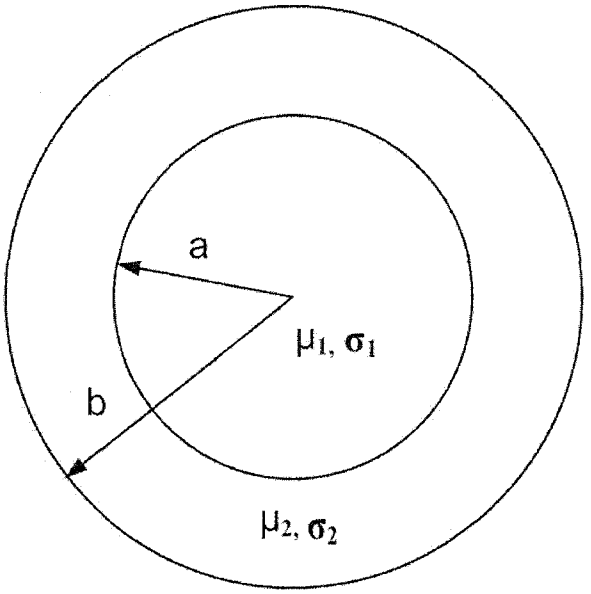

Figure 1.3 Cross-sectional diagram of a three-layer rod.

with different conductivity and permeability for the two regions:

$$\frac{\partial^2 E_1}{\partial \rho^2} + \frac{1}{\rho}\frac{\partial E_1}{\partial \rho} + k_1^2 E_1 = 0 \qquad (0 \le \rho \le a) \tag{1.16}$$

$$\frac{\partial^2 E_2}{\partial \rho^2} + \frac{1}{\rho}\frac{\partial E_2}{\partial \rho} + k_2^2 E_2 = 0 \qquad (a \le \rho \le b), \tag{1.17}$$

where k_1, k_2 are given by $k_i^2 = -\jmath\omega\mu_i\sigma_i$ for $i = 1, 2$. Note that E_1 and E_2 are both in the z direction. The solution to equation (1.16) can be borrowed from equation (1.8),

$$E_1(\rho, k) = AE_0 J_0(k_1\rho). \tag{1.18}$$

Because Bessel function $Y_0(k_2\rho)$ goes to infinity while ρ goes to zero, it is not included in the solution (1.18). But it is necessary to include it in the solution to the equation (1.17) for the surface layer:

$$E_2(\rho, k) = E_0[BJ_0(k_2\rho) + CY_0(k_2\rho)]. \tag{1.19}$$

Note that A, B, C above are coefficients to be determined by the following boundary conditions.

First, assuming the electric field intensity on the rod surface is E_0, i.e. $E_2 = E_0$ when $\rho = b$, gives

$$BJ_0(k_2b) + CY_0(k_2b) = 1. \tag{1.20}$$

Next, the tangential part of electric fields are continuous on $\rho = a$, hence

$$BJ_0(k_2a) + CY_0(k_2a) = AJ_0(k_1a). \tag{1.21}$$

Third, from

$$\nabla \times \mathbf{E} = -\frac{\partial E}{\partial \rho}\hat{\phi}, \tag{1.22}$$

and

$$\nabla \times \mathbf{E} = -\jmath\omega\mu H_\phi \hat{\phi} \tag{1.23}$$

and the fact that the tangential part of magnetic field intensity is continuous at $\rho = a$, one can get

$$\frac{1}{\mu_1}\frac{\partial E_1}{\partial \rho} = \frac{1}{\mu_2}\frac{\partial E_2}{\partial \rho}. \tag{1.24}$$

From (1.18) and (1.19),

$$\frac{\partial E_1}{\partial \rho} = -E_0 A k_1 J_1(k_1\rho), \tag{1.25}$$

and

$$\frac{\partial E_2}{\partial \rho} = -E_0 k_2 [BJ_1(k_2\rho) + CY_1(k_2\rho)], \tag{1.26}$$

thus the third interface condition is given by,

$$B\mu_1 k_2 J_1(k_2a) + C\mu_1 k_2 Y_1(k_2a) = A\mu_2 k_1 J_1(k_1a). \tag{1.27}$$

The coefficients A, B, C can now be obtained from equations (1.20), (1.21), and (1.27). It is found that

$$A = \Delta_A/\Delta, \qquad B = \Delta_B/\Delta, \qquad C = \Delta_C/\Delta \tag{1.28}$$

where

$$\Delta_A = \mu_1 k_2 [J_1(k_2a)Y_0(k_2a) - Y_1(k_2a)J_0(k_2a)] \tag{1.29}$$

$$\Delta_B = -\mu_1 k_2 Y_1(k_2a)J_0(k_1a) + \mu_2 k_1 J_1(k_1a)Y_0(k_2a) \tag{1.30}$$

$$\Delta_C = -\mu_2 k_1 J_1(k_1 a) J_0(k_2 a) + \mu_1 k_2 J_0(k_1 a) J_1(k_2 a) \tag{1.31}$$

and

$$\begin{aligned} \Delta &= -\mu_1 k_2 J_0(k_1 a) J_0(k_2 b) Y_1(k_2 a) - \mu_2 k_1 J_1(k_1 a) J_0(k_2 a) Y_0(k_2 b) \\ &\quad + \mu_2 k_1 J_1(k_1 a) J_0(k_2 b) Y_0(k_2 a) + \mu_1 k_2 J_1(k_2 a) Y_0(k_2 b) J_0(k_1 a) \qquad (1.32) \\ &= J_0(K_2 b)\Delta_B + Y_0(k_2 b)\Delta_C. \qquad (1.33) \end{aligned}$$

A better way to solve the problem is to express B and C in terms of A from (1.21) and (1.27), then substitute the expressions for B and C into (1.20) to solve for A. The following Wronskian relation is useful to simplify expressions,

$$J_1(z) Y_0(z) - J_0(z) Y_1(z) = \frac{2}{\pi z}. \tag{1.34}$$

Multiply both sides of (1.27) with $Y_0(k_2 a)$ and (1.21) with $\mu_1 k_2 Y_1(k_2 a)$ and subtract them, use Wronskian relation (1.34) to simplify the results, one gets

$$B = \frac{\pi a}{2\mu_1} P A \tag{1.35}$$

where

$$P = \mu_2 k_1 J_1(k_1 a) Y_0(k_2 a) - \mu_1 k_2 J_0(k_1 a) Y_1(k_2 a). \tag{1.36}$$

Similarly, multiply both sides of (1.21) with $\mu_1 k_2 J_1(k_2 a)$ and (1.27) with $J_0(k_2 a)$ and subtract them to give

$$C = \frac{\pi a}{2\mu_1} Q A \tag{1.37}$$

where

$$Q = \mu_1 k_2 J_0(k_1 a) J_1(k_2 a) - \mu_2 k_1 J_1(k_1 a) J_0(k_2 a). \tag{1.38}$$

The Wronskian relation (1.34) has been used again. Substitute (1.35) and (1.37) into (1.20) to solve for A, one has

$$A = \frac{2\mu_1}{\pi a [P J_0(k_2 b) + Q Y_0(k_2 b)]}. \tag{1.39}$$

Thus, the coefficients A, B and C are expressed as (1.35) — (1.39), which are simpler compared with expressions in (1.28) — (1.33). The electric field density inside the rod is

given by (1.18) and (1.19). The potential drop along the rod can be derived as follows. Express the current in the rod as

$$I = 2\pi\sigma_1 \int_0^a E_1(\rho)\rho\, d\rho + 2\pi\sigma_2 \int_a^b E_2(\rho)\rho\, d\rho. \tag{1.40}$$

Substitute equations (1.18) and (1.19) into (1.40) to get

$$\frac{I}{E_0} = 2\pi\sigma_1 A \int_0^a J_0(k_1\rho)\rho\, d\rho + 2\pi\sigma_2 B \int_a^b J_0(k_2\rho)\rho\, d\rho + 2\pi\sigma_2 C \int_a^b Y_0(k_2\rho)\rho\, d\rho. \tag{1.41}$$

Use the result of the following integration

$$\int_0^a xY_0(x)dx = aY_1(a) + \frac{2}{\pi}, \tag{1.42}$$

one can easily get

$$\int_0^a Y_0(k\rho)\rho\, d\rho = \frac{aY_1(ka)}{k} + \frac{2}{k^2\pi}. \tag{1.43}$$

Using (1.10) and (1.43) to integrate (1.41), one has

$$\frac{I}{E_0} = 2\pi\sigma_1 AaJ_1(k_1a)/k_1 + 2\pi\sigma_2 B[bJ_1(k_2b) - aJ_1(k_2a)]/k_2 + 2\pi\sigma_2 C[bY_1(k_2b) - aY_1(k_2a)]/k_2. \tag{1.44}$$

Rearrange the above equation to give the electric field intensity on the surface of the rod:

$$E_0 = \frac{I}{2\pi\sigma_1 AaJ_1(k_1a)/k_1 + 2\pi\sigma_2 B[bJ_1(k_2b) - aJ_1(k_2a)]/k_2 + 2\pi\sigma_2 C[bY_1(k_2b) - aY_1(k_2a)]/k_2}. \tag{1.45}$$

Thus the potential drop including the induced emf is

$$V_T = E_0 l + \jmath\omega LI, \tag{1.46}$$

where l and L are defined in the same way as in equation (1.15). The rod impedance is defined as

$$Z_{\text{rod}} = \frac{E_0 l}{I} + \jmath\omega L \tag{1.47}$$

with E_0 given by equation (1.45).

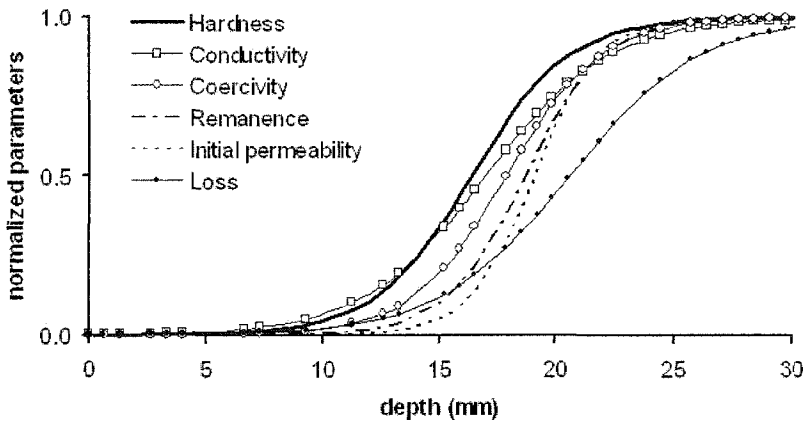

Figure 1.4 Electromagnetic property profiles for induction hardened steel. Reprint with permission by Marcus Johnson.

1.5 ACPD theory for three-layer cylindrical rods

Recent research by Marcus Johnson [34] shows that conductivity and permeability profiles of an induction-hardened steel rod are different from its hardness profile. Normalized curves in Figure 1.4 [34] show clearly how the depth dependence of the individual electrical and magnetic parameters is different from that of the hardness. The electrical conductivity appears to track hardness fairly well but the initial permeability significantly lags behind the specimen's hardness profile, which contributes to over estimation of the case depth measurements based on the two layer model [34]. If the material property profile in Figure 1.4 is represented by a piecewise constant approximation, the breakpoint in permeability is evidently at a deeper position than that in conductivity. A three layer ACPD model is thus developed to incorporate the difference between conductivity and permeability profiles. The parameters for each layer are shown in Figure 1.5. Note that the breakpoint for relative permeability is at $\rho = r_1$, whereas the breakpoint for conductivity is at $\rho = r_2$, where $r_2 > r_1$. The electric field intensity in the rod is governed by

$$\frac{\partial^2 E_1}{\partial \rho^2} + \frac{1}{\rho}\frac{\partial E_1}{\partial \rho} + k_1^2 E_1 = 0 \qquad (0 \le \rho \le r_1) \tag{1.48}$$

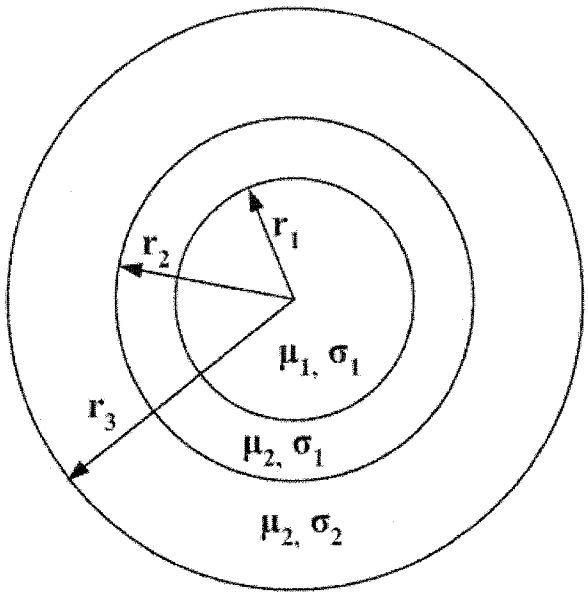

Figure 1.5 Cross-sectional diagram of a three-layer rod.

$$\frac{\partial^2 E_2}{\partial \rho^2} + \frac{1}{\rho}\frac{\partial E_2}{\partial \rho} + k_2^2 E_2 = 0 \qquad (r_1 \le \rho \le r_2) \tag{1.49}$$

$$\frac{\partial^2 E_3}{\partial \rho^2} + \frac{1}{\rho}\frac{\partial E_3}{\partial \rho} + k_3^2 E_3 = 0 \qquad (r_2 \le \rho \le r_3) \tag{1.50}$$

where $k_1^2 = -j\omega\mu_1\sigma_1$, $k_2^2 = -j\omega\mu_2\sigma_1$ and $k_3^2 = -j\omega\mu_2\sigma_2$. The solutions can be written as

$$E_1(\rho, k) = E_0 B_1 J_0(k_1\rho) \tag{1.51}$$

$$E_2(\rho, k) = E_0[B_2 J_0(k_2\rho) + C_2 Y_0(k_2\rho)] \tag{1.52}$$

$$E_3(\rho, k) = E_0[B_3 J_0(k_3\rho) + C_3 Y_0(k_3\rho)] \tag{1.53}$$

where B_1, B_2, C_2, B_3 and C_3 are the unknown coefficients to be determined from boundary/interface conditions. The interface conditions at $\rho = r_1$ are

$$E_1|_{\rho=r_1} = E_2|_{\rho=r_1} \qquad \frac{1}{\mu_1}\frac{\partial E_1}{\partial \rho}|_{\rho=r_1} = \frac{1}{\mu_2}\frac{\partial E_2}{\partial \rho}|_{\rho=r_1}. \tag{1.54}$$

The interface conditions at $\rho = r_2$ are

$$E_2|_{\rho=r_2} = E_3|_{\rho=r_2} \qquad \frac{\partial E_2}{\partial \rho}|_{\rho=r_2} = \frac{\partial E_3}{\partial \rho}|_{\rho=r_2}. \tag{1.55}$$

Substitute equations (1.51) - (1.53) into interface conditions (1.54) - (1.55) to give

$$B_1 J_0(k_1 r_1) = B_2 J_0(k_2 r_1) + C_2 Y_0(k_2 r_1) \tag{1.56}$$

$$B_1 \mu_2 k_1 J_1(k_1 r_1) = B_2 \mu_1 k_2 J_1(k_2 r_1) + C_2 \mu_1 k_2 Y_1(k_2 r_1) \tag{1.57}$$

$$B_2 J_0(k_2 r_2) + C_2 Y_0(k_2 r_2) = B_3 J_0(k_3 r_2) + C_3 Y_0(k_3 r_2) \tag{1.58}$$

$$B_2 k_2 J_1(k_2 r_2) + C_2 k_2 Y_1(k_2 r_2) = B_3 k_3 J_1(k_3 r_2) + C_3 k_3 Y_1(k_3 r_2). \tag{1.59}$$

Assuming the electric field intensity is E_0 at the rod surface ($\rho = r_3$), one gets the following boundary condition from equation (1.53),

$$B_3 J_0(k_3 r_3) + C_3 Y_0(k_3 r_3) = 1. \tag{1.60}$$

The five unknown coefficients can be found from equations (1.56) — (1.60) using a recursive method. First express B_2 and C_2 in terms of B_1 using equation (1.56) and (1.57). Next express B_3 and C_3 in terms of B_2 and C_2 from equation (1.58) and (1.59). Finally, substitute B_3 and C_3 in terms of B_1 into (1.60) to solve for B_1. Once B_1 is known, the other coefficients can be worked out recursively. A similar approach was used in [43].

Multiply both sides of (1.57) with $Y_0(k_2 r_1)$ and (1.56) with $\mu_1 k_2 Y_1(k_2 r_1)$ and subtract them, one gets

$$[\mu_2 k_1 J_1(k_1 r_1) Y_0(k_2 r_1) - \mu_1 k_2 J_0(k_1 r_1) Y_1(k_2 r_1)] B_1 = \mu_1 k_2 [J_1(k_2 r_1) Y_0(k_2 r_1) - J_0(k_2 r_1) Y_1(k_2 r_1)] B_2. \tag{1.61}$$

Simplify the right-hand side using the Wronskian relation (1.34) and define

$$P = \mu_2 k_1 J_1(k_1 r_1) Y_0(k_2 r_1) - \mu_1 k_2 J_0(k_1 r_1) Y_1(k_2 r_1). \tag{1.62}$$

Equation (1.61) becomes

$$B_2 = \frac{\pi r_1}{2\mu_1} P B_1. \tag{1.63}$$

Similarly, multiply both sides of (1.57) with $J_0(k_2 r_1)$ and (1.56) with $\mu_1 k_2 J_1(k_2 r_1)$ and subtract them, one gets

$$C_2 = \frac{\pi r_1}{2\mu_1} Q B_1 \tag{1.64}$$

where the Wronskian relation is used and

$$Q = \mu_1 k_2 J_1(k_2 r_1) J_0(k_1 r_1) - \mu_2 k_1 J_1(k_1 r_1) J_0(k_2 r_1). \tag{1.65}$$

Multiply both sides of (1.59) with $Y_0(k_3 r_1)$ and (1.58) with $k_3 Y_1(k_3 r_1)$ and subtract them, one gets

$$R_1 B_2 + S_1 C_2 = \frac{2}{\pi r_2} B_3 \tag{1.66}$$

where

$$R_1 = k_2 J_1(k_2 r_2) Y_0(k_3 r_2) - k_3 J_0(k_2 r_2) Y_1(k_3 r_2) \tag{1.67}$$

and

$$S_1 = k_2 Y_1(k_2 r_2) Y_0(k_3 r_2) - k_3 Y_0(k_2 r_2) Y_1(k_3 r_2). \tag{1.68}$$

Multiply both sides of (1.59) with $J_0(k_3 r_2)$ and (1.58) with $k_3 J_1(k_3 r_2)$ and subtract them, one gets

$$R_2 B_2 + S_2 C_2 = \frac{2}{\pi r_2} C_3 \tag{1.69}$$

where

$$R_2 = k_3 J_0(k_2 r_2) J_1(k_3 r_2) - k_2 J_1(k_2 r_2) J_0(K_3 r_2) \tag{1.70}$$

and

$$S_2 = k_3 Y_0(k_2 r_2) J_1(k_3 r_2) - k_2 Y_1(k_2 r_2) J_0(k_3 r_2). \tag{1.71}$$

Note that Wronskian relation is used in deriving equations (1.66) and (1.69). From equations (1.66) and (1.69), one can express B_3 and C_3 in terms of B_2 and C_2 in a matrix form

$$\begin{bmatrix} B_3 \\ C_3 \end{bmatrix} = \frac{\pi r_2}{2} \begin{bmatrix} R_1 & S_1 \\ R_2 & S_2 \end{bmatrix} \begin{bmatrix} B_2 \\ C_2 \end{bmatrix}. \tag{1.72}$$

Substitute equations (1.63) and (1.64) into (1.72) to give

$$\begin{bmatrix} B_3 \\ C_3 \end{bmatrix} = \frac{\pi^2 r_2 r_1}{4\mu_1} \begin{bmatrix} R_1 P + S_1 Q \\ R_2 P + S_2 Q \end{bmatrix} B_1. \tag{1.73}$$

Substitute equation (1.73) into equation (1.60), one can solve for B_1,

$$B_1 = \frac{4\mu_1}{\pi^2 r_2 r_1[(R_1P + S_1Q)J_0(k_3r_3) + (R_2P + S_2Q)Y_0(k_3r_3)]}. \tag{1.74}$$

The current along the rod can be written as

$$I = 2\pi\sigma_1 \int_0^{r_1} E_1(\rho)\rho\, d\rho + 2\pi\sigma_1 \int_{r_1}^{r_2} E_2(\rho)\rho\, d\rho + 2\pi\sigma_2 \int_{r_2}^{r_3} E_3(\rho)\rho\, d\rho. \tag{1.75}$$

Substitute equations (1.51)-(1.53) into (1.75), after integrating and rearranging the results, the electric field intensity in the rod is expressed as

$$E_0 = \frac{I}{2\pi[\frac{B_1\sigma_1 r_1}{k_1}J_1(k_1r_1) + \frac{B_2\sigma_1}{k_2}T_1 + \frac{C_2\sigma_1}{k_2}T_2 + \frac{B_3\sigma_2}{k_3}T_3 + \frac{C_3\sigma_2}{k_3}T_4]} \tag{1.76}$$

where

$$T_1 = r_2J_1(k_2r_2) - r_1J_1(k_2r_1) \tag{1.77}$$

$$T_2 = r_2Y_1(k_2r_2) - r_1Y_1(k_2r_1) \tag{1.78}$$

$$T_3 = r_3J_1(k_3r_3) - r_2J_1(k_3r_2) \tag{1.79}$$

$$T_4 = r_3Y_1(k_3r_3) - r_2Y_1(k_3r_2). \tag{1.80}$$

The voltage drop along the rod including the induced emf is

$$V_T = E_0 l + j\omega LI \tag{1.81}$$

where l and L are defined in the same way as in equation (1.15). The rod impedance can be defined the same as equation (1.47).

1.6 Comparison for the different ACPD models

The three ACPD models are related to each other. With a few modifications, the three-layer model can be simplified to the two-layer model, and the two-layer model can be reduced to the homogeneous one.

There are different ways to simplify three-layer model to the two layer model. First, let's change the conductivity in the middle layer to σ_2 in the three-layer model. Thus the

middle and outer layer have the same parameters. As a result, some of the equations in Section 1.6 can be simplified. Substitute $k_2 = k_3$ into equations (1.67), (1.68), (1.70) and (1.71), one gets

$$S_1 = R_2 = 0 \tag{1.82}$$

$$R_1 = S_2 = \frac{2}{\pi r_2}. \tag{1.83}$$

Substitute (1.82), (1.83) and $k_2 = k_3$ into equations (1.66), (1.69) and (1.74) to get

$$B_1 = \frac{2\mu_1}{\pi r_1[PJ_0(k_3r_3) + QY_0(k_3r_3)]} \tag{1.84}$$

$$B_3 = B_2 \quad \text{and} \quad \mathrm{C}_3 = \mathrm{C2}. \tag{1.85}$$

Substitute (1.85) into (1.52) and (1.53), one has

$$E_2 = E_3. \tag{1.86}$$

Thus the electrical field are the same in the middle layer and the outer layer. This is straightforward since the conductivity and the permeability are set the same in both layers.

Comparing expressions in (1.62) --- (1.65) and (1.84) with the expressions in (1.35) — (1.39), one finds that the coefficients A, B, C in the two-layer model are the same as the coefficients B_1, B_2, B_3 in the three-layer model provided that $b = r_3$ and $a = r_1$. Thus the three-layer model is simplified to the two-layer model.

Another way to compare the two-layer and three-layer model is to set $r_2 = r_1$ in the three-layer model. Replacing r_2 by r_1 in equations (1.56)—(1.60), one gets

$$B_1J_0(k_1r_1) = B_2J_0(k_2r_1) + C_2Y_0(k_2r_1) \tag{1.87}$$

$$B_1\mu_2k_1J_1(k_1r_1) = B_2\mu_1k_2J_1(k_2r_1) + C_2\mu_1k_2Y_1(k_2r_1) \tag{1.88}$$

$$B_2J_0(k_2r_2) + C_2Y_0(k_2r_2) = B_3J_0(k_3r_1) + C_3Y_0(k_3r_1) \tag{1.89}$$

$$B_2k_2J_1(k_2r_1) + C_2k_2Y_1(k_2r_1) = B_3k_3J_1(k_3r_1) + C_3k_3Y_1(k_3r_1) \tag{1.90}$$

and

$$B_3J_0(k_3r_3) + C_3Y_0(k_3r_3) = 1. \tag{1.91}$$

Note that equations (1.87), (1.88) and (1.91) are the same as equations (1.56), (1.57) and (1.60). Only equations (1.89) and (1.90) have been changed. Since the right hand side of equation (1.87) is the same as the left hand side of equation (1.89), they can be combined to give

$$B_1 J_0(k_1 r_1) = B_3 J_0(k_3 r_1) + C_3 Y_0(k_3 r_1). \tag{1.92}$$

Similarly, equations (1.88) and (1.90) can be combined to give

$$B_1 \mu_2 k_1 J_1(k_1 r_1) = B_3 \mu_1 k_3 J_1(k_3 r_1) + C_3 \mu_1 k_3 Y_1(k_3 r_1). \tag{1.93}$$

Set $r_1 = a$, $r_3 = b$, $B_1 = A$, $B_3 = B$, $C_3 = C$ in equations (1.91), (1.92) and (1.93), and keep in mind that k_3 in the three-layer model is the same as k_2 in the two-layer model since they both represent the outermost layer with σ_2 and μ_{r2}, one finds that these equations are the same as the equations (1.20), (1.21) and (1.27) for the two-layer rod model. Thus the three-layer model can be reduced to the two-layer model by setting $r_2 = r_1$.

The relationship between the two-layer model and the homogeneous one is more obvious. Let the conductivity and the relative permeability be the same in the outer layer and the inner layer, i.e.,

$$\mu_2 = \mu_1 = \mu, \quad \sigma_2 = \sigma_1 = \sigma, \quad k_2 = k_1 = k. \tag{1.94}$$

Substitute (1.94) into (1.35) — (1.39), one gets

$$Q = 0 \tag{1.95}$$

$$P = \frac{2\mu}{\pi a} \tag{1.96}$$

$$C = 0 \tag{1.97}$$

$$B = A = \frac{1}{J_0(kb)} \tag{1.98}$$

$$E_2 = E_1 = \frac{E_0 J_0(k\rho)}{J_0(kb)}. \tag{1.99}$$

Comparing (1.99) and (1.8), one finds they are equivalent.

Another way is to set $a = b$. Thus equation (1.21) becomes

$$B J_0(k_2 b) + C Y_0(k_2 b) = A J_0(k_1 a). \tag{1.100}$$

Note that equation the left hand side of (1.100) and (1.20) are the same. They can be combined to give

$$AJ_0(k_1a) = 1. \tag{1.101}$$

Thus we have

$$A = \frac{1}{J_0(k_1b)}. \tag{1.102}$$

Substitute equation (1.102) into (1.18), we get

$$E_1 = \frac{E_0 J_0(k\rho)}{J_0(kb)} \tag{1.103}$$

which is the same as the equation (1.8) in the homogeneous rod. Since $a = b$, equation (1.103) is the electrical field intensity in both layers.

It seems one can simplify the two-layer model by assigning the parameters of the outer layer to be those of air, i.e., $\sigma_2 = 0$, $\mu_{r2} = 1$. However, in such case, $k_2 = 0$, $Y_0(0) \to -\infty$ and equation (1.19) does not hold. Therefore, this is not a good way to check the relation between two-layer and homogeneous models.

Figures 1.6 — 1.9 show the difference among the ACPD models. Normalized rod impedance is plotted over a range of frequencies for two different three-layer rods (rod 1 and rod 2). Conductivity and relative permeability for both rods are $\sigma_1 = 4.9$ MS/m, $\sigma_2 = 3.6$ MS/m, $\mu_{r1} = 65$, $\mu_{r2} = 41$. These parameters are representative of a typical case-hardened steel rod. Layer radii for rod 1 are $r_1 = 4.2$ mm, $r_2 = 4.5$ mm, $r_3 = 5.5$ mm. For rod 2, they are $r_1 = 3$ mm, $r_2 = 3.5$ mm, $r_3 = 5.5$ mm. In figure 1.6 and 1.7, the inner radius of the two-layer model is selected to be r_1. The outer radius is r_3. In figure 1.8 and 1.9, the inner radius of the two-layer model is selected to be r_2. The outer radius is r_3. The rod impedances are normalized by a homogeneous rod impedance which has a radius of 5.5 mm, conductivity $\sigma_1 = 4.9$ MS/m and relative permeability $\mu_{r1} = 65$.

At very low frequency, the imaginary part of the rod impedance can be neglected and the real part is determined by the conductivity only. Thus at the low frequency limit, the three-layer rod is reduced to a two-layer model because the conductivity has only two

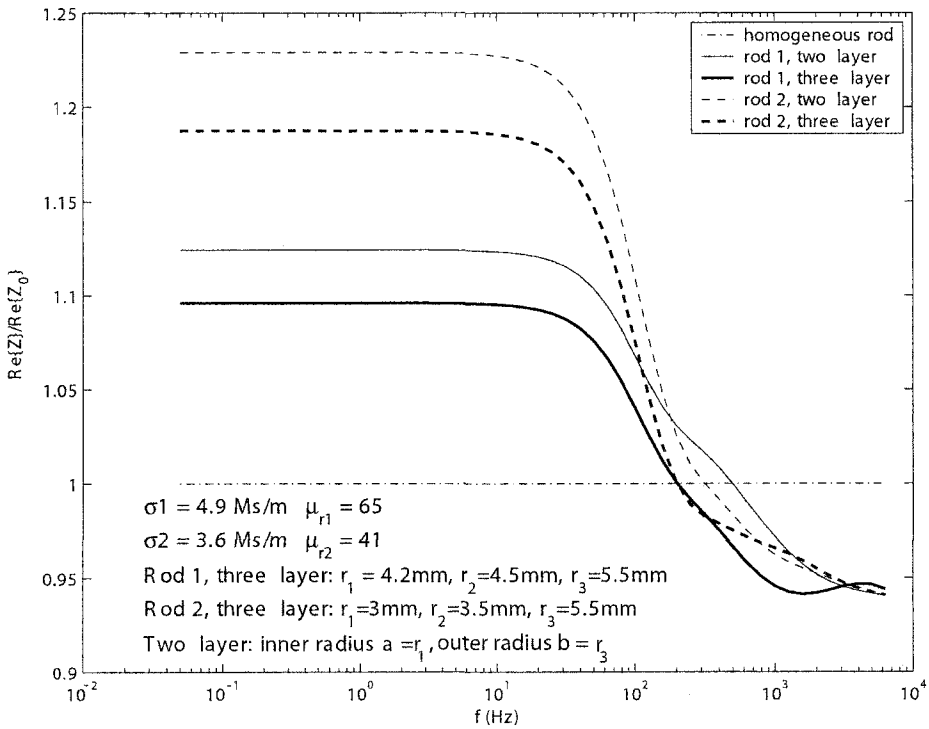

Figure 1.6 Comparison of different ACPD models (real part) for two rods (rod 1 and rod 2) with different layer depths. Conductivity and permeability for both rods are the same. The radius for the inner layer in the two-layer model is equal to the smaller interface radius, r_1, in the three-layer model. Curves are normalized by dividing by the real part of the impedance of a homogeneous rod with radius 5.5 mm, conductivity $\sigma_1 = 4.9$ MS/m and relative permeability $\mu_{r1} = 65$.

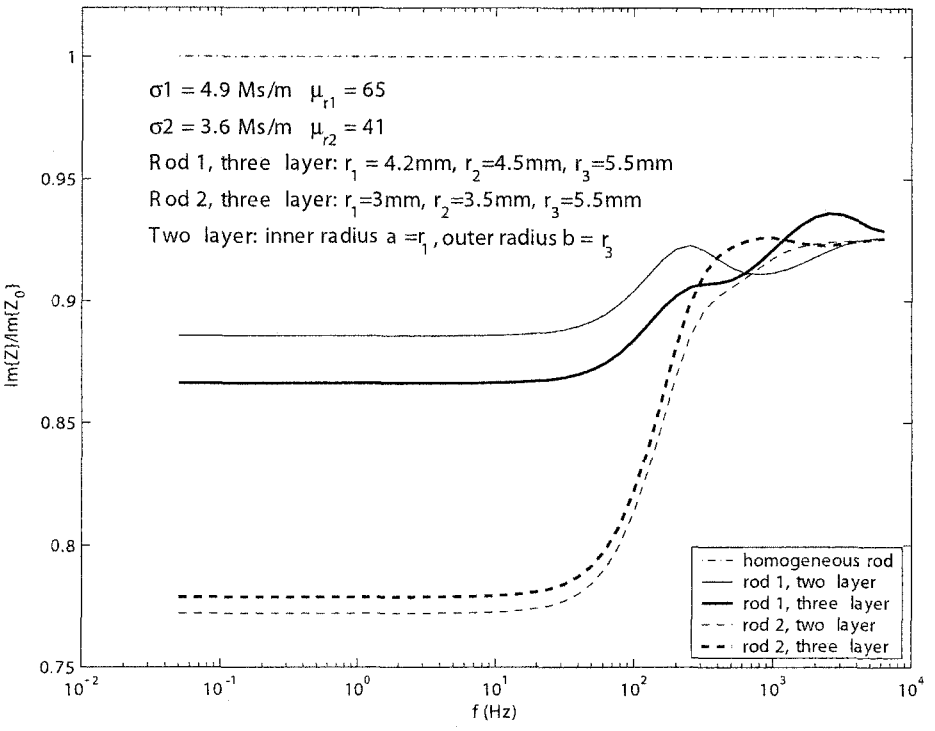

Figure 1.7 Comparison of different ACPD models (imaginary part) for two rods (rod 1 and rod 2) with different layer depths. Conductivity and permeability for both rods are the same. The radius for the inner layer in the two-layer model is equal to the smaller interface radius, r_1, in the three-layer model. Curves are normalized by dividing by the imaginary part of the impedance of a homogeneous rod with radius 5.5 mm, conductivity $\sigma_1 = 4.9$ MS/m and relative permeability $\mu_{r1} = 65$.

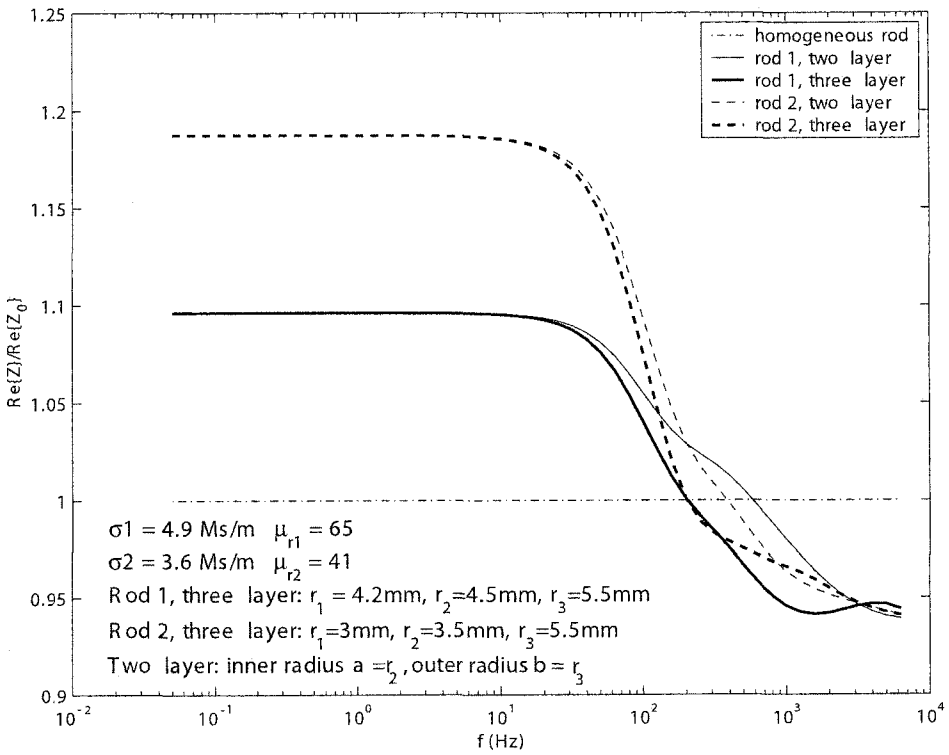

Figure 1.8 Comparison of different ACPD models (real part) for two rods (rod 1 and rod 2) with different layer depths. Conductivity and permeability for both rods are the same. The radius for the inner layer in the two-layer model is equal to the larger interface radius, r_2, in the three-layer model. Curves are normalized by dividing by the real part of the impedance of a homogeneous rod with radius 5.5 mm, conductivity $\sigma_1 = 4.9$ MS/m and relative permeability $\mu_{r1} = 65$.

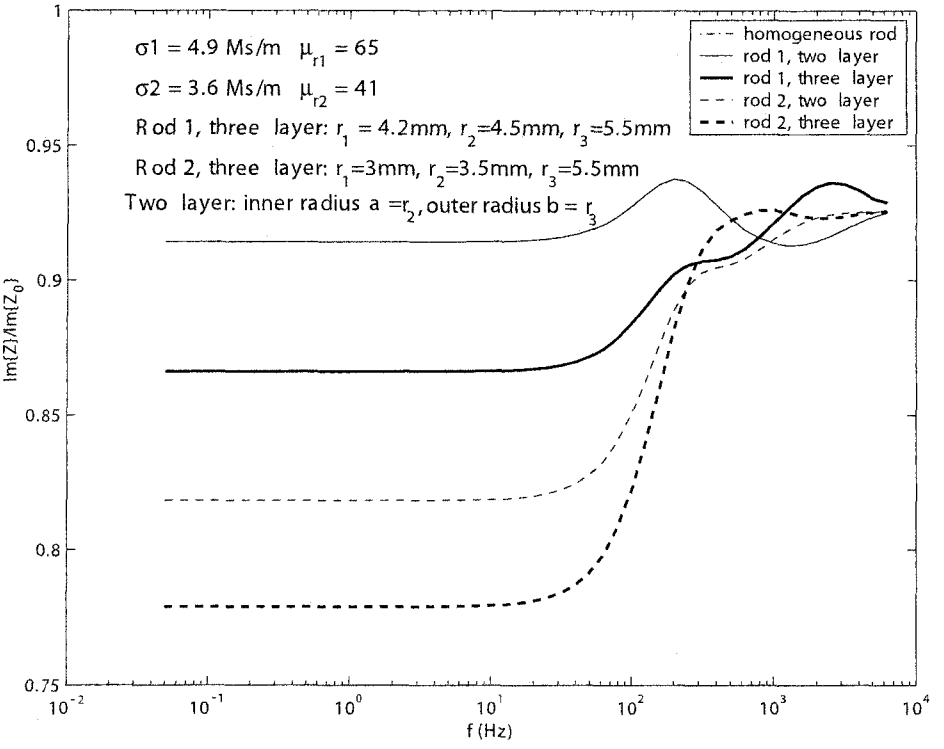

Figure 1.9 Comparison of different ACPD models (imaginary part) for two rods (rod 1 and rod 2) with different layer depths. Conductivity and permeability for both rods are the same. The radius for the inner layer in the two-layer model is equal to the larger interface radius, r_2, in the three-layer model. Curves are normalized by dividing by the imaginary part of the impedance of a homogeneous rod with radius 5.5 mm, conductivity $\sigma_1 = 4.9$ MS/m and relative permeability $\mu_{r1} = 65$.

different values. In this case, the layered rod can be treated as two resistors with different conductivities connected in parallel. Refer to Figure 1.3, at low frequency limit, let R be the total resistance of a layered rod with length l, R_1 be the resistance for the inner layer with conductivity σ_1 and R_2 be the resistance for the inner layer with conductivity σ_2. From

$$\frac{1}{R} = \frac{1}{R_1} + \frac{1}{R_2}, \tag{1.104}$$

it is easy to derive the following equation,

$$R = \frac{l}{\sigma_1 S_1 + \sigma_2 S_2} = \frac{l}{\pi(\sigma_1 - \sigma_2)a^2 + \pi\sigma_2 b^2} \tag{1.105}$$

where a is the radius for inner layer with conductivity σ_1, b is the outer layer radius, S_1 and S_2 are the cross-section area of the two layers, as shown in Figure 1.3. From (1.105), it is obvious that when a increases, the rod resistance R reduces. This is shown in Figure 1.6 and Figure 1.8. In Figure 1.6, the two-layer model gives a higher resistance than the three-layer model the low frequency range. This is because when $a = r_1$, the radius for the region of σ_1 is smaller in the two-layer rod than that of the three-layer model. However, in Figure 1.6, $a = r_2$, which means radius for the region of σ_1 is the same in both two-layer and three-layer models, thus they give the same rod resistance in the low frequency limit.

1.7 Application: using ACPD models to evaluate case hardened steel rods

Case hardening of steel components improves the resistance to wear by changing the carbon content and micro-structure of the surface region. Consequently, the electrical conductivity and magnetic permeability have different values near the surface compared with the substrate values. The required depth of the case-hardened layer varies depending on the purpose for which the steel is needed. Evaluating case depth in steel components is critical for quality control of both new and remanufactured products.

A number of methods have been investigated to to examine the results of case hardening and quantify the effect on components non-destructively [35–41]. Here an alternative approach is presented using the previous developed models and inverse strategy.

Based on the spirit of starting with a basic model and progressing to a more elaborate representation later if necessary, the case hardened steel rod specimens are first modelled as two-layer cylindrical rods with the following assumptions:

1. The breakpoint in electromagnetic properties falls at a point where the hardness is midway between surface and substrate values, which allows the case depth to be estimated from electromagnetic measurements.

2. Cylindrical rod specimens are modelled as uniform in the axial direction having a homogeneous substrate surrounded by a homogeneous surface layer (case hardened layer) of uniform thickness.

3. The process of case hardening does not modify the material properties below the case hardened layer. In other words, the conductivity and permeability of the substrate layer of a case hardened steel rod is the same as that of a non-hardened steel rod.

Under these assumptions, case hardened steel rods can be modelled by the two-layer ACPD theory. There are five unknown parameters in this model: the substrate conductivity σ_1, relative permeability μ_{r1}, the surface conductivity σ_2, relative permeability μ_{r2} and the surface layer depth (case depth) d. They can be determined separately. While details are given in the following section, the main approach is summarized here. First, the conductivity of a non-hardened (homogeneous) rod is obtained by low frequency ACPD measurements. Next, the relative permeability is determined by fitting multi-frequency ACPD measurement data with theoretical predictions from equation (1.15). Based on assumption 2, the conductivity and permeability obtained for the homogeneous rod are the same as those for the inner layer of the case hardened rod (σ_1 and μ_{r1}). Although one can fit both conductivity and permeability from the multi-frequency ACPD measurements, it is better to fit fewer parameters from the same set of data to improve accuracy in the

fitting results. The last step is to take multi-frequency ACPD measurements on the case hardened steel rods. The case depth d, outer layer conductivity σ_2 and permeability μ_{r2} are evaluated by fitting the experimental data to the theoretical expression in equation (1.47). In equation (1.15) or (1.47), there is an extra parameter, the induced emf L. Since it only appears in the imaginary part of the rod impedance, it doesn't need to be determined if we only fit the real part of the experimental data.

1.8 ACPD experiment on cylindrical rods

In this section, the ACPD experiment system is described. Conductivity for a copper rod and homogeneous steel rod were determined by very low frequency ACPD measurements. The relative permeability for the homogeneous rod was obtained using model-based multi-frequency ACPD measurements. The ACPD measurements for case-hardened steel rods can be found in Appendix B and reference [33].

Figure 1.2 shows the schematic diagram of the experimental arrangement for measuring the ACPD on cylindrical rods. A HP 3325B function generator is used to give the desired sinusoidal signal, which is amplified by a KEPCO Bipolar operation power supply/amplifier to provide a constant drive current to the rod. The current is injected into the rod through two copper rings which are kept in close contact with the two ends of the rod. The voltage drop along the rod (V_{rod}) is measured between two points separated by a distance l. A precision resistor ($R_{\text{res}} = 0.0471\Omega$) is connected in series with the rod. The voltage across the resistor (V_{res}) is measured in order to monitor the current through the circuit, $I = V_{\text{res}}/R_{\text{res}}$. Both V_{rod} and V_{res} are measured by a SR830 DSP Lock-in amplifier. A switch is used to toggle between the two measurements.

1.8.1 Conductivity measurements

The conductivity of homogeneous metal rods can be determined independently of other parameters by very low frequency ACPD measurements. At very low frequency, the skin

Table 1.1 Conductivity of a copper rod measured at low frequency using the ACPD measurement system.

frequency (Hz)	V_{rod} (mV)	V_{res} (mV)	conductivity (MS/m)	(% IACS)
0.1	132.23	117.71	58.71	101.23
0.5	132.41	117.70	58.62	101.07
1	132.52	117.67	58.57	100.98

Table 1.2 Conductivity of a soft steel rod measured at low frequency using the ACPD measurement system.

frequency (Hz)	V_{rod} (mV)	V_{res} (mV)	conductivity (MS/m)	(% IACS)
0.05	2.167	117.63	3.902	6.727
0.1	2.168	117.65	3.901	6.725
0.5	2.168	117.63	3.900	6.724

depth is much larger than the diameter of the rod, thus the current density along the radius direction of a homogeneous rod is uniform. As a result, the potential drop in the rod is independent of its permeability and is determined by its conductivity only. Using very low frequency ACPD measurements, the conductivity of a homogeneous rod can be calculated by the following equation

$$\sigma = \frac{S}{R_{\text{rod}} l} = \frac{V_{\text{res}} S}{V_{\text{rod}} R_{\text{res}} l} \tag{1.106}$$

where S is the cross-sectional area of the rod and R_{rod} is the resistance of the rod between two measurement points.

An annealed, unalloyed copper rod, 40 cm long and 11.07 mm in diameter, with a known conductivity of 58.0 MS/m or 100.0% IACS was measured using at 0.1 Hz, 0.5 Hz and 1 Hz (Table 1.1). The measured conductivity is very close to its known conductivity, indicating the accuracy of the experiment system. A soft steel rod, which is not case hardened and considered to be homogeneous, 40 cm long and 11.02 mm in diameter, was also measured using the same system. Results are shown in Table 1.2.

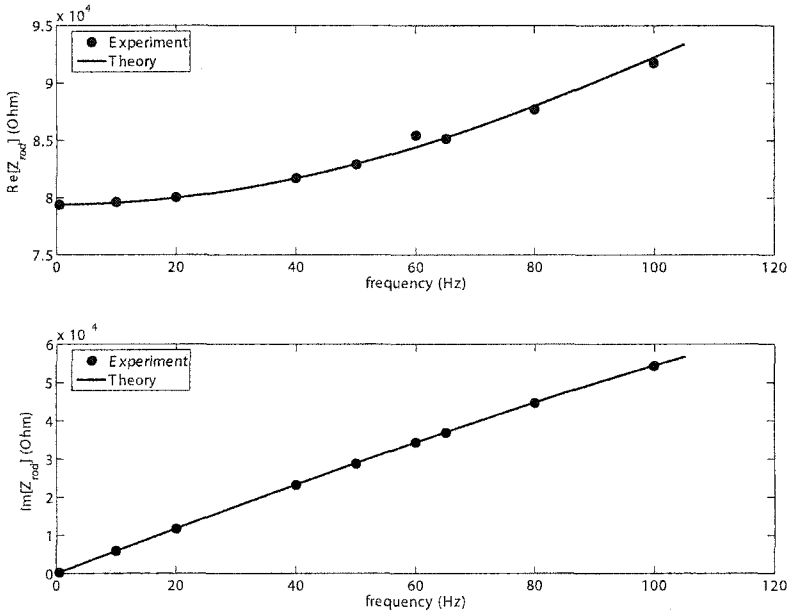

Figure 1.10 Comparison between theory prediction and experimental data for the multi-frequency ACPD measurements on a homogenous steel rod to determine its relative permeability.

1.8.2 Multi-frequency measurements on homogeneous steel rods

With the conductivity determined by low frequency measurements, the permeability of the homogeneous steel rod can be obtained from multi-frequency ACPD measurements by fitting experimental data with the theoretical predictions. As shown in Figure 1.10, ACPD measurements were carried out from 0.5 Hz to 100 Hz. The rod impedance is plotted over frequency. With the conductivity fixed at 3.9 MS/m, experimental curves were fitted with the theoretical model using equation (1.15). The best fitted value for μ_r is 70. In Figure 1.10, amplitude of the rod impedance are used for fitting, therefore, induced emf L was also fitted, whose value was found to be 0.02 μH. To avoid fitting L, one should fit only real part of the data, as mentioned in the previous section. The experimental data in Figure 1.10 were recorded manually. After these initial measurement were taken, the system was controlled automatically as in the Appendix B and in reference [33], more data were collected over a wider frequency range.

1.8.3 Multifrequency ACPD measurements on casehardened steel rods

It is assumed that the process of case hardening does not change the material properties below the case hardened layer. Based on this assumption, the substrate conductivity σ_1 and permeability μ_1 are the same as for the homogenous steel rod. Thus $\sigma_1 = 3.90$ MS/m and $\mu_{r1} = 70$. With the substrate properties held fixed, the electrical conductivity σ_2, permeability μ_{r2} and case depth d of the outer layer can be fitted using equation (1.46).

Multi-frequency ACPD measurements were not carried out using the preliminary system. However, they were performed using an automated system as described in the Appendix B and reference [33].

MATLAB routines were used to perform the fitting procedure using a built-in function in MATLAB, "fminsearch". It is a nonlinear optimization function that can minimize a function of several variables. For the homogeneous rod, the fitting is simple since there is only one free parameter: permeability. For the case hardened steel rod, there are three parameters (d, σ_2, μ_{r2}) to be determined. Because these parameters have quite large difference in their absolute value, they are normalized in order to make the fitting process more accurate, i.e., in the fitting program, they vary in percentage instead of in their absolute values. Initial estimates for the three parameters are given to the function "fminsearch", which will search the parameters in a certain range to find the minimum least mean square (LMS) error between the theoretical model and the experimental data. However, it can only find the local minimum error according to the given initial guess. In order to find the global minimum, the initial guesses for three parameters vary gradually in small steps. By comparing the LMS errors of all the local minimum, the best fitted values for d, σ_2, μ_{r2} are found that give the smallest LMS error.

1.9 Improvements on the ACPD experimental system

In Appendix B and reference [33], an improved ACPD experimental system is described. A computer program was developed to control the system and take multi-frequency mea-

surements automatically. The connections and wiring are carefully designed to minimize the induced emf. New samples are ordered with known hardness profile. A complete discussion of the updated system and more results are given in Appendix B and reference [33].

However, case depths evaluated using the two-layered ACPD model are consistently higher than the effective case-depth obtained from hardness profile. Research results by Marcus Johnson [34] show that the first assumption in Section 1.7 is not accurate. According to [34], the two-layer ACPD model is updated by a three-layer model, as shown in Section 1.5. The three-layer ACPD model can better represent the conductivity and permeability profile of a case-hardened rod. It is expected that fitting the measured data with the three-layered model will improve the accuracy in the evaluation of case depth.

It should be pointed out that fitting with the three-layer model is more complex than the two-layer model because there is one more parameter: radius of the middle layer. However, by using the low-frequency limit in equation (1.105) as a constraint, one can reduce the number of free parameters and improve the overall fitting accuracy.

1.10 Conclusions

In this chapter, analytical models are derived for alternating current potential drop (ACPD) on homogeneous, two-layer and three-layer cylindrical rods. The relationships between different models are discussed. MATLAB programs have been developed to calculate the rod impedance with ACPD method. Comparison for the three ACPD models are given and their difference are illustrated with figures.

The models are applied to evaluate case hardened steel rods. This is a new method to determine the case depth of case hardened steel rods. An experimental system is designed to take ACPD measurements. Measurements are carried out on homogeneous rods. By fitting experimental data with the theoretical model, material conductivity and permeability can be found. Model-based inversion strategies have been explained on how to determine the case depth by measuring the voltage on the rod surface. The data fitting process is

discussed. The case depths evaluated based on two-layer ACPD model are in reasonable agreement with the effective case depths obtained from hardness profile. However, they are consistently higher than the effective case depths. Based on recent advances in the analysis of conductivity and permeability profiles in hardened steel [34], a new three-layer model is developed, which is a better representation of hardened steel rods and gives the hope of improving the accuracy in evaluating case depth with the ACPD method.

1.11 Future work

Research results have clearly shown that the electromagnetic properties do not vary in the same way as the specimen's hardness profile [34]. Therefore, the actual case hardened steel rods are over simplified by the two-layer model. Future work will fit multi-frequency ACPD data with the three-layer model. In order to reduce the overall fitting errors, the low frequency limit should be added to the model as a constraint, as mentioned before. If necessary, the three-layer ACPD model can be expanded to a multi-layer model. However, this will complicate the data fitting procedure.

In the ACPD system designed in section 1.8, alternating current is injected into the rod by two copper rings which are kept in close contact with the two ends of the rod. Voltages are measured at two points between the the current injecting copper rings and are away from them for a certain distance. This can ensure that at least between the two voltage measurement points, the current are homogeneous in $\hat{z}$ and $\hat{\phi}$ (azimuthal) direction. Thus the electric field in the rod varies in one-dimension only and the model is simple. However, this arrangement is inconvenient when taking measurements on large numbers of rods, and it is feasible only when the rod dimension is large enough. A better approach is to use point contacting electrodes to inject current and place the current injecting and voltage measurement electrodes close to each other. But this will require a much more complicated model because one needs to solve for the three-dimensional electric field in the rods. Yamashita gave the DC model on cylindrical rods in reference [16]. But an AC model

has not been developed yet.

CHAPTER 2. EDDY CURRENTS INDUCED IN A FINITE LENGTH LAYERED ROD BY A COAXIAL COIL

2.1 Introduction

As early as 1968, Dodd and Deeds [42] gave an analytical solution for the electromagnetic field of a coil encircling an infinitely long cylindrical conductive rod with a uniform layer whose conductivity and permeability differed from that of the core material. The solution is in the form of integrals of first-order associated Bessel functions giving the magnetic vector potential. From the potential, other electromagnetic quantities of interest are obtained including the eddy current density and the coil impedance. Later Dodd, Cheng, and Deeds [43] generalized the solution for a coil coaxial with a cylindrical conductor having an arbitrary number of concentric, homogeneous layers. The vector potential, also expressed in the form of Bessel integrals, employs an recursive relationship to link solutions in adjacent layers [43].

In this study, a theory for finite length layered rods is developed accounting for end effects using the truncated region eigenfunction expansion (TREE) method [44–47]. The work is partly stimulated by the need to evaluate case depths of a case hardened rods taking into account end effects. This avoids systematic errors that can arise whenever the data is interpreted using the infinite rod theory [42, 43]. There are, in fact, many other possible applications of the finite rod analysis since the results provide, for example, a simple method of calculating the impedance of a lossy inductor with a cylindrical core. By truncating the problem region to a finite length in the axial direction, one can obtain the solutions in the

form of a series. This can be done for a number of similar problems, such as a tube with a bobbin coil inside [44], a finite homogeneous rod encircled by a coil [45], a cylindrical ferrite-cored probe in the presence of a layered conducting half space [46], or a long coil above a conductive plate with a long flaw [47].

As in the above examples, the approach here introduces an artificial boundary to limit the length of the problem domain in the axial direction. A truncation error is involved but its magnitude can be reduced to an acceptable level by making the axial span as large as necessary. Another error is introduced in computation since it is necessary to limit an infinite series solution to a finite number of terms. This error is easy to control and is small if a large number of terms is used, yet the computation cost remains very low compared with that incurred using numerical methods. In fact, the calculation time is also small compared with that for the numerical integration needed for evaluating the traditional infinite rod solutions.

2.2 Magnetic vector potential

Consider the case where the coil encircles a finite, layered conductive rod, shown in Figure 2.1. We assume that the rod has two homogenous layers: an outer layer with outer radius r_2, conductivity σ_2, relative permeability μ_{r2}, and an inner layer with a radius r_1, conductivity σ_1, and relative permeability μ_{r1}. The solution domain is truncated in the axial direction to the region defined by $-h \leq z \leq h$. The electromagnetic field is represented by a magnetic vector potential with only an azimuthal component: $\mathbf{A} = \hat{\phi} A_\phi$. Assuming a time harmonic current varying as the real part of $Ie^{-i\omega t}$, the magnetic vector potential satisfies the Laplace equation in air and the Helmholtz equation,

$$(\nabla^2 + i\omega\mu_0\mu_{rn}\sigma_{n,})\mathbf{A} = 0 \qquad n = 1, 2, \tag{2.1}$$

in the conductive regions 1 and 2. Solutions are of the form,

$$[A\sin(qz) + B\cos(qz)][CI_1(\gamma^{(n)}\rho) + DK_1(\gamma^{(n)}\rho)] \tag{2.2}$$

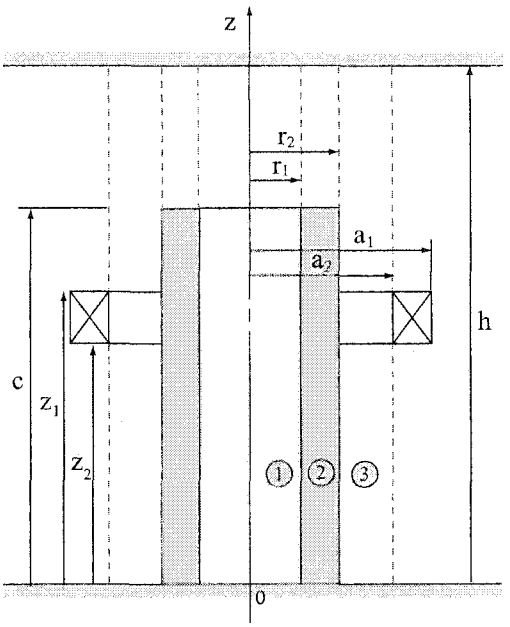

Figure 2.1 Coil coaxial with a two-layer finite rod.

where I_1 and K_1 are associated Bessel functions and

$$\gamma^{(n)} = \sqrt{q^2 - i\omega\mu_0\mu_{rn}\sigma_n} \qquad n = 1, 2. \tag{2.3}$$

A homogeneous Dirichlet condition,

$$A_\phi(\rho, \pm h) = 0, \tag{2.4}$$

is applied at the boundaries, $z = \pm h$. To simplify the problem, an odd solution with respect to z, having the property $A(\rho, z) = -A(\rho, -z)$, is sought first. Then the even symmetry solution is derived following a similar procedure. Hence, only half of the solution region ($0 \leq z \leq h$) is considered at each stage. For the odd parity solution, $A_\phi(\rho, 0) = 0$ and for the even parity, $\frac{\partial A_\phi}{\partial \rho}|_{z=0} = 0$. The solution for a single encircling coil is the average of the odd an even solutions.

2.2.1 Odd parity solution

The magnetic vector potential, A_ϕ, in each subregion, Figure 2.1, can be expanded in terms of a series of appropriate eigenfunctions:

$$A_1(\rho,z) = \frac{2\mu_0 nI}{h}\sum_j \begin{bmatrix} \sin(q_j^{(1)}z) \\ \alpha_j^{(1)}\sin[\gamma_j^{(1)}(h-z)] \end{bmatrix} I_1(\gamma_j^{(1)}\rho)C_j^{(1)} \qquad \begin{matrix} 0\le z<c \\ c\le z\le h \end{matrix} \tag{2.5}$$

$$A_2(\rho,z) = \frac{2\mu_0 nI}{h}\sum_j \begin{bmatrix} \sin(q_j^{(2)}z) \\ \alpha_j^{(2)}\sin[\gamma_j^{(2)}(h-z)] \end{bmatrix} [I_1(\gamma_j^{(2)}\rho)C_j^{(2)}+K_1(\gamma_j^{(2)}\rho)D_j^{(2)}] \qquad \begin{matrix} 0\le z<c \\ c\le z\le h \end{matrix} \tag{2.6}$$

$$A_3(\rho,z) = \frac{2\mu_0 nI}{h}\sum_j \sin(\kappa_j z)\left[I_1(\kappa_j\rho)C_j^{(0)}+K_1(\kappa_j\rho)D_j^{(3)}\right] \qquad 0\le z\le h, \tag{2.7}$$

where, to satisfy (2.4), $\kappa_j = j\pi/h$, $j = 1,2,3...$ and

$$\gamma_j^{(n)} = \sqrt{q_j^{(n)2} - i\omega\mu_0\mu_{rn}\sigma_n} \qquad n = 1,2. \tag{2.8}$$

The eigenvalues $q_j^{(n)}$ and the coefficients $\alpha_j^{(n)}$ are defined below. One set of coefficients, the $C_j^{(0)}$, is prescribed and the solution expresses the other coefficients in terms of this set. The prescribed coefficients are found from the calculation of the vector potential, $A^{(0)}(\rho,z)$, due to a coil in the absence of the rod. The result of this preliminary calculation is that [45]

$$A^{(0)}(\rho,z) = \frac{2\mu_0 nI}{h}\sum_j \sin(\kappa_j z)I_1(\kappa_j\rho)C_j^{(0)}, \tag{2.9}$$

where

$$C_j^{(0)} = -\frac{1}{\kappa_j^3}[\cos(\kappa_j z_1)-\cos(\kappa_j z_2)]\mathcal{K}_1(\kappa_j a_1,\kappa_j a_2), \tag{2.10}$$

with

$$\mathcal{K}_1(r_1,r_2) = \int_{r_2}^{r_1} rK_1(r)\,dr. \tag{2.11}$$

In the steps which follow, the eigenvalues, $q_j^{(n)}$, and the coefficients $\alpha_j^{(n)}$ are found by applying interface conditions, at the end of the rod. Then the remaining unknown coefficients are determined by applying interface conditions at the cylindrical interfaces where

$\rho = r_1$ and $\rho = r_2$. Using the continuity of H_ρ at the end of the rod, it is found that

$$\alpha_j^{(n)} = -\frac{q_j^{(n)} \cos(q_j^{(n)} c)}{\mu_{rn} \gamma_j^{(n)} \cos[\gamma_j^{(n)}(h-c)]} \qquad n = 1, 2, \tag{2.12}$$

and from the continuity of E_ϕ at the end of the rod,

$$\sin(q_j^{(n)} c) = \alpha_j^{(n)} \sin[\gamma_j^{(n)}(h-c)] \qquad n = 1, 2. \tag{2.13}$$

Eliminating $\alpha_j^{(n)}$ gives

$$\mu_{rn} \gamma_j^{(n)} \tan(q_j^{(n)} c) + q_j^{(n)} \tan[\gamma_j^{(n)}(h-c)] = 0. \qquad n = 1, 2 \tag{2.14}$$

from which with (2.8), the eigenvalues, $q_j^{(n)}$, are found by means of a numerical search for roots. Once the roots have been determined, the $\alpha_j^{(n)}$ can be found from (2.12).

Next consider the cylindrical interfaces. From the continuity of E_ϕ and H_z at $\rho = r_1$,

$$A_1 = A_2 \tag{2.15}$$

and

$$\begin{bmatrix} \frac{1}{\mu_{r1}} \\ 1 \end{bmatrix} \frac{1}{\rho} \frac{\partial(\rho A_1)}{\partial \rho}\bigg|_{\rho=r1} = \begin{bmatrix} \frac{1}{\mu_{r2}} \\ 1 \end{bmatrix} \frac{1}{\rho} \frac{\partial(\rho A_2)}{\partial \rho}\bigg|_{\rho=r1} \qquad \begin{matrix} 0 \le z < c \\ c \le z \le h. \end{matrix} \tag{2.16}$$

Similarly, from the continuity of E_ϕ and H_z at $\rho = r_2$,

$$A_2 = A_3 \tag{2.17}$$

and

$$\begin{bmatrix} \frac{1}{\mu_{r2}} \\ 1 \end{bmatrix} \frac{1}{\rho} \frac{\partial(\rho A_2)}{\partial \rho}\bigg|_{\rho=r2} = \begin{bmatrix} 1 \\ 1 \end{bmatrix} \frac{1}{\rho} \frac{\partial(\rho A_3)}{\partial \rho}\bigg|_{\rho=r2} \qquad \begin{matrix} 0 \le z < c \\ c \le z \le h. \end{matrix} \tag{2.18}$$

Substituting (2.5) and (2.6) into (2.15), multiplying by $\sin(\kappa_i z)$ and integrating from zero to h gives

$$\sum_j P_{ij} I_1(\gamma_j^{(1)} r_1) C_j^{(1)} = \sum_j Q_{ij} [I_1(\gamma_j^{(2)} r_1) C_j^{(2)} + K_1(\gamma_j^{(2)} r_1) D_j^{(2)}] \tag{2.19}$$

where

$$P_{ij} = \int_0^c \sin(\kappa_i z) \sin(q_j^{(1)} z)\, dz + \alpha_j^{(1)} \int_c^h \sin(\kappa_i z) \sin[\gamma_j^{(1)}(h-z)]\, dz \tag{2.20}$$

and

$$Q_{ij} = \int_0^c \sin(\kappa_i z)\sin(q_j^{(2)} z)\,dz + \alpha_j^{(2)} \int_c^h \sin(\kappa_i z)\sin[\gamma_j^{(2)}(h-z)]\,dz. \tag{2.21}$$

The integrations in the above equations are evaluated using

$$\int_0^c \sin(\kappa_i z)\sin(q_j^{(n)} z)\,dz = \frac{\sin[(q_j^{(n)} - \kappa_i)c]}{2(q_j^{(n)} - \kappa_i)} - \frac{\sin[(q_j^{(n)} + \kappa_i)c]}{2(q_j^{(1)} + \kappa_i)} \qquad n = 1, 2 \tag{2.22}$$

and

$$\begin{aligned}(\gamma_j^{(n)2} - \kappa_i^2) \int_c^h \sin(\kappa_i z)\sin[\gamma_j^{(n)}(h-z)]\,dz = \\ \kappa_i \cos(c\kappa_i)\sin[(c-h)\gamma_j^{(n)}] - \gamma_j^{(n)}\sin(c\kappa_i)\cos[(c-h)\gamma_j^{(n)}] \qquad n = 1, 2.\end{aligned} \tag{2.23}$$

Similarly, from (2.16), one gets

$$\sum_j R_{ij}\gamma_j^{(1)} I_0(\gamma_j^{(1)} r_1) C_j^{(1)} = \sum_j S_{ij}\left[\gamma_j^{(2)} I_0(\gamma_j^{(2)} r_1) C_j^{(2)} - \gamma_j^{(2)} K_0(\gamma_j^{(2)} r_1) D_j^{(2)}\right] \tag{2.24}$$

where

$$R_{ij} = \frac{1}{\mu_{r1}} \int_0^c \sin(\kappa_i z)\sin(q_j^{(1)} z)\,dz + \alpha_j^{(1)} \int_c^h \sin(\kappa_i z)\sin[\gamma_j^{(1)}(h-z)]\,dz \tag{2.25}$$

and

$$S_{ij} = \frac{1}{\mu_{r2}} \int_0^c \sin(\kappa_i z)\sin(q_j^{(2)} z)\,dz + \alpha_j^{(2)} \int_c^h \sin(\kappa_i z)\sin[\gamma_j^{(2)}(h-z)]\,dz. \tag{2.26}$$

Using the same method with equations (2.6), (2.7), (2.17) and (2.18), one finds that

$$\sum_j \frac{2}{h} Q_{ij}[I_1(\gamma_j^{(2)} r_2) C_j^{(2)} + K_1(\gamma_j^{(2)} r_2) D_j^{(2)}] = I_1(\kappa_j r_2) C_j^{(0)} + K_1(\kappa_j r_2) D_j^{(3)} \tag{2.27}$$

and

$$\sum_j \frac{2}{h} S_{ij}\left[\gamma_j^{(2)} I_0(\gamma_j^{(2)} r_2) C_j^{(2)} - \gamma_j^{(2)} K_0(\gamma_j^{(2)} r_2) D_j^{(2)}\right] = \kappa_j I_0(\kappa_j r_2) C_j^{(0)} - \kappa_j K_0(\kappa_j r_2) D_j^{(3)}. \tag{2.28}$$

Write equations (2.19), (2.24), (2.27) and (2.28) in matrix form as

$$\mathbf{P} I_1(\boldsymbol{\gamma}^{(1)} r_1)\mathbf{C}^{(1)} = \mathbf{Q}[I_1(\boldsymbol{\gamma}^{(2)} r_1)\mathbf{C}^{(2)} + K_1(\boldsymbol{\gamma}^{(2)} r_1)\mathbf{D}^{(2)}] \tag{2.29}$$

$$\mathbf{R}\boldsymbol{\gamma}^{(1)} I_0(\boldsymbol{\gamma}^{(1)} r_1)\mathbf{C}^{(1)} = \mathbf{S}\boldsymbol{\gamma}^{(2)}[I_0(\boldsymbol{\gamma}^{(2)} r_1)\mathbf{C}^{(2)} - K_0(\boldsymbol{\gamma}^{(2)} r_1)\mathbf{D}^{(2)}] \tag{2.30}$$

$$\frac{2}{h}\mathbf{Q}[I_1(\boldsymbol{\gamma}^{(2)}r_2)\mathbf{C}^{(2)} + K_1(\boldsymbol{\gamma}^{(2)}r_2)\mathbf{D}^{(2)}] = I_1(\boldsymbol{\kappa}r_2)\mathbf{C}^{(0)} + K_1(\boldsymbol{\kappa}r_2)\mathbf{D}^{(3)} \tag{2.31}$$

$$\frac{2}{h}\mathbf{S}\boldsymbol{\gamma}^{(2)}[I_0(\boldsymbol{\gamma}^{(2)}r_2)\mathbf{C}^{(2)} - K_0(\boldsymbol{\gamma}^{(2)}r_2)\mathbf{D}^{(2)}] = \boldsymbol{\kappa}[I_0(\boldsymbol{\kappa}r_2)\mathbf{C}^{(0)} - K_0(\boldsymbol{\kappa}r_2)\mathbf{D}^{(3)}]. \tag{2.32}$$

Here Bessel functions with bold symbol arguments represent diagonal matrices. $\mathbf{C}^{(0)}$, $\mathbf{C}^{(1)}$, $\mathbf{C}^{(2)}$, $\mathbf{D}^{(1)}$, $\mathbf{D}^{(2)}$ are column vectors. The four unknowns $\mathbf{C}^{(1)}$, $\mathbf{C}^{(2)}$, $\mathbf{D}^{(2)}$, $\mathbf{D}^{(3)}$ can be expressed in terms of the known vector $\mathbf{C}^{(0)}$ using equations (2.29-2.32) by matrix and vector manipulations. The final expressions are as follows:

$$\mathbf{C}^{(1)} = \frac{h}{2}\frac{1}{r_1 r_2}\mathbf{T}^{-1}\mathbf{C}^{(0)} \tag{2.33}$$

$$\mathbf{C}^{(2)} = \frac{h}{2}\frac{1}{r_2}\mathbf{M}_1\mathbf{T}^{-1}\mathbf{C}^{(0)} \tag{2.34}$$

$$\mathbf{D}^{(2)} = \frac{h}{2}\frac{1}{r_2}\mathbf{N}_1\mathbf{T}^{-1}\mathbf{C}^{(0)} \tag{2.35}$$

$$\mathbf{D}^{(3)} = \mathbf{W}\mathbf{C}^{(0)} \tag{2.36}$$

where $\boldsymbol{M_1}$, $\boldsymbol{N_1}$, $\boldsymbol{T}$, $\boldsymbol{W}$ are defined as

$$\mathbf{M}_1 = \boldsymbol{\gamma}^{(2)}K_0(\boldsymbol{\gamma}^{(2)}r_1)\mathbf{Q}^{-1}\mathbf{P}I_1(\boldsymbol{\gamma}^{(1)}r_1) + K_1(\boldsymbol{\gamma}^{(2)}r_1)\mathbf{S}^{-1}\mathbf{R}\boldsymbol{\gamma}^{(1)}I_0(\boldsymbol{\gamma}^{(1)}r_1) \tag{2.37}$$

$$\mathbf{N}_1 = \boldsymbol{\gamma}^{(2)}I_0(\boldsymbol{\gamma}^{(2)}r_1)\mathbf{Q}^{-1}\mathbf{P}I_1(\boldsymbol{\gamma}^{(1)}r_1) - I_1(\boldsymbol{\gamma}^{(2)}r_1)\mathbf{S}^{-1}\mathbf{R}\boldsymbol{\gamma}^{(1)}I_0(\boldsymbol{\gamma}^{(1)}r_1) \tag{2.38}$$

$$\mathbf{M}_2 = I_1(\boldsymbol{\gamma}^{(2)}r_2)\mathbf{M}_1 + K_1(\boldsymbol{\gamma}^{(2)}r_2)\mathbf{N}_1 \tag{2.39}$$

$$\mathbf{N}_2 = I_0(\boldsymbol{\gamma}^{(2)}r_2)\mathbf{M}_1 - K_0(\boldsymbol{\gamma}^{(2)}r_2)\mathbf{N}_1 \tag{2.40}$$

$$\mathbf{T} = \boldsymbol{\kappa}K_0(\boldsymbol{\kappa}r_2)\mathbf{Q}\mathbf{M}_2 + K_1(\boldsymbol{\kappa}r_2)\mathbf{S}\boldsymbol{\gamma}^{(2)}\mathbf{N}_2 \tag{2.41}$$

and

$$\mathbf{W} = \mathbf{K}_1^{-1}(\boldsymbol{\kappa}r_2)\left[\frac{1}{r_2}\mathbf{Q}\mathbf{M}_2\mathbf{T}^{-1} - I_1(\boldsymbol{\kappa}r_2)\right]. \tag{2.42}$$

The odd parity solution represents the field due to a rod length $2c$ encircled by two identical coaxial coils carrying current in antiphase and located symmetrically on opposite sides of the $z = 0$ plane. If the rod is long and the coils are well separated then the electric field due to one such coil may be negligible in the $z = 0$ plane, in which case the odd parity solution gives a good approximation to the field of a single coil in the half-space that it occupies.

2.2.2 Even parity solution

In order to represent end effects due to a short rod and a co-axial coil, one needs to average the odd and even solutions. The even parity solution represents the field due to two identical coaxial coils carrying alternating current in phase, symmetrically placed about the $z = 0$ plane. Incidentally, if the rod is long and the coils well separated, the even and odd solutions should be similar in one half of the problem domain.

The even parity solution can be derived following a procedure similar to that described in the previous sections. Rather than going through the derivation in full, the main distinctive features of the even parity solution are summarized below. Note that the main results of the previous section, equations (2.29) to (2.42) can be preserved in this form to represent either odd, even or a linear combination of both odd and even solutions. One only needs to introduce a new set of eigenvalues for $\boldsymbol{\kappa}, \mathbf{q}$ and $\boldsymbol{\gamma}$ and modify the definition of the matrices $\mathbf{P}$, $\mathbf{Q}$, $\mathbf{R}$ and $\mathbf{S}$. These modifications will now be outlined.

For the even parity solution, one needs to replace the sine function in equation (2.7) for the potential in the region $0 \leq z \leq h$ by a cosine function. Similarly, for the region $0 \leq z \leq c$, the sine function in equations (2.5) and (2.6) is replaced by a cosine function. However, one needs to keep the sine for the solution in the region $c \leq z \leq h$, equations (2.5) and (2.6), because the homogeneous boundary conditions are to be satisfied at $z = h$. Thus the magnetic vector potentials in each region for an even parity solution are given by

$$A_1(\rho, z) = \frac{2\mu_0 nI}{h} \sum_j \begin{bmatrix} \cos(q_j^{(1)} z) \\ \alpha_j^{(1)} \sin[\gamma_j^{(1)}(h - z)] \end{bmatrix} I_1(\gamma_j^{(1)}\rho) C_j^{(1)} \qquad \begin{matrix} 0 \leq z < c \\ c \leq z \leq h \end{matrix} \tag{2.43}$$

$$A_2(\rho, z) = \frac{2\mu_0 nI}{h} \sum_j \begin{bmatrix} \cos(q_j^{(2)} z) \\ \alpha_j^{(2)} \sin[\gamma_j^{(2)}(h - z)] \end{bmatrix} [I_1(\gamma_j^{(2)}\rho) C_j^{(2)} + K_1(\gamma_j^{(2)}\rho) D_j^{(2)}] \qquad \begin{matrix} 0 \leq z < c \\ c \leq z \leq h \end{matrix} \tag{2.44}$$

$$A_3(\rho, z) = \frac{2\mu_0 nI}{h} \sum_j \cos(\kappa_j z) \left[I_1(\kappa_j \rho) C_j^{(0)} + K_1(\kappa_j \rho) D_j^{(3)} \right] \qquad 0 \leq z \leq h, \tag{2.45}$$

where the coefficient $C_j^{(0)}$ for an even solution is expressed as [45]:

$$C_j^{(0)} = \frac{1}{\kappa_j^3}[\sin(\kappa_j z_1) - \sin(\kappa_j z_2)]\mathcal{K}_1(\kappa_j a_1, \kappa_j a_2), \tag{2.46}$$

and setting $\kappa_j = (2j-1)\pi/2h$, $j = 1, 2, 3...$ ensures that $A_3(\rho, \pm h)$ vanishes.

From the continuity conditions that apply to the field at the end of the rod, the new eigenvalues for even symmetry are the solutions of

$$q_j^{(n)} \tan[\gamma_j^{(n)}(h-c)] - \mu_{rn}\gamma_j^{(n)} \cot[q_j^{(n)}c] = 0, \;\; n = 1, 2. \tag{2.47}$$

Finally, it is found that the matrices **P**,**Q**, **R** and **S** are defined in terms of the new eigenvalues for the even solution with their matrix elements, given by

$$P_{ij} = \int_0^c \cos(\kappa_i z)\cos(q_j^{(1)}z)\,dz + \alpha_j^{(1)}\int_c^h \cos(\kappa_i z)\sin[\gamma_j^{(1)}(h-z)]\,dz \tag{2.48}$$

$$Q_{ij} = \int_0^c \cos(\kappa_i z)\cos(q_j^{(2)}z)\,dz + \alpha_j^{(2)}\int_c^h \cos(\kappa_i z)\sin[\gamma_j^{(2)}(h-z)]\,dz \tag{2.49}$$

$$R_{ij} = \frac{1}{\mu_{r1}}\int_0^c \cos(\kappa_i z)\cos(q_j^{(1)}z)\,dz + \alpha_j^{(1)}\int_c^h \cos(\kappa_i z)\sin[\gamma_j^{(1)}(h-z)]\,dz \tag{2.50}$$

$$S_{ij} = \frac{1}{\mu_{r2}}\int_0^c \cos(\kappa_i z)\cos(q_j^{(2)}z)\,dz + \alpha_j^{(2)}\int_c^h \cos(\kappa_i z)\sin[\gamma_j^{(2)}(h-z)]\,dz \tag{2.51}$$

where

$$\alpha_j^{(n)} = \frac{q_j^{(n)}\sin(q_j^{(n)}c)}{\mu_{rn}\gamma_j^{(n)}\cos[\gamma_j^{(n)}(h-c)]} \qquad n = 1, 2. \tag{2.52}$$

The integrals in (2.48) to (2.51) are evaluated as follows:

$$(q_j^{(n)2} - \kappa_i^2)\int_0^c \cos(\kappa_i z)\cos(q_j^{(n)}z)\,dz =$$
$$q_j^{(n)}\cos(c\kappa_i)\sin(cq_j^{(n)}) - \kappa_i\cos(cq_j^{(n)})\sin(c\kappa_i) \qquad n = 1, 2 \tag{2.53}$$

$$(\gamma_j^{(n)2} - \kappa_i^2)\int_c^h \cos(\kappa_i z)\sin[\gamma_j^{(n)}(h-z)]\,dz =$$
$$-\gamma_j^{(n)}\cos[(c-h)\gamma_j^{(n)}]\cos(c\kappa_i) + \gamma_j^{(n)}\cos(h\kappa_i) - \kappa_i\sin[(c-h)\gamma_j^{(n)}]\sin(c\kappa_i) \qquad n = 1, 2$$
$$. \tag{2.54}$$

2.3 Impedance

The impedance change of a source coil due to the presence of the conductive object is given in terms of an integral over the coil region by

$$I^2\Delta Z = -\int \Delta\mathbf{E}\cdot\mathbf{J}\,d\mathbf{r}, \tag{2.55}$$

where $\Delta\mathbf{E}$ is the electric field due to eddy current in the conductor and $\mathbf{J}$ is the coil current density. The impedance is expressed in a more convenient form for present purposes using what is commonly known as a reciprocal relationship based on the identity

$$\int_\Omega (\mathbf{b}\cdot\nabla\times\nabla\times\mathbf{a} - \mathbf{a}\cdot\nabla\times\nabla\times\mathbf{b})\,d\mathbf{r} = \int_S (\mathbf{a}\times\nabla\times\mathbf{b} - \mathbf{b}\times\nabla\times\mathbf{a})\cdot d\mathbf{S} \tag{2.56}$$

where an arbitrary regular surface S encloses a region Ω and $d\mathbf{S} = \mathbf{n}dS$, $\mathbf{n}$ being the outward unit normal vector. With the identifications $\mathbf{a}\equiv\mathbf{E}^{(0)}$ and $\mathbf{b}\equiv\Delta\mathbf{E}$, where the superscript (0) indicates the field in the absence of the conductor, transformation of (2.55) gives

$$I^2\Delta Z = \int_S (\Delta\mathbf{E}\times\mathbf{H}^{(0)} - \mathbf{E}^{(0)}\times\Delta\mathbf{H})\cdot d\mathbf{S}, \tag{2.57}$$

where $\Delta\mathbf{H}$ is the change in the magnetic field due to the presence of the conductor. It is emphasized that the surface S encloses the primary source, the coil in this case, and the direction of $d\mathbf{S}$ is that of an outward normal with respect to the source.

In applying the foregoing general expression, (2.57), to the case of the compound rod, the closed surface S will be taken to be the surface of radius r_2 co-joined with surfaces at the planes $z=\pm h$ where the field vanishes, extending outwards to join a cylindrical surface at infinity on which the surface integral vanishes. With other contributions vanishing, we need consider only an integral over the cylinder, radius r_2 of length $2h$. With these factors taken into account, substituting the vector potential into the equation (2.57) gives

$$I^2\Delta Z = \frac{2\pi i\omega}{\mu_0}\int_0^h \left[A^{(0)}\frac{\partial(\rho\Delta A)}{\partial\rho} - \Delta A\frac{\partial(\rho A^{(0)})}{\partial\rho}\right]_{\rho=r_2} dz. \tag{2.58}$$

Note that without the rod present, the magnetic vector in region 3 is given by

$$A^{(0)}(\rho,z) = \frac{2\mu_0 nI}{h}\sum_j \sin(\kappa_j z) I_1(\kappa_j\rho) C_j^{(0)}. \tag{2.59}$$

With the rod present, the magnetic vector potential in this region is given by (2.7). Substituting into (2.58), one finds that

$$\Delta Z = -i\omega\mu_0 \frac{4\pi n^2}{h} \mathbf{C^{(0)}} \mathbf{W} \mathbf{C^{(0)}} \tag{2.60}$$

where $\mathbf{W}$ is given in (2.42). Equation (2.60) is also applicable for the even case, with $\mathbf{C^{(0)}}$ given by (2.46).

2.4 Tube

With a few modifications, the model can be applied to the problem of a tube encircled by a coaxial coil. Only the odd parity solution for a tube is given here. The even parity solution can be derived easily using a similar procedure. Since the inner layer for a tube is air, equation (2.5) is replaced with

$$A_1(\rho, z) = 2\frac{\mu_0 nI}{h} \sum_j \sin(\kappa_j z) I_1(\kappa_j \rho) C_j^{(1)} \qquad 0 \le z \le h \tag{2.61}$$

where $\kappa_j = j\pi/h$, $j = 1, 2, 3....$ Note that for a tube, equations (2.8), (2.13) and (2.14) are used for $n = 2$ only. From the continuity of E_ϕ and H_z at $\rho = r_1$, and with the new expression for $A_1(\rho, z)$, one finds that the definition for P_{ij} and R_{ij} should be changed to $P_{ij} = (h/2)\delta_{ij}$ and $R_{ij} = (h/2)\delta_{ij}$. Accordingly, in (2.29), (2.30), (2.37) and (2.38), one should replace $\mathbf{P}, \mathbf{R}$ by $(h/2)\mathbf{I}$, where $\mathbf{I}$ is a unit matrix and replace $\boldsymbol{\gamma}^{(1)}$ by $\boldsymbol{\kappa}$. The new expressions for these equations are listed below:

$$\frac{h}{2} I_1(\boldsymbol{\kappa} r_1) \mathbf{C^{(1)}} = \mathbf{Q}[I_1(\boldsymbol{\gamma^{(2)}} r_1) \mathbf{C^{(2)}} + K_1(\boldsymbol{\gamma^{(2)}} r_1) \mathbf{D^{(2)}}] \tag{2.62}$$

$$\frac{h}{2} \boldsymbol{\kappa} I_0(\boldsymbol{\kappa} r_1) \mathbf{C^{(1)}} = \mathbf{S}\boldsymbol{\gamma^{(2)}}[I_0(\boldsymbol{\gamma^{(2)}} r_1) \mathbf{C^{(2)}} - K_0(\boldsymbol{\gamma^{(2)}} r_1) \mathbf{D^{(2)}}] \tag{2.63}$$

$$\mathbf{M_1} = \frac{h}{2} \boldsymbol{\gamma^{(2)}} K_0(\boldsymbol{\gamma^{(2)}} r_1) \mathbf{Q^{-1}} I_1(\boldsymbol{\kappa} r_1) + \frac{h}{2} K_1(\boldsymbol{\gamma^{(2)}} r_1) \mathbf{S^{-1}} \boldsymbol{\kappa} I_0(\boldsymbol{\kappa} r_1) \tag{2.64}$$

and

$$\mathbf{N_1} = \frac{h}{2} \boldsymbol{\gamma^{(2)}} I_0(\boldsymbol{\gamma^{(2)}} r_1) \mathbf{Q^{-1}} I_1(\boldsymbol{\kappa} r_1) - \frac{h}{2} I_1(\boldsymbol{\gamma^{(2)}} r_1) \mathbf{S^{-1}} \boldsymbol{\kappa} I_0(\boldsymbol{\kappa} r_1). \tag{2.65}$$

Note that for a tube, equations (2.31-2.36), (2.39-2.42) and (2.60) remain applicable.

2.5 Eigenvalue calculations

One of the critical steps is to calculate precisely the complex eigenvalues $q_i^{(n)}$ and $\gamma_i^{(n)}$, which are the roots of equation (2.14) or (2.47). Different approaches can be used. One method is to use the"FindRoot" function in Mathematica, using two different initial values. The first set is computed by selecting an initial value for the case $c = 0$ when $\gamma^{(n)} = \kappa$ and the second set is computed by selecting an initial value for the case $c = h$ when $\gamma^{(n)} = \sqrt{\kappa^2 + j\omega\mu\sigma}$. The two sets of computed eigenvalues are then combined to give the final set. This method works well for the odd solution for nonmagnetic material ($\mu_r = 1$).

For other cases, a similar approach to that described in reference [47] is used. This approach uses Newton-Raphson method and changes c step by step. First, start with $c = 0$, in which case $\gamma = \kappa$. Then increase the rod length by a small step Δc and use the Newton-Raphson method with κ as the initial values to calculate $\gamma_i^{(n)}$ for $c = \Delta c$. Keep increasing c step by step. In each step, use $\gamma_i^{(n)}$ calculated in the previous step as the initial value, until c increases to the desired value. Another set of eigenvalues are calculated starting from $c = h$, and then decreasing c step by step. In each step, the Newton-Raphson technique is used with $\gamma_i^{(n)}$ calculated in the previous step as the initial value, until c decreases to the desired value. Combine the two sets of computed eigenvalues to give the complete set. With this approach, accurate eigenvalues can be obtained for magnetic material.

2.6 Results

The change of the coil impedance as it is traversed coaxially across the end of a rod or a tube is calculated using both the TREE method and a 2D FEM package. Results are shown in Figure 2.2 and Figure 2.3. In these figures, the abscissa axis shows the relative distance between the coil center and the rod or tube end. Negative values mean that the rod or tube is inside the coil. The results are normalized to the isolated coil reactance X_0. The cases considered are a two-layer steel rod or an aluminum tube excited at 1kHz. Some of the coil and rod parameters are the same for both cases. They are shown in Table 2.1.

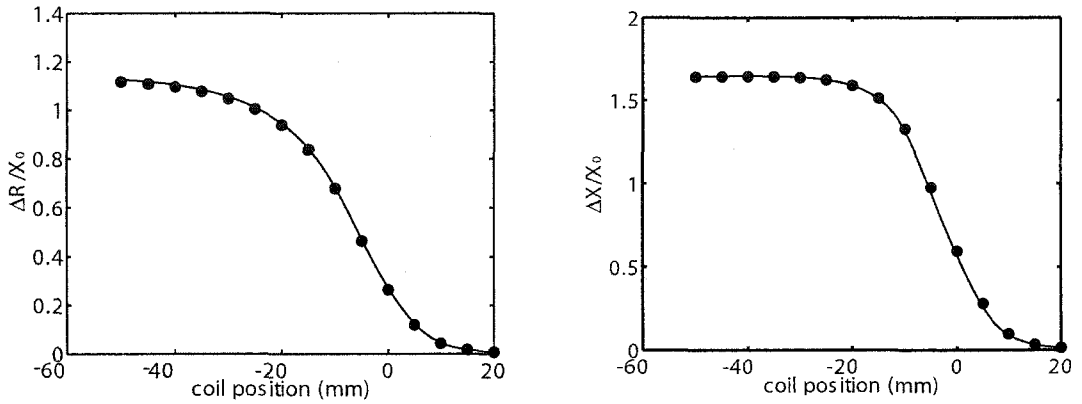

Figure 2.2 Normalized coil resistance (left) and reactance (right) variation with position due to the the two-layer steel rod at 1kHz: comparison between TREE method (solid line) and FEMLAB result (solid circles).

Other parameters are shown in Table 2.2. The border of the region is far away from the limit of the coil movement. The number of summation terms for both cases are 80. For the aluminum tube whose length is very short, both odd and even solutions are used to calculate the results. But for the steel rod which is long compared with the coil, only the odd solution is used. As shown in Figure 2.2, the odd solution is sufficient to give a very good result.

Normalized impedance variations with frequency are also calculated for a homogeneous rod and two layered steel rods with different layer depths, as shown in Figure 2.4. The frequency varies from 6.3 Hz to 1995.3 Hz. Dimensions for the coil, the length and outer radius for the rods are the same as above. The inner radius for the rods are 8.69 mm, 10.69 mm, 12.69 mm. Thus the outer layer depths are 4 mm, 2 mm and 0 mm respectively. The

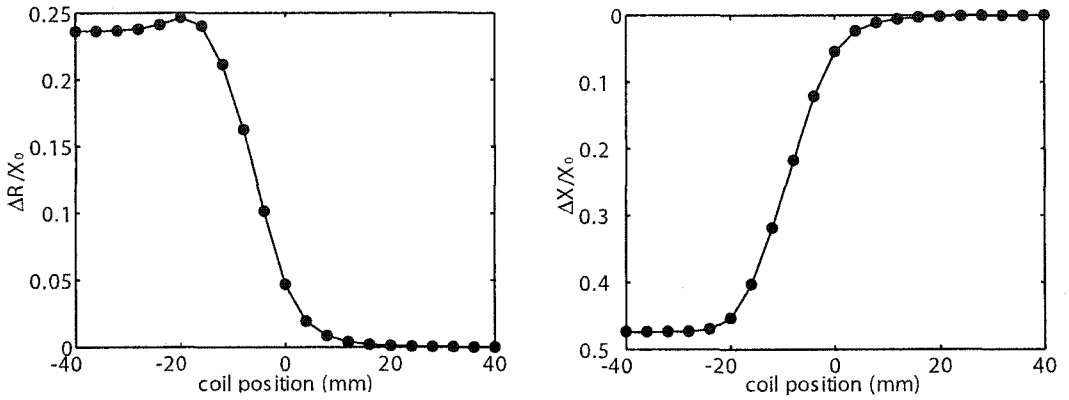

Figure 2.3 Normalized coil resistance (top) and reactance (bottom) variation with position due to the short aluminum tube at 1kHz: comparison between TREE method (solid line) and FEMLAB result (solid circles).

Table 2.1 Coil and rod parameters that are the same for Figure 2.2 (Aluminum tube) and Figure 2.3 (two-layer steel rod).

a_1	13.7 mm
a_2	16.25 mm
$z_2 - z_1$	20 mm
r_1	11.02 mm
r_2	12.69 mm
h	412 mm
number of turns for the coil	3200

coil center is at the top end of the rod. Again, only the odd solution is used here.

Figure 2.4 can be used to discriminate the outer layer depth by fitting frequency scan experimental data with the theoretical predictions. For coils encircling a long layered rod, the model in [43] has been applied in Appendix A and reference [33]to evaluate case depth of case hardened steel rods. However, in order to take measurements on short steel rods, end effects should be considered. In this case, the finite rod model developed in this chapter can be used. Figure 2.4 shows that the sensitivity of the outer layer depth is higher in the lower frequency range. Thus one should take measurements in the lower frequency range whenever possible. The convergence region in Figure 2.4 (584 Hz to 858 Hz) is expanded and

Table 2.2 Coil and rod parameters that are different for Figure 2.2 (Aluminum tube) and Figure 2.3 (two-layer steel rod).

	aluminum tube	two-layer steel rod
c	30 mm	206 mm
μ_{r1}	1	66.15
σ_1	0	5.05 MS/m
μ_{r2}	1	37.58
$\sigma 2$	35.4 MS/m	3.28 MS/m

shown in Figure 2.5. If the frequency is too low, the measurement data will be subject to high noise level. An appropriate range should be chosen in order to obtain high sensitivity and keep a reasonable signal-to-noise level. It should be pointed out that the convergence region is dependent on material properties. The difference will be smaller if the difference of the conductivity and permeability between the two layers is smaller.

2.7 Discussion of the system equations

Equations (2.29)-(2.32) can be solved to give different expressions to those given in (2.33) - (2.42). These new expressions are below. Move $\mathbf{P}$ to the right side of equation (2.29) and multiply both sides by $I_0(\boldsymbol{\gamma}^{(1)}r_1)$ to give

$$I_0(\boldsymbol{\gamma}^{(1)}r_1)I_1(\boldsymbol{\gamma}^{(1)}r_1)\mathbf{C}^{(1)} = I_0(\boldsymbol{\gamma}^{(1)}r_1)\mathbf{P}^{-1}\mathbf{Q}[I_1(\boldsymbol{\gamma}^{(2)}r_1)\mathbf{C}^{(2)} + K_1(\boldsymbol{\gamma}^{(2)}r_1)\mathbf{D}^{(2)}]. \quad (2.66)$$

Move $\mathbf{R}\boldsymbol{\gamma}^{(1)}$ to the right side of equation (2.30) and multiply both sides by $I_1(\boldsymbol{\gamma}^{(1)}r_1)$ to give

$$I_1(\boldsymbol{\gamma}^{(1)}r_1)I_0(\boldsymbol{\gamma}^{(1)}r_1)\mathbf{C}^{(1)} = I_1(\boldsymbol{\gamma}^{(1)}r_1)\boldsymbol{\gamma}^{(1)-1}\mathbf{R}^{-1}\mathbf{S}\mathbf{Q}\boldsymbol{\gamma}^{(2)}[I_0(\boldsymbol{\gamma}^{(2)}r_1)\mathbf{C}^{(2)} - K_1(\boldsymbol{\gamma}^{(2)}r_1)\mathbf{D}^{(2)}]. \quad (2.67)$$

Equating the right sides of (2.7) and (2.67), $\mathbf{C}^{(2)}$ can be expressed in terms of $\mathbf{D}^{(2)}$,

$$\mathbf{C}^{(2)} = \mathbf{M}\mathbf{D}^{(2)} = \mathbf{M}_1^{-1}\mathbf{M}_2\mathbf{D}^{(2)} \quad (2.68)$$

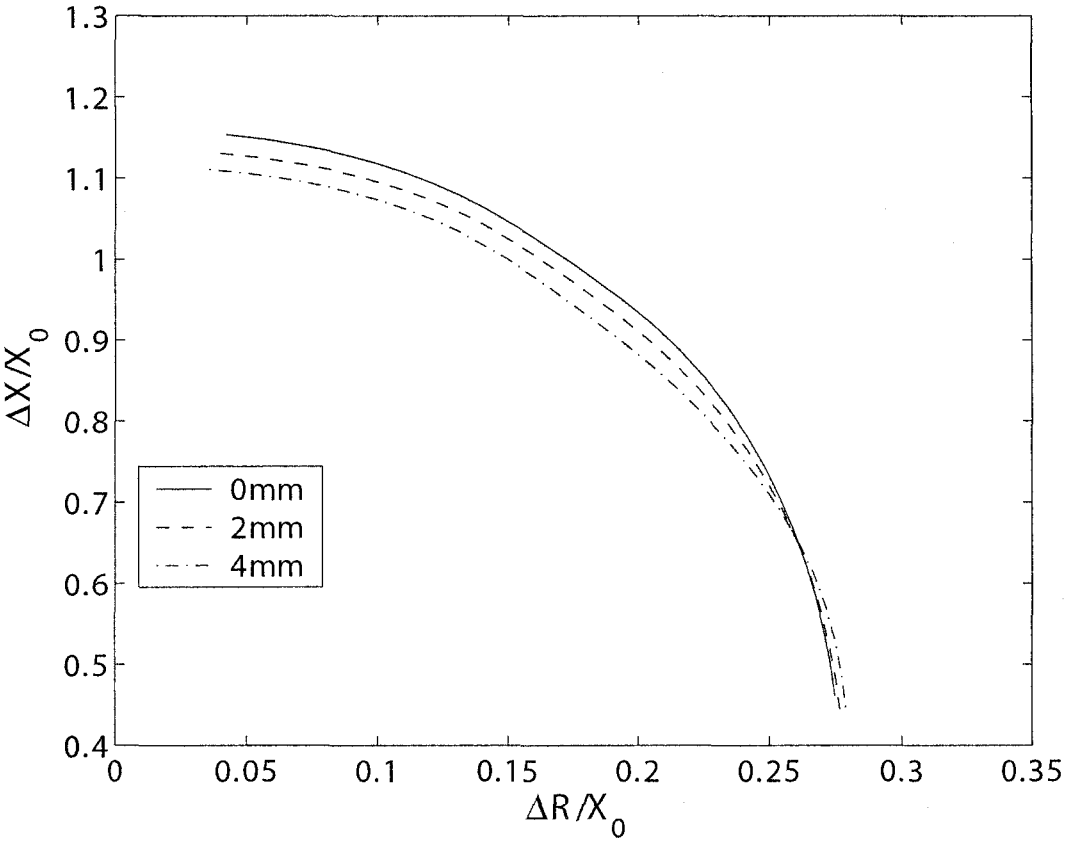

Figure 2.4 Normalized coil impedance variation with frequency (6.3 Hz — 1995.3 Hz) due to the two-layer steel rods with different outer layer depths of 0 mm, 2 mm, and 4 mm respectively. The coil center is placed at the end of the rod.

where

$$\mathbf{M_1} = I_0(\boldsymbol{\gamma}^{(1)} r_1)\mathbf{P}^{-1}\mathbf{Q} I_1(\boldsymbol{\gamma}^{(2)} r_1) - I_1(\boldsymbol{\gamma}^{(1)} r_1)\boldsymbol{\gamma}^{(1)-1}\mathbf{R}^{-1}\mathbf{S}\boldsymbol{\gamma}^{(2)} I_0(\boldsymbol{\gamma}^{(2)} r_1) \tag{2.69}$$

$$\mathbf{M_2} = -I_0(\boldsymbol{\gamma}^{(1)} r_1)\mathbf{P}^{-1}\mathbf{Q} K_1(\boldsymbol{\gamma}^{(2)} r_1) - I_1(\boldsymbol{\gamma}^{(1)} r_1)\boldsymbol{\gamma}^{(1)-1}\mathbf{R}^{-1}\mathbf{S}\boldsymbol{\gamma}^{(2)} K_0(\boldsymbol{\gamma}^{(2)} r_1). \tag{2.70}$$

Substitute (2.68) - (2.70) into (2.31) and (2.32) to give

$$\mathbf{W_1 D^{(2)}} = \boldsymbol{\kappa}[I_1(\boldsymbol{\kappa} r_2)\mathbf{C^{(0)}} + K_1(\boldsymbol{\kappa} r_2)\mathbf{D^{(3)}}] \tag{2.71}$$

$$\mathbf{W_2 D^{(2)}} = \boldsymbol{\kappa}[I_0(\boldsymbol{\kappa} r_2)\mathbf{C^{(0)}} - K_0(\boldsymbol{\kappa} r_2)\mathbf{D^{(3)}}] \tag{2.72}$$

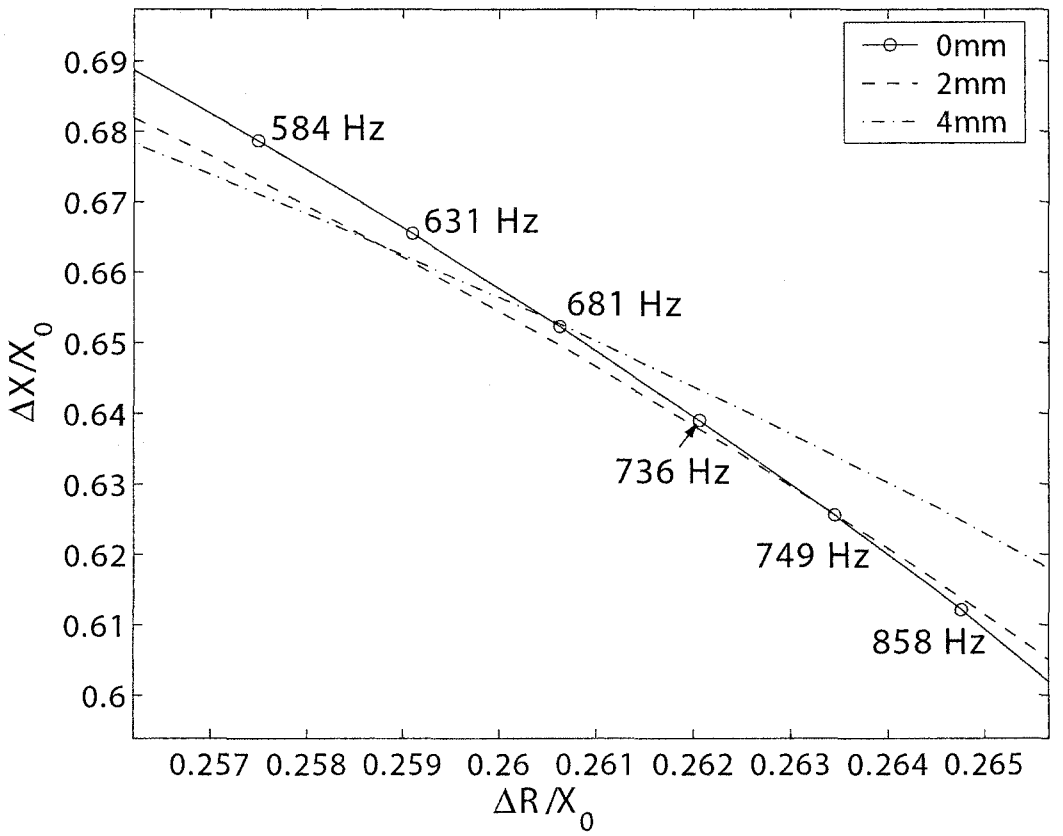

Figure 2.5 Normalized coil impedance variation with frequency (584 Hz to 858 Hz) due to the two-layer steel rods with different outer layer depths of 0 mm, 2 mm, and 4 mm respectively. The coil center is placed at the end of the rod.

where

$$\mathbf{W_1} = \frac{2}{h}\mathbf{Q}[I_1(\boldsymbol{\gamma}^{(2)}r_2)\mathbf{M} + K_1(\boldsymbol{\gamma}^{(2)}r_2)] \tag{2.73}$$

$$\mathbf{W_2} = \frac{2}{h}\mathbf{S}\boldsymbol{\gamma}^{(2)}[I_0(\boldsymbol{\gamma}^{(2)}r_2)\mathbf{M} + K_0(\boldsymbol{\gamma}^{(2)}r_2)]. \tag{2.74}$$

Multiply both sides of (2.71) by $K_0(\boldsymbol{\kappa}r_2)$ and multiply both sides of (2.72) by $K_1(\boldsymbol{\kappa}r_2)$ and add them, one gets

$$[K_0(\boldsymbol{\kappa}r_2)\mathbf{W_1} + K_1(\boldsymbol{\kappa}r_2)\mathbf{W_2}]\mathbf{D}^{(2)} = \frac{1}{r_2}\mathbf{C}^{(0)}. \tag{2.75}$$

Multiply both sides of (2.71) by $I_0(\kappa r_2)$ and multiply both sides of (2.72) by $I_1(\kappa r_2)$ and subtract them, one gets

$$[I_0(\kappa r_2)\mathbf{W_1} - I_1(\kappa r_2)W_2]\mathbf{D^{(2)}} = \frac{1}{r_2}\mathbf{D^{(3)}}, \tag{2.76}$$

where the Wronskian relationship

$$I_0(\kappa r_2)K_1(\kappa r_2) + I_1(\kappa r_2)K_0(\kappa r_2) = \frac{1}{r_2}\kappa^{-1} \tag{2.77}$$

is used to simplify (2.75) and (2.76). From (2.75), we have

$$\mathbf{D^{(2)}} = \frac{1}{r_2}[K_0(\kappa r_2)\mathbf{W_1} + K_1(\kappa r_2)\mathbf{W_2}]^{-1}\mathbf{C^{(0)}}. \tag{2.78}$$

Substitute it into (2.76) to give

$$\mathbf{D^{(3)}} = \mathbf{W}\mathbf{C^{(0)}} \tag{2.79}$$

where

$$\mathbf{W} = [I_0(\kappa r_2)\mathbf{W_1} - I_1(\kappa r_2)\mathbf{W_2}][K_0(\kappa r_2)\mathbf{W_1} + K_1(\kappa r_2)\mathbf{W_2}]^{-1}. \tag{2.80}$$

Here $\mathbf{W}$ is a nice symmetric expression. But it turns out this expression will cause seriously ill-conditioned matrices, thus it is not numerically efficient. Therefore, expression in (2.42) is used for $\mathbf{W}$ in coding.

2.8 Conclusion

With a finite domain, the magnetic vector potential for a two-layer cylindrical rod excited by an encircling coil can be solved using orthogonal eigenfunctions and expressed as a summation instead of as an integral. Homogeneous boundary conditions are enforced at the boundary of the solution region. Interface conditions at the end of the rod are satisfied by comparing eigenfunctions in the series term by term. To simplify the problem, odd and even parity solution are calculated separately. Closed-form expressions are derived using the TREE method for a two-layer rod with different material properties in each layer. The model has been modified to give the solution for a tube. The coil impedance expression

is useful to allow parametric studies. The agreement with numerical results of the FEM is very good. For calculating result in only one position, the speed of TREE method is comparable with FEM method. But the TREE method can be much faster if one needs to perform a coil position scan, because the matrix $\mathbf{W}$ only needs to be calculated once. The model can be easily extended to a tube whose radius varies along its length, with an encircling coil. The model can be applied for a parametric study for layered cylindrical rods, such as case hardened steel rods as discussed in the previous chapter.

2.9 Future Work

The key part of TREE method is to calculate eigenvalues completely and accurately. This requires a good method to find the roots of a complex equation. The methods shown in section 2.5 works fine for non-magnetic material in any cases. Solutions for long magnetic rods with $h = 2c$ can also be found as shown before. But for short magnetic rods ($c << h$) with high permeability, one needs to find a better way to calculate the eigenvalues. For the two-layer steel rod shown in section 2.6, if we keep its conductivity and permeability the same but change the rod length c to 30 mm, one can work out the eigenvalues for the outer layer using the method in section 2.5, however, this method does not work for the inner layer, which has a higher permeability than the inner layer. In order to applied the TREE method for all cases, a better technique is needed to solve complex eigenvalues.

The TREE method is similar to the mode matching method (MMM), which is widely used in solving wave guides problems [48–53]. Both of these methods involves a truncating region and imposing homogeneous conditions on the artificial boundaries. Since the mode matching method has been investigated for quite a long time and there are many references covering various aspects, they can be borrowed to improve the TREE method.

CHAPTER 3. HALL SENSOR ARRAY AND CRACK DETECTION: EXPERIMENT AND SYSTEM

3.1 Introduction

Conventional eddy current inspection uses induction coils to detect cracks and other flaws but it has been suggested recently that inductive probes are reaching their development limits and that new sensors are needed to push back the present boundaries of flaw detection [54]. For subsurface flaws such as cracks under fasteners in aircraft skins, the performance of inductive sensors is limited by the need to use low frequencies to achieve sufficient penetration of the eddy currents. Induction coil signals, being dependent on the rate of change of flux linkage, are less effective at low frequencies whereas typical solid state sensors do not suffer from a diminished sensitivity in the low frequency regime. In a driver/pick-up probe configuration, a relatively large coil can be used as a driver and high spatial resolution plus good low frequency performance achieved by using small solid state devices as detectors. Because the solid state sensors are easily fabricated as arrays, we can take advantage of this to produce probes that facilitate faster inspections.

Coil arrays have been successfully produced and tested by General Electric company [55], however, additional turns of wire are needed for subsurface flaw detection to improve the low frequency performance. This increases their size and reduces the spatial resolution of the probe. Arrays made with individual Hall sensor ICs (integrated circuits) and a rectangular coil have been produced by Smith and Harrison [56]. However, the integrated circuit package is much bigger than the actual Hall element, therefore the spatial separation of the devices

is limited by the package. To overcome these difficulties, a new probe technology has been developed that uses Hall sensor arrays fabricated on a single wafer. With advanced photolithographic techniques, such arrays can be made with extremely high density.

3.2 Hall effect and Hall sensors

If an electric current flows through a conductor (or a semiconductor) in a magnetic field, the magnetic field exerts a transverse force on the moving charge carriers, which tends to push them to one side of the conductor. A buildup of charge at the sides of the conductors will balance this magnetic influence, producing a measurable voltage between the two sides of the conductor. The presence of the measurable transverse voltage is called the Hall effect named after E. H. Hall who discovered it in 1879 [60].

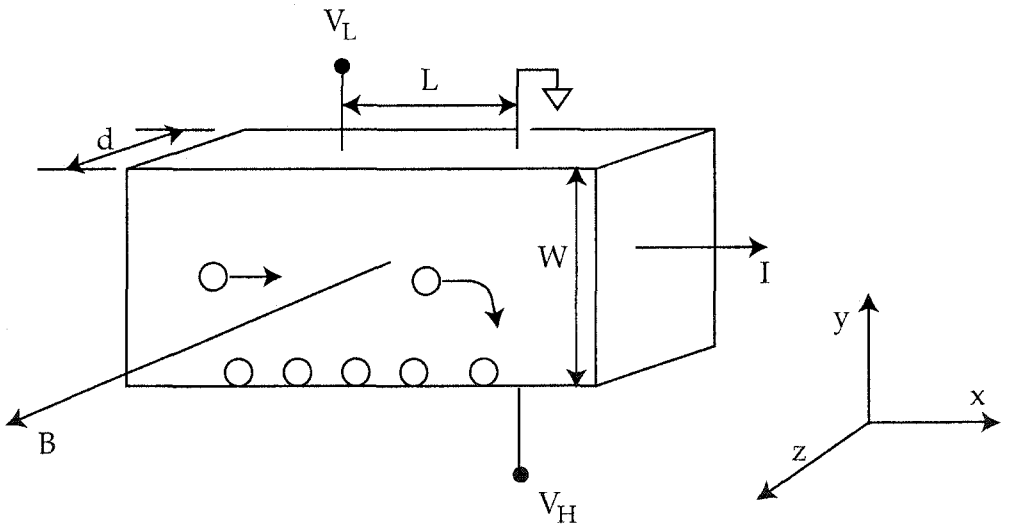

Figure 3.1 Diagram illustrating the Hall effect in a p-type sample.

Consider a p-type semiconductor sample shown in Figure 3.1 [69]. Note that the carriers in the p-type semiconductor are holes with positive charges. A control current, I, flows in the x-direction and a uniform magnetic field, B, is applied in the z-direction, as indicated

in Figure 3.1. The Hall current is given by

$$I = qAnv_x = qWdnv_x. \tag{3.1}$$

In the above equation, n is the carrier density, q is the carrier charge where $q = 1.6\times10^{-19}$C, A is the cross-sectional area, W and d are the width and thickness of the Hall sample as shown in Figure 3.1, v_x is the carrier velocity in the x-direction. For a uniform field in the z-direction, the force on the holes, which is called Lorentz force, is given by

$$\mathbf{F_m} = q(\mathbf{v}\times\mathbf{B}) = qv_xB(-\hat{x}). \tag{3.2}$$

The magnetic field, in conjunction with the current, forces some of the holes to be deflected to the bottom of the sample. For an n-type sample, the electrons will also be deflected to the bottom of the sample for the same current direction as that in Figure 3.1. The holes accumulate at the bottom surface leading to a vertical electrical field E_y. Thus a voltage $V_H = WE_y$ can be measured between the top and bottom surfaces. At equilibrium, the Lorentz force is balanced by the vertical electrical field, thus

$$F_m = qE_y = \frac{qV_H}{W}. \tag{3.3}$$

Substitute equation (3.1) and (3.2) into (3.3), the Hall voltage V_H is given by

$$V_H = \frac{BI}{qdn}. \tag{3.4}$$

The Hall voltage can also be expressed in terms of the supply voltage V_L. Note the supply current is

$$I = \frac{V_L}{R} \tag{3.5}$$

where R is the resistance of the Hall sample

$$R = \frac{\rho L}{Wd}, \tag{3.6}$$

ρ is resistivity. Using the relationship

$$\rho = \frac{1}{q\mu_H n} \tag{3.7}$$

where μ_H is the electron mobility, and substituting (3.5) and (3.6) into (3.4), one gets

$$V_H = \mu_H B \frac{W}{L} V_L. \tag{3.8}$$

The voltage sensitivity S_V can be defined as

$$S_V = \frac{\Delta V_H}{\Delta B \Delta V_L}. \tag{3.9}$$

From (3.8), it can be expressed as

$$S_V = \mu_H \frac{W}{L}. \tag{3.10}$$

The current sensitivity, S_I, can be defined as

$$S_I = \frac{\Delta V_H}{\Delta B \Delta I}. \tag{3.11}$$

From (3.4),

$$S_I = \frac{1}{qdn}. \tag{3.12}$$

Sometimes current sensitivity is also called the open circuit (unloaded) product sensitivity constant, K_H.

As shown in equation (3.10), Hall sensor sensitivity is directly proportional to the carrier electron mobility μ_H, which is material dependent. Typical electron mobilities (in $cm^2V^{-1}S^{-1}$) are: Si = 1.45×10^3, GaAs = 8.5×10^3, InAs = 2.26×10^4 and InSb = 7.5×10^4.

Hall sensor sensitivity is also inversely proportional to the thickness of the Hall plate. The thinner the Hall plate, the higher the sensitivity, as is shown in equation (3.12). The thickness of a Hall plate is limited by manufacturing methods and handling procedures. However, there is a design tradeoff between sensitivity and resistance. As the thickness of the Hall plate decreases, its resistance also increases. Typically, low input and output resistances are desired. A low input resistance decreases the voltage drop and reduces the power consumption and device self heating. A low output resistance allows the load resistor to be low, which in turn lowers the overall noise of the design.

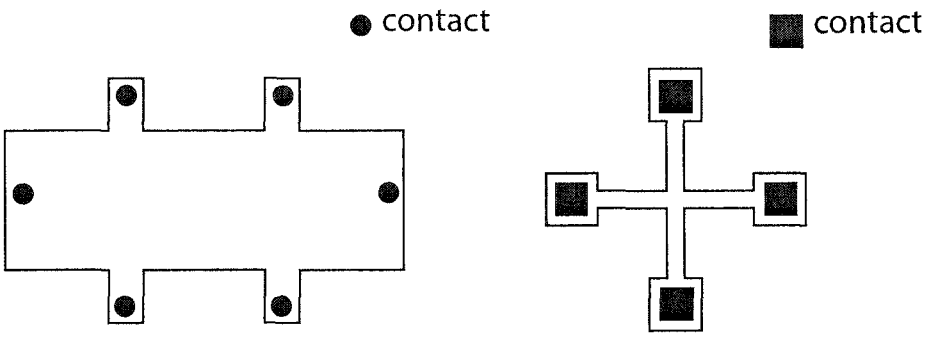

Figure 3.2 (a) Bridge-type Hall sample, (b) lamella-type van der Pauw Hall sample.

Another factor to affect the Hall sensor sensitivity is device geometry. For a simple shape as shown in Figure 3.1, equation (3.10) indicates the relation between device geometry and sensitivity. Figure 3.2 shows a bridge-type Hall sample and a lamella-type van der Pauw Hall sample [60]. Given the same supply current, different sample geometry and shape will lead to different current pattern and result a different sensitivity. The selection of the geometry involves trade-offs between product sensitivity, linearity and device resistance.

When selecting Hall sensors, a number of design parameters must be considered including Hall plate material, operating temperature range, sensitivity, temperature performance, packaging, frequency response, input and output resistance, linearity, cost, etc. Table 3.1 shows the parameters for some commercial available Hall sensors. Values shown in the table are obtained from manufacture's data sheets [62–65].

3.3 Hall sensor fabrication and testing

3.3.1 Fabrication of Hall sensors

The fabrication process of Hall sensors involves three steps. The first step is to deposit the desired material (GaAs, InAs, InSb, metal, etc.) on a certain substrate. The second step is to pattern the deposited film using photolithographic techniques. The third step is

Table 3.1 Parameters for some commercial available Hall sensors.

Device	material	sensitivity ($mVT^{-1}mA^{-1}$)	$R_{in}(\Omega)$	$R_{out}(\Omega)$	Temp.coef.of $V_H(\%°C)$	Temp.coef.of $R_{in}(\%°C)$
[1]FH – 560	InAs	12	80-160	150-480	-0.1	+0.1
[1]GH – 700	GaAs	100-280	450-900	1000	-0.07	0.15
[1]SH – 400	InSb	580-2240	240-550	240-550	-1.8	-1.8
[2]HG106C	GaAs	160	650-850	650-850	-0.06	0.3
[2]HW105A	InSb	610-1350	250-450	250-450	-1.8	-1.8
[3]P2	*	180	780	780	-0.04	-
[3]P15A	*	1000	4000	4000	-0.09	0.3

* complex material InGaAs-AlGaAs-GaAs as shown in Figure 3.14.
[1] Made by F.W.Bell, USA.
[2] Made by Asahi Kasei Electronics Co., Japan.
[3] Made by Advanced Hall Sensors Ltd., Manchester, United Kingdom.

to deposit a layer or several layers of metal and to pattern them using photolithography in order to form the desired metal contacts.

Figure 3.3 illustrates the basic photolithography process [60]. A light sensitive photoresist is spun onto the wafer forming a thin layer on the surface. The resist is then selectively exposed by shining light through a mask which contains the pattern information for the particular layer being fabricated. Then the photoresist is developed, so that the exposed region can be washed away. The next step is etching, during which the remaining photoresist acts as an etch mask to the material beneath it. Regions uncovered by photoresist are removed by the etch solution, thus completing the pattern transfer from the mask to the wafer. Finally, all the remaining photoresist is removed.

The above procedure can be repeated to pattern several different layers of semiconductor material or metal. The modern photolithography technique enables us to integrate multiple components on a single wafer and to interconnect them. Using this technique, Hall arrays that are connected in series or parallel can be fabricated on a single wafer.

Some Hall sensors were fabricated and their basic physical characteristics were measured at the Microelectronics Research Center (MRC), Iowa State University.

First a GaAs sample is grown using the molecular beam epitaxy (MBE) technique. A semi-insulating GaAs substrate is mounted inside a vacuum chamber and heated to 600°C

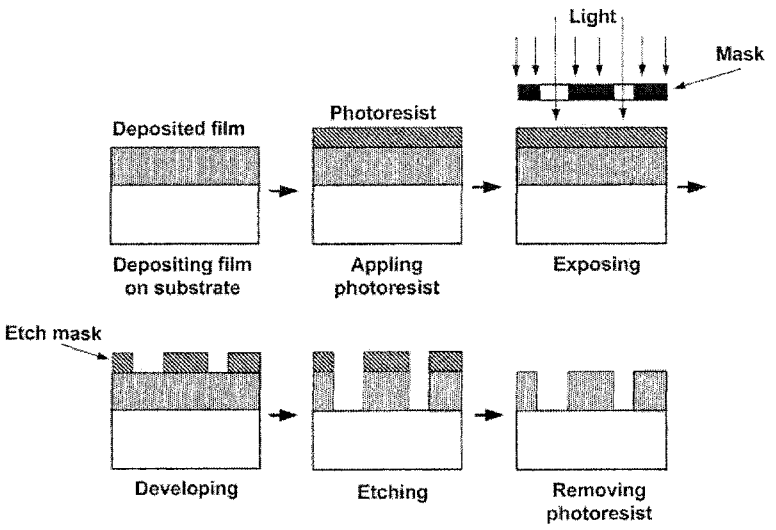

Figure 3.3 Basic photolithography process.

at a pressure of 10^{-10} Torr. Different source beams including gallium (Ga) and arsenic (As) are heated and introduced into the chamber. Once a gallium atom gets to the surface of the substrate, it has enough surface mobility to move around and position itself in the most energetically favorable location. In contrast, an arsenic atom has low surface mobility. It will fly off the substrate unless it happens to hit a position adjacent to a gallium atom. Thus, with the MBE technique, one can grow crystal of very good quality and ensure that the carrier structure, thickness and carrier density are well controlled. The semi-insulating GaAs substrate has very high resistivity (107 Ω·cm), therefore it can act effectively as an insulating substrate. However, the epitaxial layer is doped with the desired carrier density and hence has a higher conductivity.

After a sample of GaAs was grown, it was cut to form a 6 mm×6 mm square. Indium foil was cut into tiny dots and pressed onto each corner of the GaAs square to make temporary contacts, Figure 3.4. Then the sensor was sintered in a furnace at a temperature of 400°C for 15 minutes to insure the contacts were well attached to the GaAs.

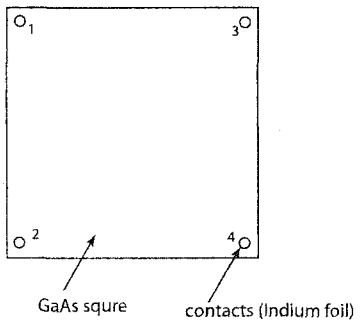

Figure 3.4 Van der Pauw Hall sensor made of GaAs square.

3.3.2 Testing of the Hall sensors

Two different van der Pauw sensors (VDP1 and VDP2) were made using GaAs. Their properties were measured. The results are listed in Table 3.2. The methods for measuring these parameters are discussed below.

Table 3.2 Measurement results for Hall sensors VDP1 and VDP2.

properties	VDP 1	VDP 2
d (μm)	1.25	2.75
$R_{12,34}(\Omega)$	60	8.038
$R_{14,23}(\Omega)$	24	13.558
F	0.92	0.96
$\rho(\times 10^{-2}\Omega \cdot \mathrm{cm})$	2.21	1.29
$\mu_H(\mathrm{cm^2V^{-1}s^{-1}})$	4301	3816
n ($\mathrm{cm^{-3}}$)	6.61×10^{16}	1.27×10^{17}

In Table 3.2, thickness (d) of the GaAs sample was determined by the settings of the MBE system when it was grown. Resistance $R_{12,34}$ was measured by injecting a current through connections 1 and 2, and measuring the voltage between connections 3 and 4, Figure 3.4. $R_{14,23}$ was measured in a similar way by injecting current through the connections 1 and 4, and measuring voltage between connections 2 and 3. The resistivity ρ was determined by the following equation

$$\rho = \frac{\pi d}{\ln 2} \frac{R_{12,34} + R_{14,23}}{2} F \tag{3.13}$$

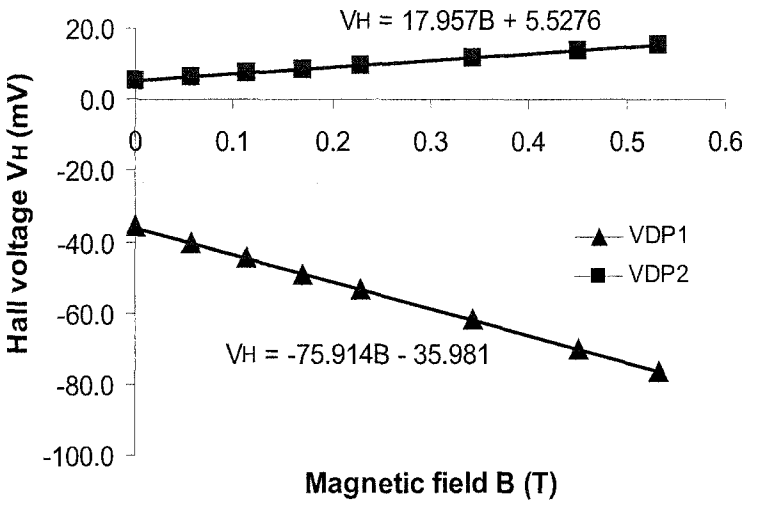

Figure 3.5 Relation between Hall voltage and magnetic flux density for Hall sensor VDP1 and VDP2.

where F is a correction factor. F is a function only of the ratio $R_r = R_{12,34}/R_{23,41}$, satisfying the relation [60]

$$\frac{R_r - 1}{R_r + 1} = \frac{F}{\ln 2}\text{arccosh}(\frac{\exp[\ln 2/F]}{2}). \tag{3.14}$$

A figure showing the dependence of F on R_r can be found in [58] or [60].

To determine the mobility and carrier density, the Hall sensor was placed in a magnetic field generated by a pair of excitation coils. The magnetic flux density B, was controlled by changing the current through the coil. A current of 1 mA was passed through connections 1 and 3 of the Hall sensor and the Hall voltage V_H measured between connections 2 and 4, Figure 3.4. The results are shown in Figure 3.5. The gradient of the trend line in Figure 3.5 shows the average value of $\Delta V_H/\Delta B$. From equations (3.4) and (3.7), mobility

μ_H is calculated,

$$\mu_H = \frac{d\Delta V_H}{\rho I \Delta B}, \tag{3.15}$$

where I is the current through the Hall transducer (1 mA). The carrier density, n, can be calculated from the mobility and resistivity,

$$n = \frac{1}{\mu_H q \rho}. \tag{3.16}$$

The sensitivity of VDP1 and VDP2, named S_1 and S_2, can be calculated from the parameters in Table 3.2 using equation (3.12). The calculated results are $S_1 = 75.64\ VT^{-1}A^{-1}$ and $S_2 = 17.90\ VT^{-1}A^{-1}$. The sensitivity can be also be calculated with a different method. From Figure 3.5, $\Delta V/\Delta B$ of VDP1 and VDP2 are 75.91 mVT^{-1} and 17.96 mVT^{-1} respectively. Since the current through the Hall sample is 1 mA, one can get the sensitivity from equation (3.11). The results are $S_1 = 75.91\ VT^{-1}A^{-1}$ and $S_2 = 17.96\ VT^{-1}A^{-1}$. Sensitivity calculated with the two methods are consistent with each other.

It is obvious that the sensitivity of VDP1 is higher than that of VDP2, but both devices have lower sensitivities than most of the Hall sensors list in Table 3.1. More Hall sensors were fabricated at MRC using different structures and materials, results are shown in [59]. However, their performance is not satisfactory. As a result, Hall sensor P2, fabricated by Advanced Hall Sensor Ltd., was chosen to build a high density linear Hall array probe. P2 sensors were fabricated in arrays on a single wafer using the photolithographic techniques. More details will be covered in section 3.5. Because it takes quite long time to finish the design and fabrication process, Hall sensor HW105A, made by Asahi Kasei Electronics Co., was chosen to build a prototype eight-element linear Hall array probe, before the P2 Hall sensor arrays were available. Design and testing of the prototype probe are described in the following section.

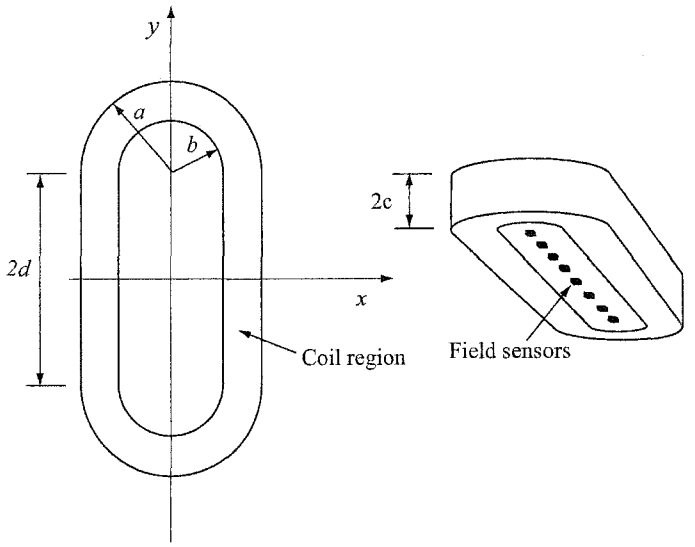

Figure 3.6 Linear array probe with racetrack coil and eight Hall sensors.

3.4 Eight-element linear Hall array probe

3.4.1 Probe design

An eddy current probe was designed and built with eight Hall sensor ICs in a linear array excited by a racetrack coil. In plan view, the racetrack coil has the shape of a running track with semicircular bends connected by straight sections as shown in Figure 3.6.

A coil former was constructed of Ultem, a material that is dimensionally stable and features high strength at temperatures up to 170°C. Before winding the coil on the former, some non-stick cooking spray was applied to the former to act as a releasing agent. The coil (shown in Figure 3.7) was wound using 36 AWG bondable magnet wire. After winding, the coil, together with the former, was heated to 135°C for 30 minutes in order to bond the windings together. The coil was then removed from the former after it was cooled down. The coil dimensions are shown in Table 3.3.

A row of eight HW105A Hall sensors [62] were mounted at 3 mm centers on the edge of

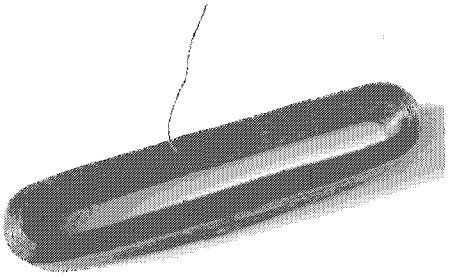

Figure 3.7 Picture of the racetrack coil.

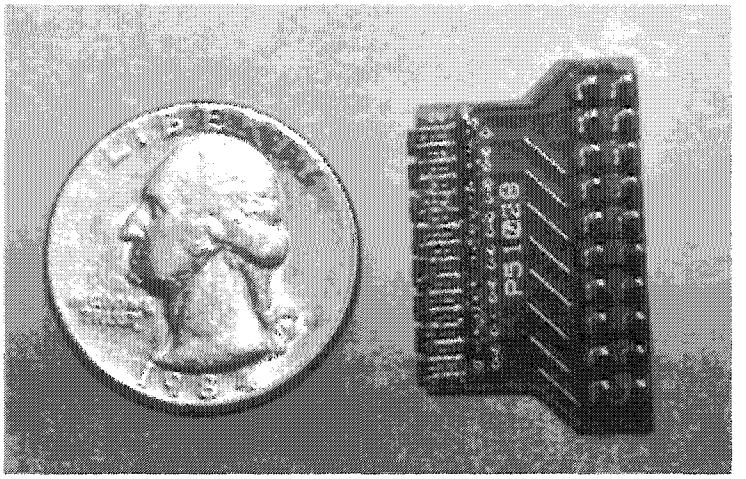

Figure 3.8 Picture showing the PCB with 8 HW105A Hall sensors mounted on its edge.

Table 3.3 Dimensions of the racetrack coil.

Inner Radius (b)	1.60 mm
Outer Radius (a)	3.89 mm
Length of the Straight Part (2d)	28.00 mm
Hight (2c)	5.99 mm
Number of Turns	517

a small printed circuit board (Shown in Figure 3.8). The HW105A Hall sensors, provided by Asahi Kasei Electronics Co, are made of Indium Antimonide (InSb) with high mobility of 75,000 $cm^2/Vsec$. Parameters of HW105A can be found in Table 3.1 and reference [62]. The sensor array circuit board and the racetrack coil were mounted together using a casting resin.

3.4.2 System and electric hardware design

Figure 3.9 shows the block diagram of the test system for the eight-element Hall sensor array probe. The signal generator provides a drive source for the probe coil. Signals from each Hall sensor are AC coupled to amplifiers (one amplifier for each Hall sensor). The gains of the amplifiers are adjusted so that each channel will give the same level of output in a uniform field. The amplified Hall sensor signal is fed to a multiplexer (MUX), which selects one of the eight channels in turn to an analog multiplier AD633. One of the amplified Hall signals is connected to a zero-crossing detector, which converts the sine-wave to a square-wave signal, the latter is counted by a frequency divider composed of three synchronous binary counters in series. The output binary digits from the last counter (from 000 to 111) provide a channel-selecting signal to the multiplexer. When the counters reset themselves, the last counter generates a carry-out signal to reset a ramp generator simultaneously. The ramp generator provides a linear ramp signal to be the x-sweep signal for an oscilloscope.

Figure 3.10 is the schematic diagram for the zero crossing detector that converts the sine-wave to a square-wave signal.

Figure 3.11 shows the schematic diagram for the linear ramp generator. Capacitor C_2

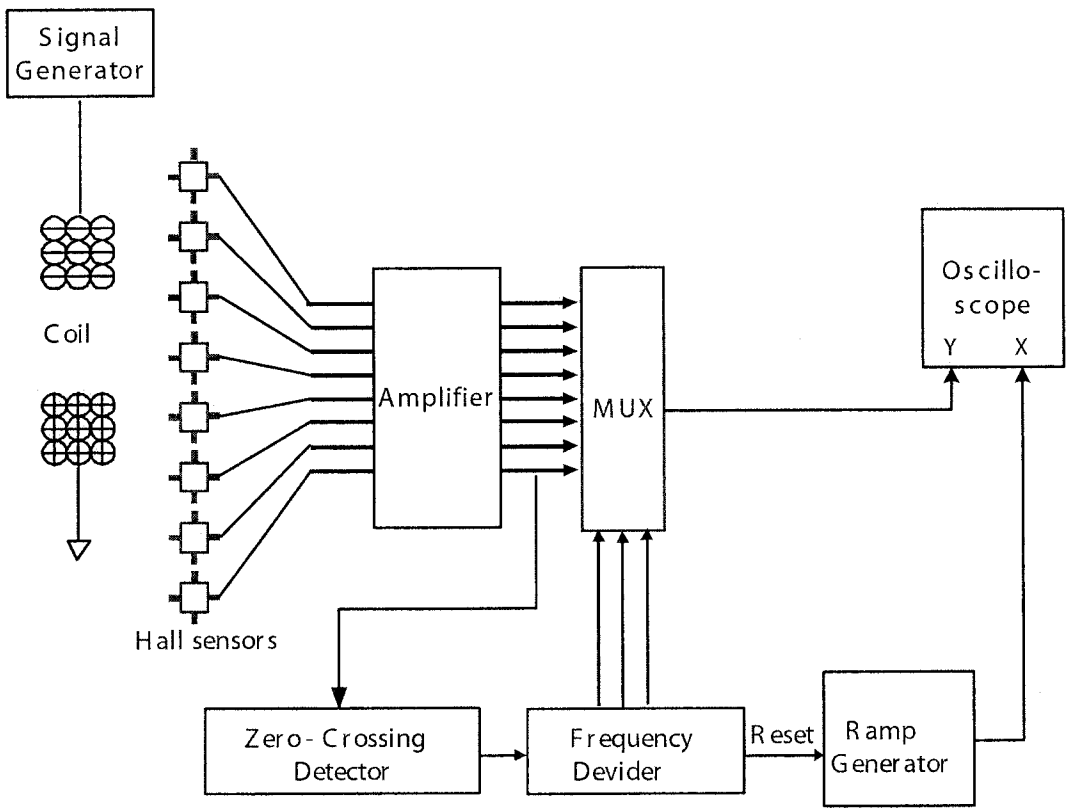

Figure 3.9 Diagram of the test system for the eight-element Hall sensor array probe.

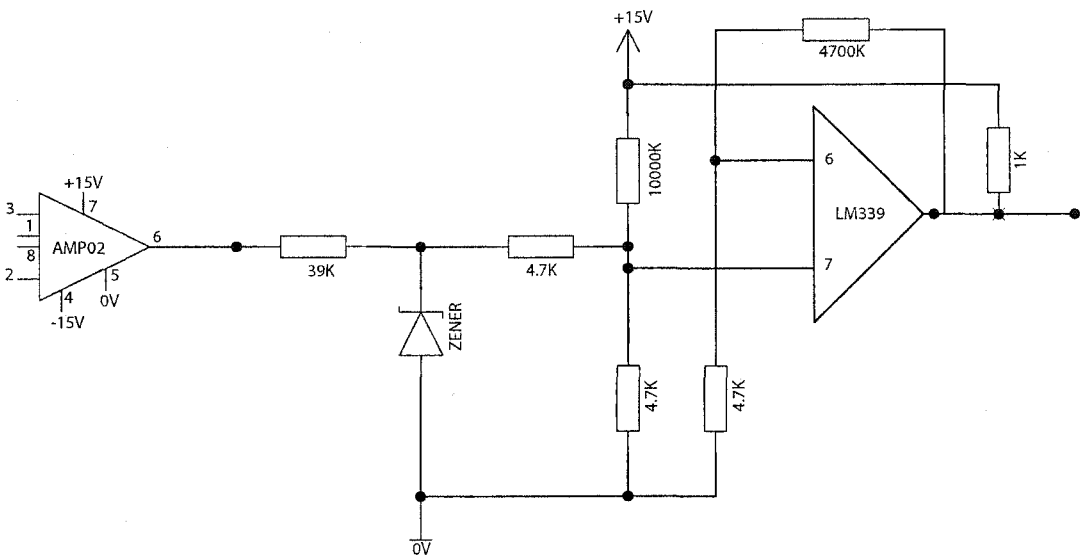

Figure 3.10 Zero crossing detector circuit schematic.

is charged up linearly by a current source consisting of a PNP transistor, R_1, R_2 and R_E. The constant current from the current source is

$$I_C = \frac{\frac{R_1 V_{cc}}{R_1+R_2} - V_{BE}}{R_E} \tag{3.17}$$

where the base-emitter voltage $V_{BE} = 0.6V$. The voltage on C_2 varies linearly with time t as

$$V_{C2} = \frac{I_C}{C_2} t \tag{3.18}$$

until at some point, it is discharged through a 555 timer.

The charge/discharge behavior of the capacitor C_2 is controlled by a 555 timer chip. The trigger and threshold pins of the 555 timer are connected to each other. When the voltage on them is lower than $\frac{1}{3}V_{CC}$, discharge is enabled. When it is higher than $\frac{2}{3}V_{CC}$, discharge is disabled. The control signal to trigger/threshold the 555 chip comes from a monostable multivibrator 74HC123, which upon receiving a carry-out (RCO) signal from the binary counter 74HC163, will generate a pulse signal whose pulse width (t_W) is determined as [66]

$$t_W = R_3 C_3. \tag{3.19}$$

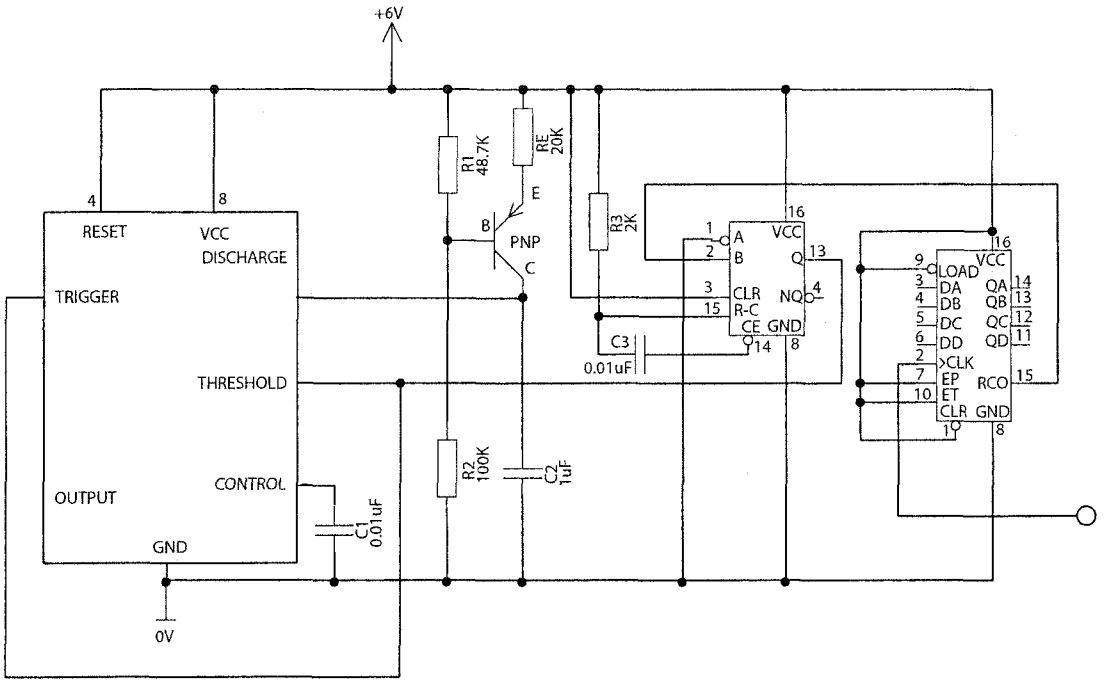

Figure 3.11 Ramp generator circuit schematic.

This pulse width is set to be very short so that there is almost no "dead zone" for the ramp signal.

3.4.3 Test results

The eight-element Hall sensor array probe was placed on the top of a circular coil with the sensor array along the radius of the circular coil. Figure 3.12 shows the ramp signal together with probe signal. The x-axis is the time axis. The y-axis is the scale of the signal level. The higher level steps correspond to the sensors near the center of the circular coil, where the field is stronger, and the lower steps correspond to the sensors near the edge of the coil where the field is weaker. Note that when the probe output switches from the last sensor to the first sensor, the ramp signal resets quickly at the same time.

Figure 3.13 displays the signal when the probe was placed on an aluminum plate with a long and narrow electrodischarge machined (EDM) slot. The sensor array was aligned in

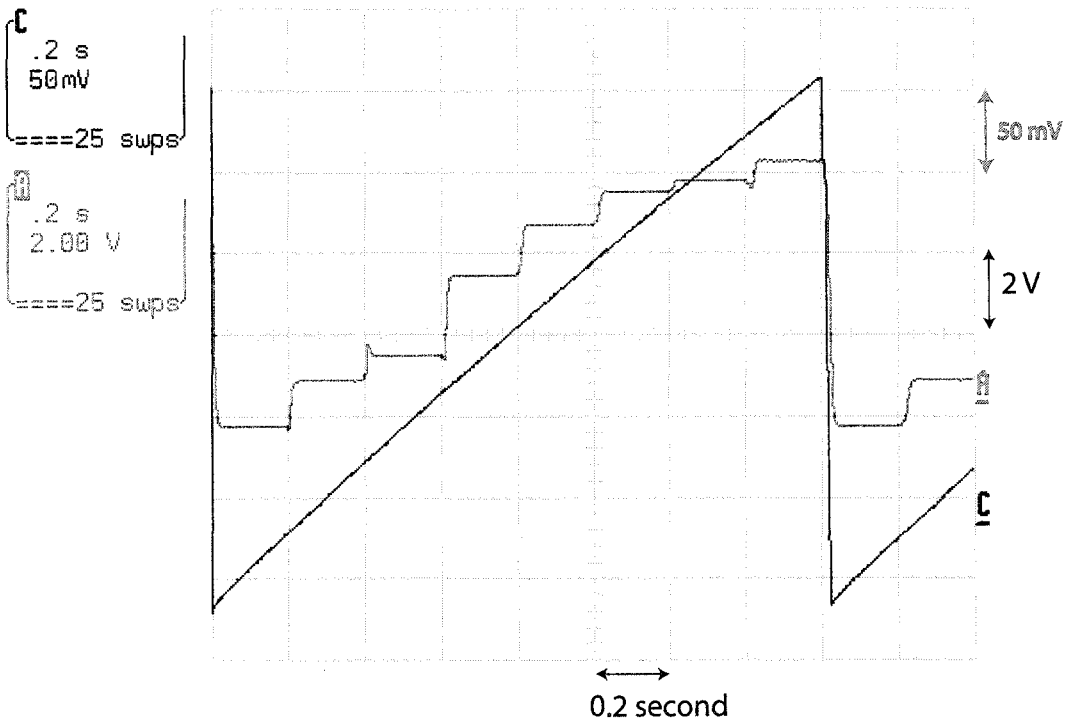

Figure 3.12 Ramp signal (A) and probe signal (C) when the probe was placed along the radius of a circular coil. X-axis is time with a grid of 0.2 second. Y-axis is the signal level. The grid for the ramp signal (C) is 50 mV and the grid for the probe signal is 2V.

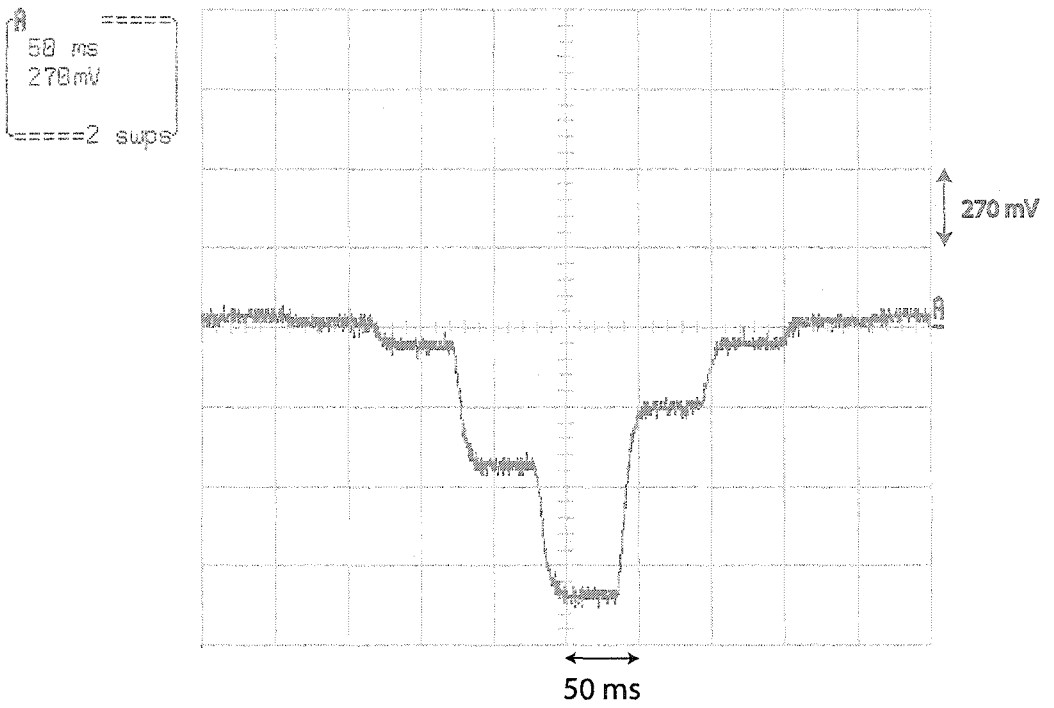

Figure 3.13 Signal displayed on the screen of the oscilloscope when the array probe is placed on an aluminum plate with a long EDM slot. The lowest step represents the location of the slot.

a direction perpendicular to the EDM notch. The x-axis is the time axis and the y-axis is output signal from the probe. The lowest step represents the location of the groove.

3.5 High density linear Hall array probe

3.5.1 Design of the Hall sensor arrays

The Hall sensors, P2, grown by a molecular beam epitaxy (MBE) system on a 2-inch wafer were obtained from the University of Manchester Institute of Science and Technology in the United Kingdom. They are new two-dimensional electron gas (2DEG) Hall devices which were designed using the AlGaAs-InGaAs structure shown in Figure 3.14. The sensors are designed for low magnetic field measurement of the order 1 μT with a magnetic field amplitude resolution of a few hundred nanoTesla [57]. The characteristics of the P2 Hall sensor are given in Table 3.4. Some of the characteristics of the P2 Hall sensor are compared with other commercial available Hall sensors in Table 3.1. Parameters of the 2DEG Hall sensors such as P2 and P15A are controllable at the material level (wafer growth) [65]. Although P2 has a lower sensitivity than P15A, its input resistance is also lower. A lower input resistance is desirable for Hall sensors that are to be operated in series because it requires lower supply voltage to achieve the same current. The very high supply voltage could result in complete device failure in the event of a short circuit.

Two types of arrays were fabricated on a single wafer: one with the devices connected in series and the other with them connected in parallel, Figure 3.15. While the series arrays are suitable for constant current drive, the total input resistance will be very high. The arrays in parallel are suitable for constant voltage drive and have low input resistance which requires a low supply voltage. Both types of arrays will be investigated to determine the best configuration. The two array types are fabricated in the central region of a single wafer while some individual devices populate the region near the border. This arrangement was used because the center of the wafer has more uniform properties than in the border region due to the fabrication process.

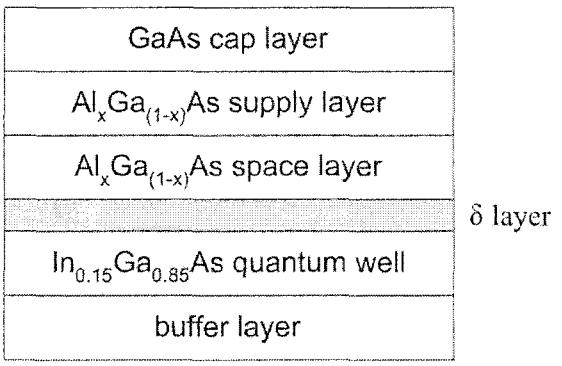

Figure 3.14 Epitaxial structure of the Hall effect sensor (P2)

Table 3.4 Characteristics of the P2 Hall sensors.

Parameters	Value	Units
Nominal control current	1.5	mA
Input resistance	680	Ω
Output resistance	680	Ω
Mobility	6500	cm^2/V sec
Current sensitivity	180	V/AT
Current sensitivity drift over temperature	-0.08	% °C
Power consumption for $V_{in} = 1V$	1.4	mW
Linearity of Hall voltage	1	%

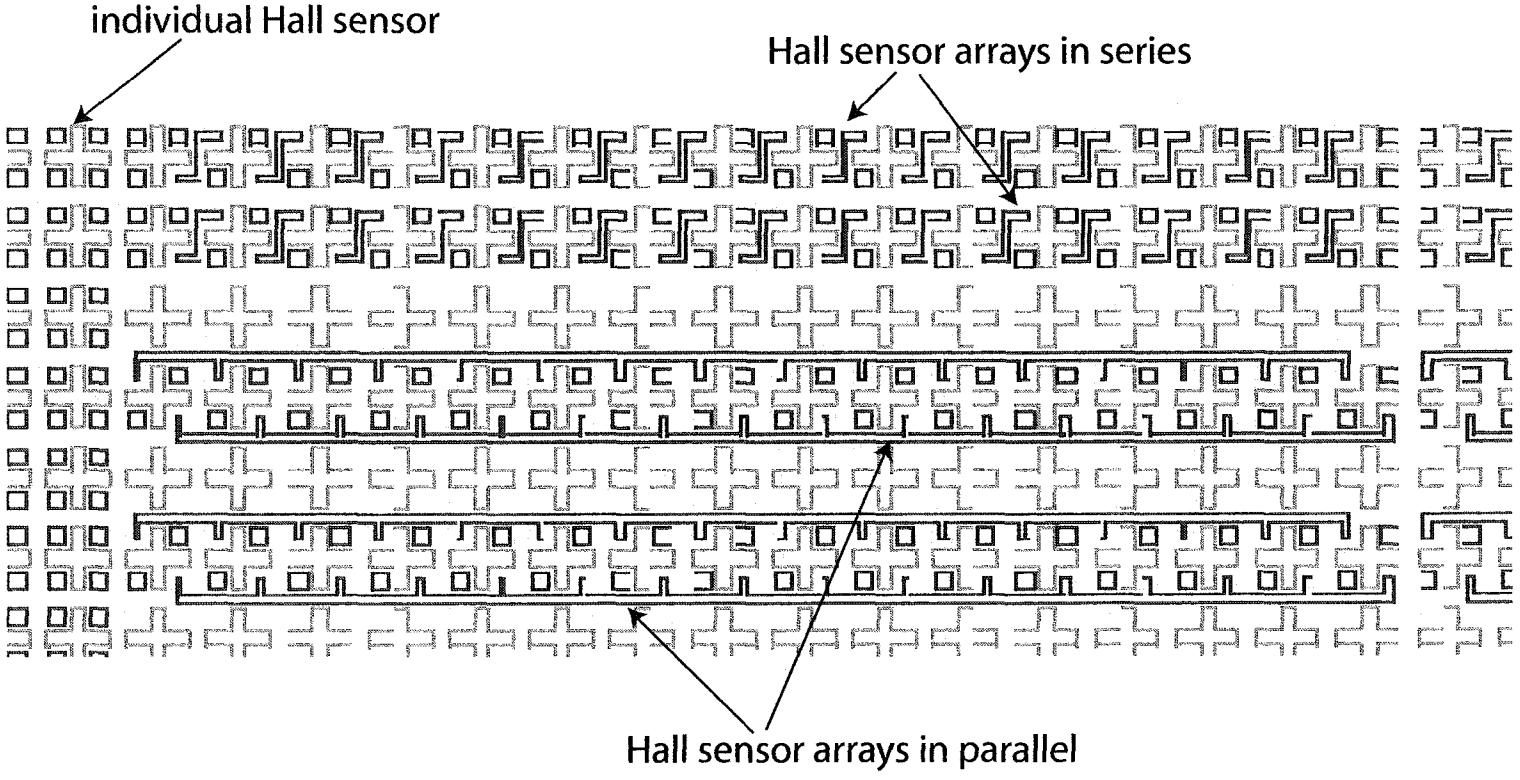

Figure 3.15 Part of the design for a 2-inch wafer, which contains 16- element Hall arrays connecting in series or parallel in the central region and some individual Hall sensors near the boarder.

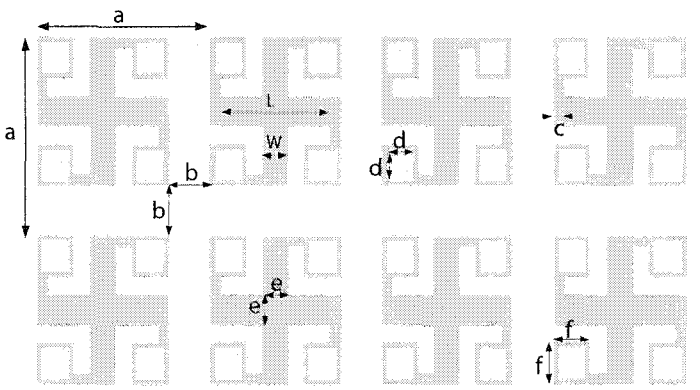

Figure 3.16 Geometries of the Hall sensor arrays. The dimensions shown in the figure are $a = 400\mu m$, $b = 90\mu m$, $c = 70\mu m$, $d = 80\mu m$, $e = 50\mu m$, $f = 100\mu m$, $W = 70\mu m$, $L = 210\mu m$. Note that the tracks connecting between sensors are not shown.

The Hall devices are in the form of a square Greek cross with four Ohmic contacts for each sensor, Figure 3.16. The device structure is fully symmetrical and thus input and output resistances are equal. Each array has 16 elements with conductive tracks connecting them. The connecting tracks are made by thermal evaporation of titanium followed by gold. The arrays and individual devices have a pitch of 400 microns.

3.5.2 Probe design

A printed circuit board (PCB) was designed with a long slot in the center for holding the Hall sensor arrays, Figure 3.17. Two Hall arrays, each having 16 Hall sensors, were glued in the slot. Each Hall sensor has two current supply contacts and two Hall signal contacts. The current supply contacts were connected by tracks on the wafer for either series or parallel operation as mentioned above. The Hall signal contacts are wire-bonded to pads on the PCB. These pads are then connected to two insulation displacement cable (IDC) headers on the edges of the PCB by copper tracks. Pairs of copper tracks associated with an individual Hall sensor are routed directly opposite one another on two different layers. The purpose of this layout is to minimize the induction in the circuit loop. Figure 3.18

shows the dimensions for the Hall arrays in the PCB slot.

There are three options to arrange the coils and the sensor array, Figure 3.19. Option A uses one racetrack coil with the Hall array placed along the central line of the coil, where the magnetic field intensity is perpendicular to the Hall sensor surface. This generates a strong background signal due to the coil itself. Furthermore, the field at two ends of the array is different from that at its center. Thus, although option A is simple, it suffers from a strong background signal and end effects. Options B and C use two racetrack coils with the Hall array placed between them. The currents flowing in the two coils are of the same magnitude but in the opposite directions (one in the clockwise direction and the other in the counter-clockwise direction). In option C, the Hall array is placed exactly between the two coils and along the coil tracks, where the magnetic fields generated by two coils cancel completely. Therefore, there is no background signal. In option B, the Hall array is placed between the coils and across the coil tracks, where the fields are partly cancelled by each other and the background signal is weak compared with option A. But the field is non-uniform along the Hall array. For option A and B, it is necessary to null the background signal before measurements.

3.5.3 Circuit system design

The block diagram of the Hall array system is shown in Figure 3.20. The racetrack coil is excited by a current source through a sensing resistor. Hall sensors can be supplied by either DC voltage or AC voltage. Both will be discussed in this chapter. The signal from each Hall sensor is connected to detector circuits, which will be discussed in details below. Each channel contains one detector circuit. The voltage across the sensing resistor is amplified to serve as a reference signal to the detector circuits. This amplified voltage can be connected to the detector circuit directly as an in-phase reference or through a phase-shifter to give a quadrature reference. A switch is used to toggle between the two reference signals.

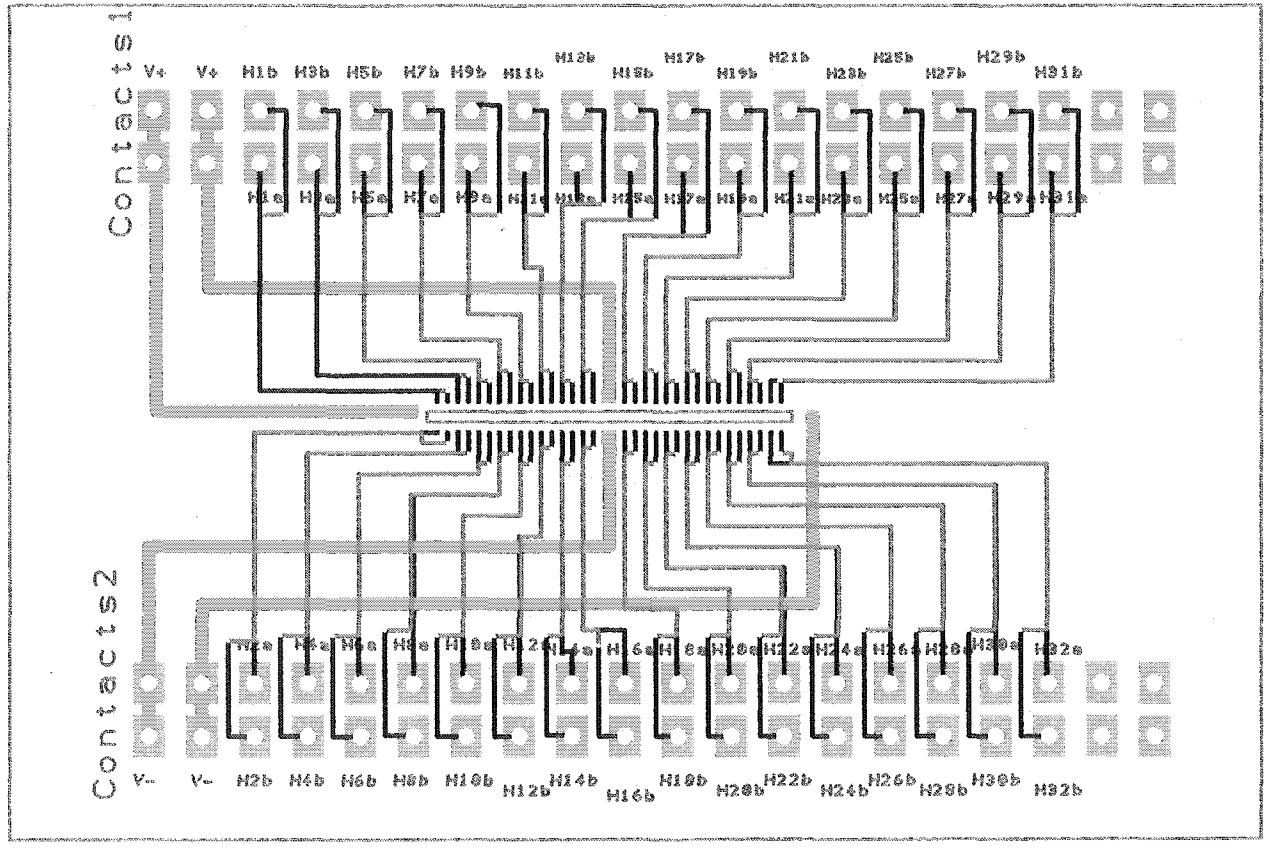

Figure 3.17 A printed circuit board (PCB) with a long slot in the center. To minimize pick-up voltages in the track loops, pairs of copper tracks associated with an individual Hall sensor are routed directly opposite one another on two different layers.

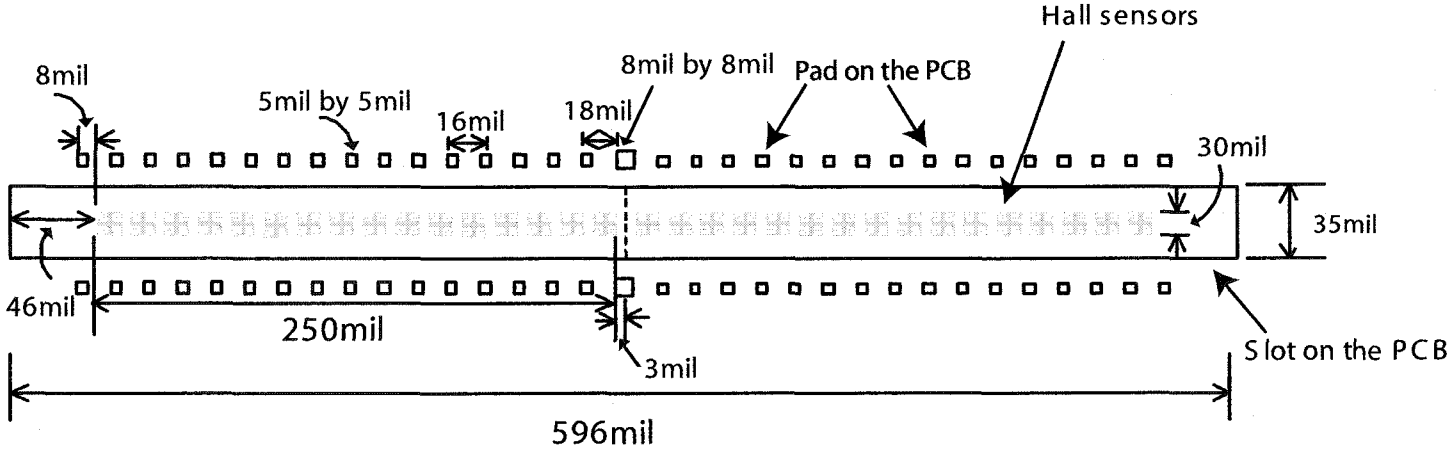

Figure 3.18 Dimensions for two Hall arrays in the PCB slot. The two Hall arrays, each having 16 Hall sensors, are wire bounded with the pads on the PCB. Note that connections between Hall sensors are not shown in the figure.

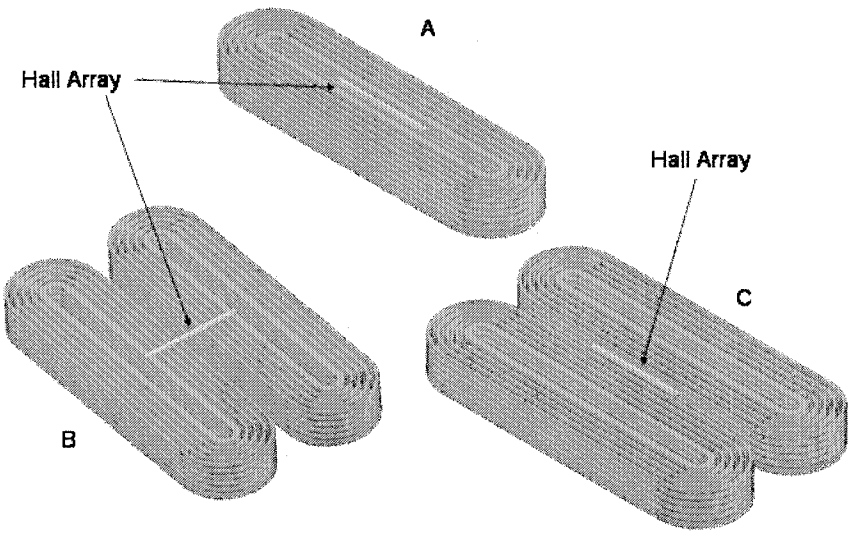

Figure 3.19 Different coils and Hall sensor array arrangements.

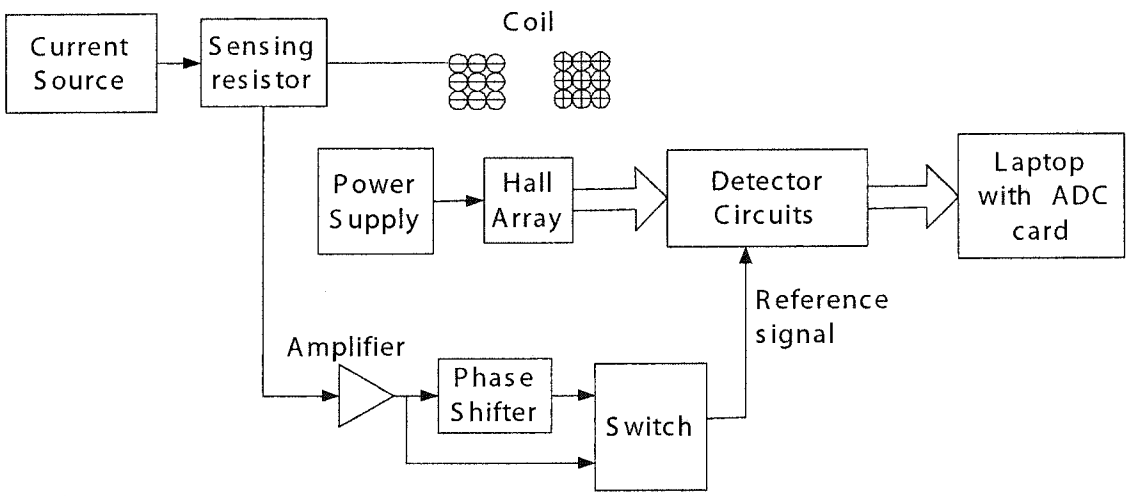

Figure 3.20 Block diagram of the Hall array circuit system.

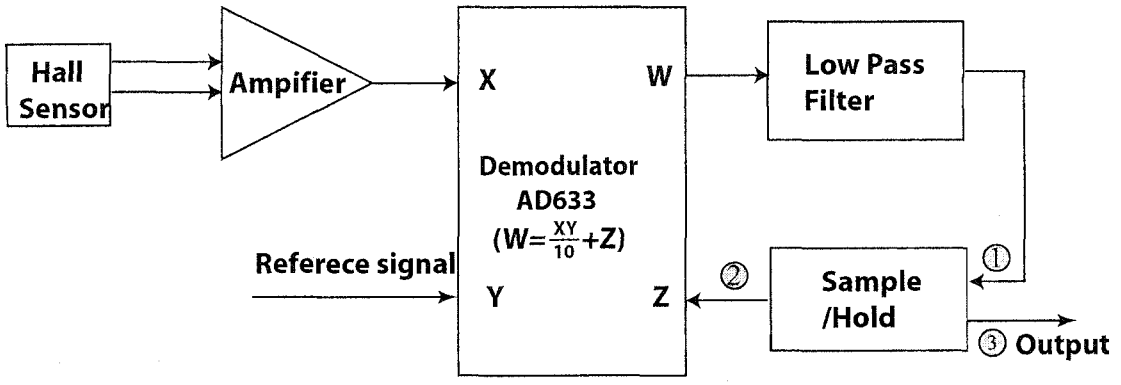

Figure 3.21 Block diagram of the detector circuit for one channel.

The block diagram of the detector circuit is shown in Figure 3.21 and the detailed schematic diagram is shown in Figure 3.22. The detector circuit (one for each Hall device) consists of four blocks: an amplifier, an analog multiplier AD633 (acting as a demodulator), a low pass filter and a sample-and-hold circuit. Each block is analyzed below.

The Hall signal from each sensor is AC coupled to a two-stage differential amplifier, each stage containing an instrumentation amplifier AD620 and a gain setting resistor. AC coupling can eliminate the DC offset of the Hall sensors as well as the DC offset from the AD620. The AC coupling is realized by a 100 kΩ resistor and a 0.1μF capacitor connected as a high pass filter. Due to differences in the Hall sensors, the gain resistors need to be adjusted in the calibration process before measurements to ensure all channels give the same signal level in a uniform field.

When the Hall sensor is supplied by a DC voltage (Hall sensors supplied by AC voltages will be discussed in the next section.) and placed in an AC magnetic field of frequency f_0, the frequency of the Hall signal is f_0 and the magnitude is proportional to the field intensity. However, it is desirable to have a DC signal instead of an AC signal oscillating at the field frequency. This is realized by using a demodulator, AD 633, and a low pass filter.

The AD633 is basically a multiplier that takes inputs X and Y and adds a third input,

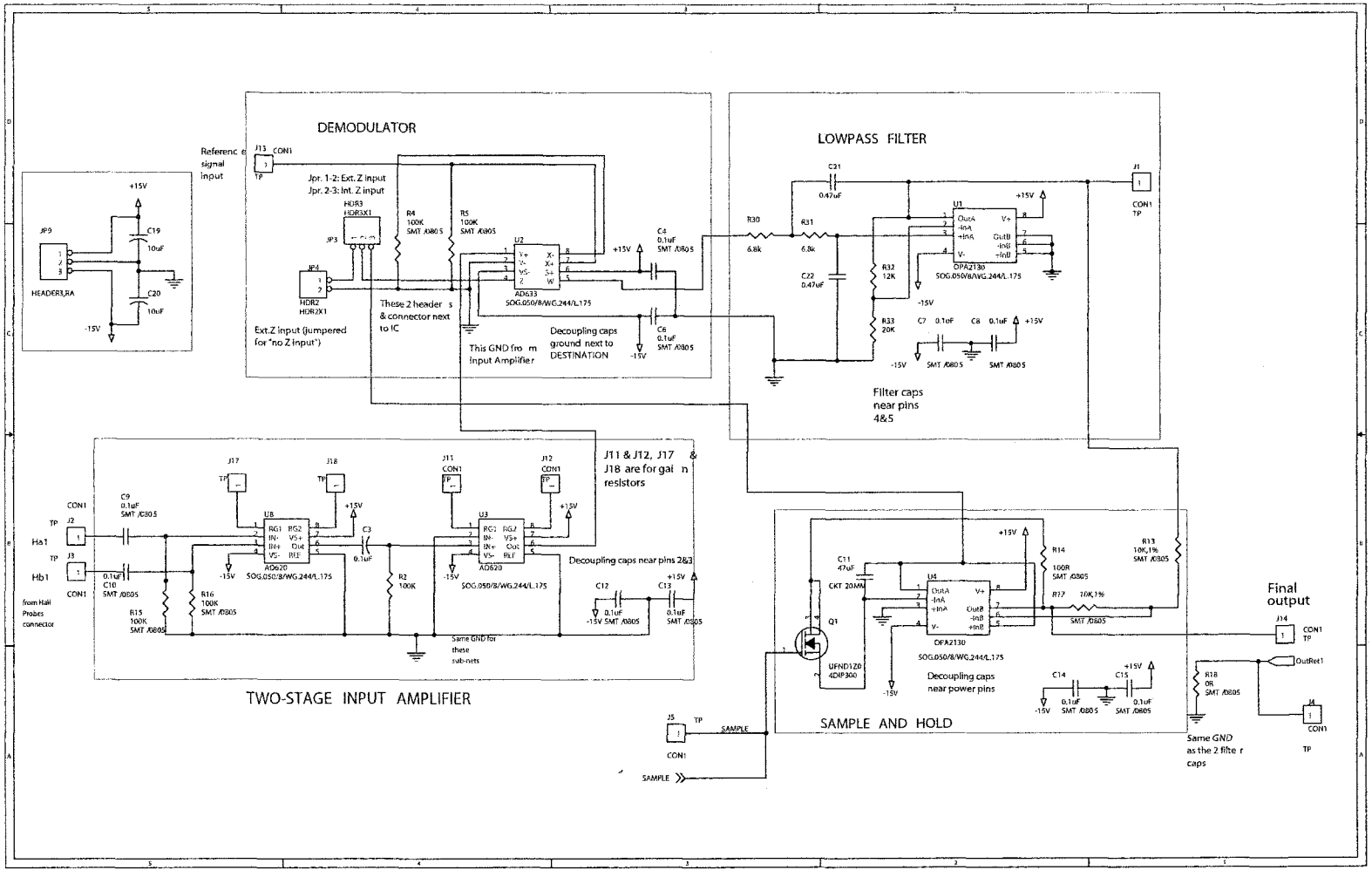

Figure 3.22 Schematic for one channel of Hall signal processing circuit which consists of input amplifier, phase demodulator, low pass filter and sample/hold circuit.

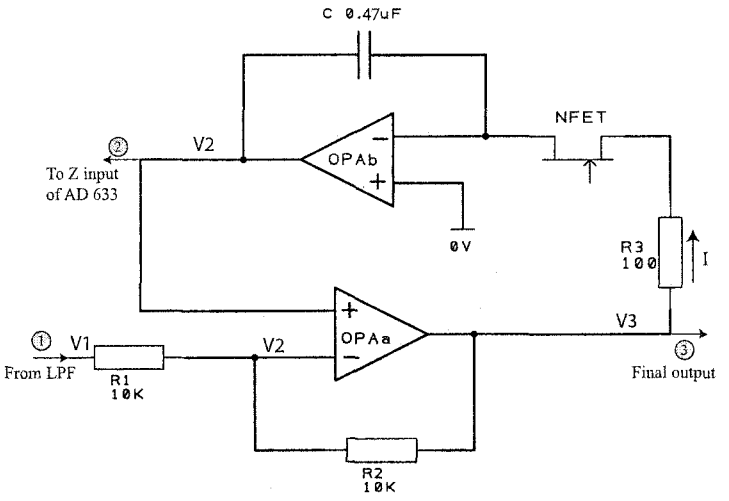

Figure 3.23 Schematic diagram for the sample and hold circuit.

Z. The output W is [76]:

$$W = \frac{XY}{10} + Z. \tag{3.20}$$

Here X is the amplified Hall signal at f_0. Y is the reference signal, coming from the sensing resistor as shown in Figure 3.20, whose frequency is also f_0. Z is a DC offset value and will be discussed later. The product of X and Y generates a DC level as well as an AC component at a frequency of $2f_0$. To eliminate the component at $2f_0$, the output (W) from the multiplier AD 633 are connected to a low pass filter (LPF) to give the DC level that is proportional to the magnetic field. The LPF is an active filter [77] with -3dB frequency at 50 Hz, which is set by R_{30}, R_{31}, C_{21} and C_{22} in Figure 3.22.

In normal operation, it is standard practice to null a conventional eddy-current probe, usually in the presence of an unflawed region of the specimen being inspected. The same is true of array probes, the only difference being that multiple channels must be nulled simultaneously. The sample and hold (S/H) circuit is included for this purpose.

A schematic diagram for S/H is shown in Figure 3.23. It has one input port (1) and two output ports (2 and 3). The N-channel MOS (metal-oxide-semiconductor) FET (field effect

transistor) acts as a switch. It is controlled by the gate voltage. When a positive voltage (+15V) is connected to the gate, the NFET is on. A negative voltage (-15V) at the gate turns the NFET off. This can be controlled by a push-button. There are two operational amplifier in the S/H circuit (termed OPAa and OPAb below.) OPAa is connected with R_1 and R_2 to form a unity-gain inverting amplifier. OPAb, R_3 and a capacitor C are configured as an integrator with a time constant of 4.7 milli-second (time constant $\tau = R_3C$). The output of OPAb is connected to the non-inverting input of OPAa to form a feed back loop.

Before analyzing the S/H circuit, two basic characteristics of an ideal operational amplifier (op-amp) are stated:

1. The input impedance of an ideal op-amp is infinite, thus there is no current flow into an ideal op-amp.

2. In normal operation, the two differential inputs are the same (it is called *virtual short.*)

Voltages V_1, V_2, V_3 are marked in Figure 3.23. Note that the two inputs to OPAa are V_2 and the two inputs to OPAb are both zero, according to the characteristic 2 stated above.

Since there is no current flow into OPAa, current through R_1 will also flow through R_2, thus

$$\frac{V_1 - V_2}{R_1} = \frac{V_2 - V_3}{R_2}. \tag{3.21}$$

Since $R_1 = R_2$, we have

$$V_3 = 2V_2 - V_1. \tag{3.22}$$

When the switch is on, the upper side of R_3 is 0V, the lower side of R_3 is V_3, which generates a current I through R_3 unless $V_3 = 0$. As an example, suppose $V_3 > 0$. The current I flows as shown in Figure 3.23. Since no current can flow into an op-amp, I charges the capacitor, which causes V_2 to decrease,

$$\frac{V_3}{R_3} = I = -C\frac{dV_2}{dt}. \tag{3.23}$$

Suppose V_2 decreases by ΔV. Note that V_2 is fed to the summing input (Z) of the AD633 (Figure 3.21). V_1, which is the output from the LPF, will also decrease by ΔV. According

to equation (3.22), V_3 will decrease by ΔV, too. V_3 will keep decreasing until $V_3 = 0$, when there is no current charging the capacitor. Thus the circuit reaches a balance. At this point, the sensor is said to be nulled.

When $V_3 = 0$, according to equation (3.22), $V_2 = \frac{1}{2}V_1$. Now if we turn the switch off, there is no path for the capacitor to be discharged. Voltage $V_2 = \frac{1}{2}V_1$ is stored on the capacitor. Next when V_1 varies to V_1', voltage at port 3 is:

$$V_3' = 2V_2 - V_1' = V_1 - V_1'. \tag{3.24}$$

Equation (3.24) shows that after the circuit is nulled, only the difference between the previous measurement and the new measurements will appear in the output. Thus gain can then be increased and small changes in the field seen by the Hall devices, such as those produced by a flaw, magnified.

3.5.4 Modulation of Hall signal

The Hall effect voltage (V_H) is given by

$$V_H = K_H I B \tag{3.25}$$

where K_H is the open circuit (unloaded) current sensitivity, I is the supply current to the Hall sensor and B is the magnetic flux density to be measured. The measured voltage contains not only V_H, but also an induced voltage V_{ind} due to the loop area of the connecting leads. To separate the induced voltage from the genuine Hall effect voltage, the principle of modulation is employed. Experiments have shown that the Hall signal can be modulated and demodulated in order to remove the induced voltage component. [78]

To modulate the Hall signals, the Hall sensor are supplied by an AC current at a frequency of ω_1, which varies sinusoidally with time as $I_0 \cos(\omega_1 t)$. This provides an another advantage over DC supply by avoiding the low frequency (1/f) noise, mainly generated by the Hall sensor [57]. The coil current excites eddy currents at another frequency ω_2, which generates the magnetic field as

$$B = B_0 \cos(\omega_2 t). \tag{3.26}$$

The Hall voltage can then be written as

$$V_H = K_H I_0 \cos(\omega_1 t) B_0 \cos(\omega_2 t) = \frac{1}{2} V_{H0}[\cos(\omega_1 + \omega_2)t + \cos(\omega_1 - \omega_2)t] \tag{3.27}$$

where $V_{H0} = K_H I_0 B_0$. From Faraday's law, the induction voltage (V_{ind}) in the connecting loop can be expressed as

$$V_{\text{ind}} = -\frac{d\Phi}{dt} \qquad \text{with} \qquad \Phi = \Phi_0 \cos(\omega_2 t) \tag{3.28}$$

where Φ is the magnetic flux linking the connecting leads. The induced emf will appear in the measured voltage as a term which increases linearly with frequency. Thus the total measured voltage is

$$V_T = \frac{1}{2} V_{H0}[\cos(\omega_1 + \omega_2)t + \cos(\omega_1 - \omega_2)t] + \Phi_0 \omega_2 \sin(\omega_2 t). \tag{3.29}$$

This expression shows that the measured voltage has three frequency components. Using a reference signal at $\omega_1 - \omega_2$, one can remove the induction voltage at ω_2 and only get the upper sideband of the modulated Hall signal. This can be realized by the demodulator and low pass filter designed in the previous section.

Figure 3.24 shows an example. Suppose the Hall sensor supply voltage is at f_1 =70kHz, while the coil excitation frequency is f_2 = 2kHz. The Hall signal is modulated and the measured signal includes the induction voltage. According to equation (3.29), the output signal from Hall sensor includes three frequency component at 72kHz, 68kHz and 2kHz respectively, Figure 3.24 (a). To remove the induction signal (2 kHz) and get only the upper sideband Hall signal (68 kHz), one can use the detector circuit in Figure 3.21 and set the reference source at 68kHz, Figure 3.24 (b). When the reference signal is multiplied with the three components in the Hall signal, it generates different frequency components as shown in Figure 3.24 (c). After passing through a low pass filter whose -3 dB frequency is at 50 Hz, Figure 3.24 (e), only DC signal remains which represents the level of the upper sideband of the modulated Hall signal while the induction signal is removed, Figure 3.24 (e).

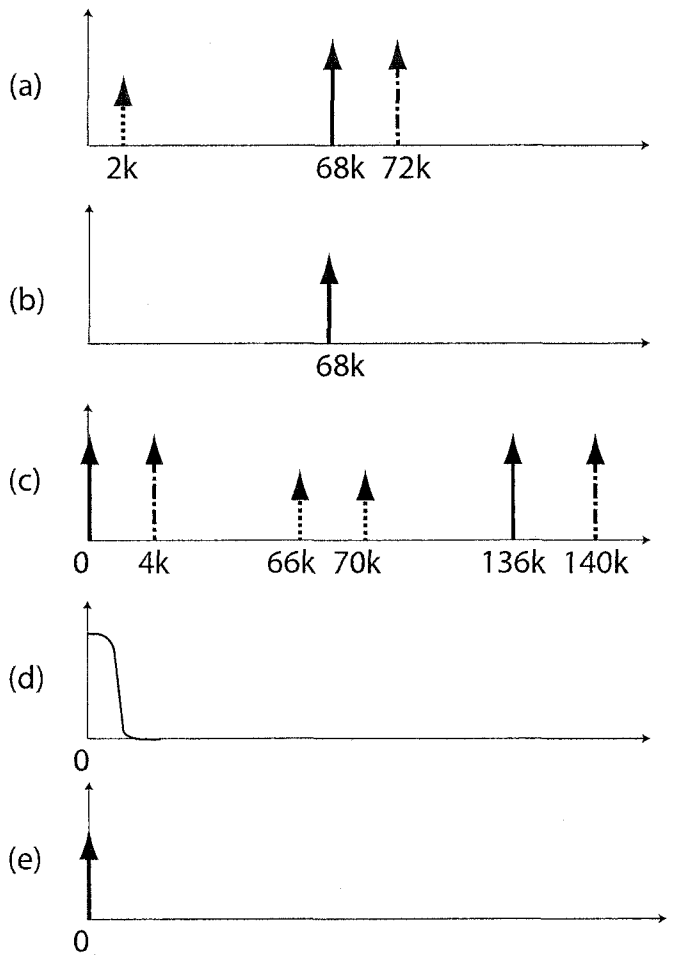

Figure 3.24 Illustration of modulation and demodulation of Hall signal in frequency domain. (a) Hall signal together with induction signal, (b) reference signal at 68 kHz, (c) output signal from the multiplier (AD633), where the reference signal is multiplied by the Hall signal, (d) low pass filter with -3dB frequency at 50 Hz, (e) output signal from the low pass filter. After demodulation, only DC signal remains which represents the level of the upper sideband of the modulated Hall signal while the induction signal is removed.

It should be pointed out that the reference signal (68kHz) and the modulated signal (72kHz and 2kHz) should have a fixed phase difference. Therefore, the coil excitation signal, the Hall sensor supply voltage and the demodulator reference signal should be synchronized.

3.6 Conclusion

A prototype linear Hall array probe was designed and built with eight Hall sensor ICs and a racetrack coil. Electrical circuits were designed to process multiple channel signals. The prototype probe was tested. The results show that the Hall sensor array probe can accelerate inspection time.

A multi-sensor linear array probe was designed based on high sensitivity, high resolution, custom designed Hall sensor arrays. It has a potential to reduce inspection time and to improve flaw detection ability. This is extremely useful when detecting small cracks near fasteners, where the back ground signals are large and high resolution is essential. The Hall array probe can be operated at low frequency. Thus it has the advantage of being able to detect deep cracks.

A test system has been built to process signals from multiple channels. The modulation technique is introduced to remove the induction voltage and to increase the signal to noise ratios.

3.7 Future work

After the high density linear Hall array probe is built and multi-channel test system is ready, a POD (probability of detection) study is needed to compare the characteristics of the new probe with other array probes. Other types of array probes can also be designed using the Hall sensors. The Hall sensors can be connected as a ring, which can cover the top of a bolt to enable fast inspection over many bolts in airplanes.

APPENDIX A. EDDY CURRENT MEASUREMENTS ON CASE HARDENED STEEL

A paper published in Review of Quantitative Nondestructive Testing, Vol. 21, 2002

Haiyan Sun John R. Bowler Nicola Bowler Marcus J. Johnson

Iowa State University, Center for Nondestructive Evaluation,

1915 Scholl Road, Ames, IA 50011, USA

Abstract

The case-hardening process modifies the near-surface permeability and conductivity of steel, as can be observed through changes in eddy current probe signals measured over a range of frequency. In this work, experiments have been performed using normal absolute probe coils on flat steel specimens and coils encircling case-hardened steel rods. By fitting model results to the experimental data, estimates of electrical material properties are found. The approach also allows an assessment of the sensitivity of the measurements to the case depth.

Introduction

Steel components are often subjected to a process which hardens the surface and produces what is known as a case-hardened layer. This improves the component's resistance to wear. The required depth of the case-hardened layer varies depending on the purpose for which the steel is needed, and manufacturers require a nondestructive method of measuring

the thickness of the layer in order to ensure that specifications are met.

The case-hardening process produces a change in the electrical conductivity and magnetic permeability of the steel in the case-hardened region. Consequently, these properties have different values near the steel surface and in the substrate. In simple terms, if the conductivity and permeability profile of the metal can be determined then the depth of the case-hardened layer can be deduced.

Eddy-current impedance measurements are sensitive to the conductivity and permeability profile of a test-piece. In principle, the material properties can be determined by comparing experimental measurements of eddy-current coil impedance with predictions from an appropriate theoretical model and adjusting the model parameters until agreement is obtained. Here, a simple model is adopted in which it is assumed that the material consists of a substrate with a single, uniformly thick, surface layer. The conductivity and permeability values differ in the substrate and in the surface layer. In this paper we present results of work on flat plates and cylindrical rods.

Studies on Plate Specimens

Preliminary investigations were performed on flat specimens using surface probes. Well-characterized samples [1] and precision eddy-current probes were used. To further reduce experimental uncertainties, the probe was calibrated using some standard characterization procedures, described below.

Probe Calibration

Coil P1, Table 1, was designed and built for measurements on plate specimens. The inner radius and the length of the coil were obtained by measuring the dimensions of the coil former with digital calipers, prior to the coil being wound. The outer radius and liftoff are difficult to measure directly and require the following special treatment.

TABLE 1. Coil parameters of probes P1 and E1.

Parameter	P1	E1
Number of turns	1858	1611
Inner radius (mm)	4.04	6.55
Outer radius (mm)	11.43	9.176
Length (mm)	8.02	19.93
Liftoff (mm)	1.08	–

Outer Radius: If the outer radius of the coil is measured directly using calipers, a value that is larger than the required value is obtained. This is because the diameter of the wire is finite and the coil is not perfectly wound. An effective value of the outer radius of the coil was determined by measuring the coil impedance in air (free space) over a frequency range of 40 Hz to 3 kHz and fitting the experimental data to calculated data based on the theory of Dodd and Deeds [2]. The impedance measurements were made using an Agilent 4294A impedance analyzer. When making free-space impedance measurements, the resistance of the coil remains nominally constant with frequency and only the reactance need be considered. Using this approach, a value of 11.43 mm was obtained for the effective outer radius of the coil, whereas the average of several measurements made using calipers was 12.0 mm.

Liftoff: The coil liftoff (defined as the distance between the base of the coil and the bottom of the probe casing) was determined by measuring the coil impedance with the probe placed on a thick aluminum plate, over a frequency range of 40 Hz to 3 kHz. The aluminum was sufficiently thick to approximate a half-space. The best fit between the experimental data and calculated data based on the theory of Dodd and Deeds [2] was found for a liftoff value of 1.08 mm, comparing well with the nominal value 1 mm.

Experimental Measurements

In order to minimize nonlinear effects which may arise due to the magnetic properties of steel, it is important that the magnetic field produced by the sensor be sufficiently

TABLE 2. Best fit parameters for three case-hardened plate specimens with different nominal values of case depth.

nominal case depth (mm)	substrate		surface layer	
	μ_r	σ (MS/m)	μ_r	σ (MS/m)
0.58	48	3.6	18	2.5
1.08	36	2.9	15	1.44
2.08	36	3.1	15	1.44

weak. The impedance of the coil placed on soft steel was measured using an Agilent 4294A impedance analyzer. The oscillator drive level was altered over a range approximately equal to one order of magnitude. The resulting impedance readings, except those at the highest drive level, were found to be independent of drive level indicating an absence of significant nonlinear excitation effects.

After the coil was fully calibrated, impedance analyzer measurements were made on a thick, demagnetized soft steel plate, over the frequency range 40 Hz to 3 kHz. The material conductivity and permeability values were adjusted in the theoretical model to give the best agreement between experimental data and calculated impedance values. The best fit was obtained for conductivity value 1.6 MS/m and relative permeability value 36.

The coil was then placed on a demagnetized, case-hardened steel plate and impedance measurements were made. In this investigation, the sample is modelled as a substrate with a single surface layer that represents the case-hardened region. The conductivity and permeability values of the surface layer are permitted to differ from those of the substrate. This means that five parameters are used to represent the samples: the conductivity and permeability of the substrate and the surface layer, and the layer thickness d. The parameter values which give the best fit between theory and experiment are given in Table 2 for three case-hardened plate specimens with different nominal values of case depth.

Permeability values obtained for the substrate were somewhat smaller than expected. It was also observed that there is a fairly weak dependence of the fit on the layer thickness parameter. For this reason, the results presented in Table 2 are for layer thickness values

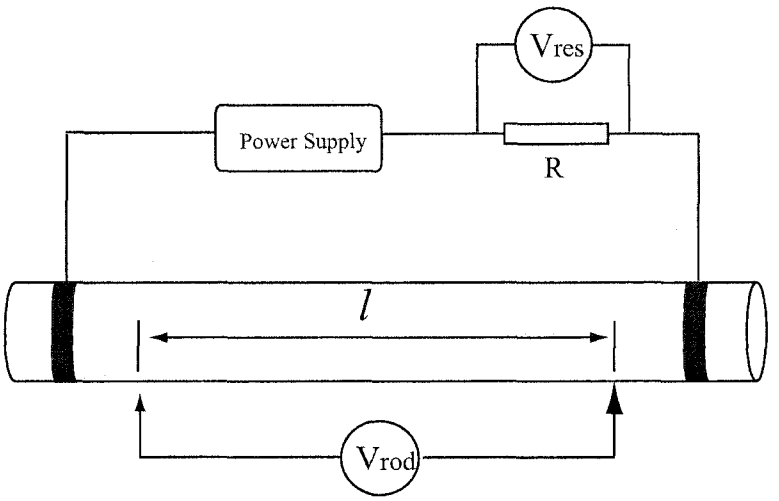

Figure A.1 Schematic diagram of the four-point conductivity measurement system.

equal to the nominal values provided by the manufacturer of the specimens [1].

Studies on Cylindrical Rods

Interpretation of the experimental data for the flat plate geometry is complicated due to the large number of free parameters in the model. With cylindrical specimens, the conductivity of the metal rods can be determined independently using a four-point voltage drop method. This reduces the number of parameters that must be adjusted to obtain a fit between theory and experiment.

Conductivity Measurements

A schematic diagram of the experimental arrangement for measuring the conductivity of the metal rods is shown in FIGURE 1.

TABLE 3. Conductivity of a soft steel rod measured using the four-point system and DC current.

		conductivity	
V_{rod} (mV)	V_{res} (mV)	(MS/m)	(% IACS)
10.78	586.8	3.927	6.771

Current is injected into the metal rod from either end. The voltage drop along the rod (V_{rod}) is measured between two points at which sharpened bolts are screwed in to the rod to make firm contact with its surface. Let L be the distance between the two points, R_{rod} be the resistance of the rod between them, and S be the cross-sectional area of the rod. A precision resistor ($R_{\text{res}} = 0.0471\Omega$) is connected in series with the rod. The voltage across the precision resistor (V_{res}) is measured in order to calculate the value of the current through the circuit, $I = V_{\text{res}}/R_{\text{res}}$. The conductivity of the metal is then determined using the equation

$$\sigma = \frac{L}{R_{\text{rod}}S} = \frac{V_{\text{res}}L}{V_{\text{rod}}R_{\text{res}}S}. \tag{A.1}$$

Both DC and AC measurements were made. In the DC measurement, two multimeters were used to measure the voltage across the rod (V_{rod}) and sensing resistor (V_{res}). In the AC measurement, a lock-in amplifier was used to measure the voltages. In order to ensure that the skin-effect was negligible, the frequency was kept between 0.05 and 1 Hz.

The accuracy of the experimental system was tested by measuring the conductivity of a copper rod with known conductivity 100.0% IACS. The measured conductivity of the copper rod was found to be 100.9% IACS with DC current and 101.1% IACS with AC current, indicating that the experimental system is accurate to within 1%.

The conductivity of a soft steel rod was then measured with both DC and AC current. The results are presented in Tables 3 and 4.

TABLE 4. Conductivity of a soft steel rod measured using the four-point system and AC current.

frequency (Hz)	V_{rod} (mV)	V_{res} (mV)	conductivity (MS/m)	conductivity (% IACS)
0.05	2.167	117.63	3.902	6.727
0.1	2.168	117.65	3.901	6.725
0.5	2.168	117.63	3.900	6.724

Impedance Measurements

An encircling coil, E1, was built to make impedance measurements on the cylindrical rod specimens. Coil E1 was wound around a cylindrical tube with the outer radius of the tube being the inner radius of the coil. The inner radius of the tube was designed to accommodate rod specimens such that they could easily be slipped into place. Parameters of coil E1 are listed in Table 1. The outer radius of coil E1 was calibrated using the same method as for coil P1.

First of all the impedance of coil E1 encircling a copper rod was measured to test the agreement between theory and experiment using the measured conductivity value as a parameter in the theoretical model. In FIGURE 2 it is shown that experimental results are consistent with theoretical predictions. Results are presented in the form

$$\Delta R = R - R_0 \qquad \text{and} \qquad \Delta X = X - X_0 \tag{A.2}$$

where the resistance R and reactance X are, respectively, the real and imaginary parts of the impedance. In the figure the measurements are normalized with respect to the free-space reactance X_0, where free-space measurements are denoted by the subscript '0'.

Measurements were then made on a demagnetized soft steel rod whose conductivity (3.9 MS/m) was measured using the four-point approach (Tables 3 and 4). The value of permeability was adjusted in the model until a good fit was obtained between theoretical data and experimental measurements. The best fit value for the relative permeability was 70 and the comparison between experimental and theoretical data is shown in FIGURE 3.

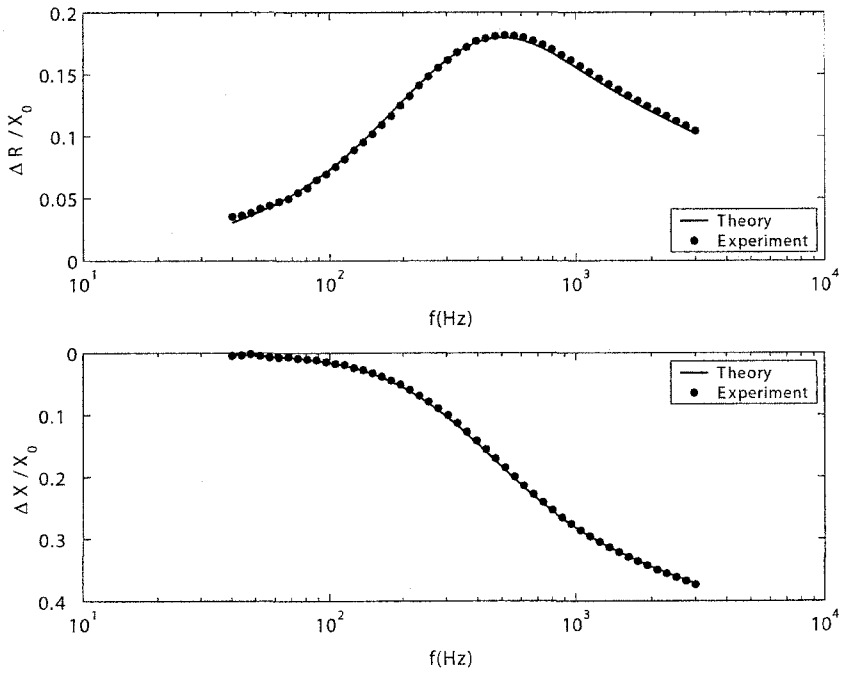

Figure A.2 Comparison between theory and experiment for eddy-current impedance measurements on a copper rod with conductivity $\sigma = 58.6$ MS/m.

Over all, the agreement between theory and experiment is very good. The reason for the small discrepancy between measured and calculated values of ΔR at low frequencies (below about 200 Hz) is unknown.

Impedance measurements were then made on demagnetized, case-hardened steel rods. Assuming that the substrate has the same conductivity and permeability as the soft steel rod ($\sigma = 3.9$ MS/m and $\mu_r = 70$), the surface-layer depth d, surface conductivity and permeability were adjusted to obtain the fit to experimental data shown in FIGURE 4.

The best values were $\sigma = 3.18$ MS/m, $\mu_r = 50$ and $d = 1.5$ mm. These values of σ and μ_r are reasonable given that the case-hardening process acts to reduce both conductivity and permeability. The value of d agrees with the nominal value for the specimen, indicating that this model-based approach may be used successfully to determine case depth.

In FIGURE 5, the root mean square error between the experimental data and the calculated impedance values is plotted as a function of layer depth for fixed conductivity and permeability values in the substrate and the surface layer. It can be seen that the error in both the resistive and reactive parts of the impedance goes through a minimum for $d = 1.5$ mm. For these calculations the conductivity and permeability in the substrate are 3.90 MS/m and 70, respectively. In the surface layer they are 3.18 MS/m and 50.

The very good fit between theory and experiment shown in FIGURE 4 is obtained by assuming that the conductivity and permeability of the substrate are the same as those for soft steel, obtained by experiment on a soft steel rod. This approximation allows two of the five parameters in the theoretical model to be constrained so that only the remaining three must be adjusted to obtain a good fit between theory and experiment. The method is apparently successful since the value obtained for the surface layer depth d agrees with the nominal value for the specimen.

If it is not possible to constrain the parameter values of the substrate in this way, an equally good fit between theory and experiment can be obtained for a different set of

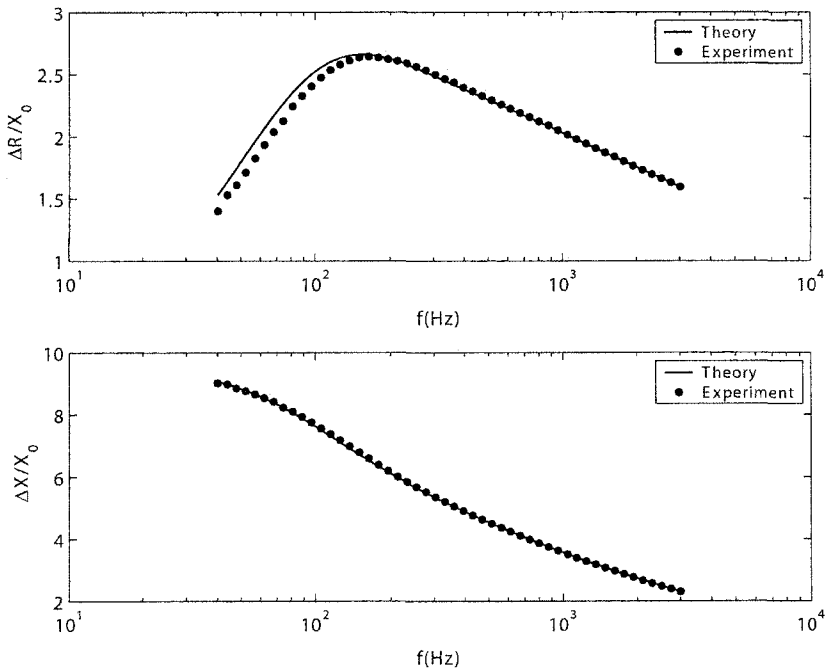

Figure A.3 Comparison between theory and experiment for eddy-current impedance measurements on a soft steel rod with conductivity $\sigma = 3.9$ MS/m and relative permeability 70.

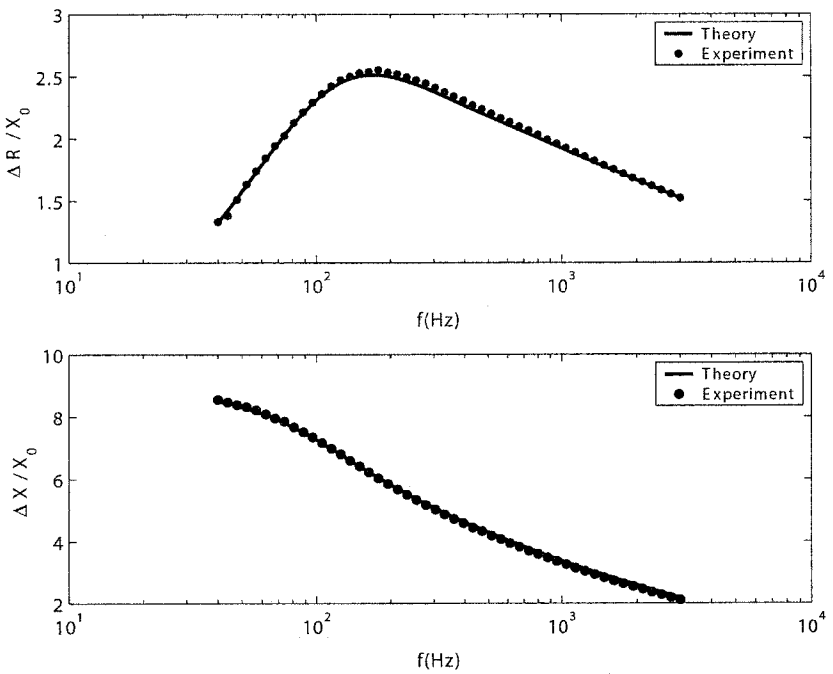

Figure A.4 Comparison between theory and experiment for eddy-current impedance measurements on a case-hardened steel rod. The theoretical curves shown here are obtained by fixing the conductivity and permeability values of the substrate to be the same as those found for the soft steel rod (FIGURE 3). The thickness, permeability and conductivity of the layer are then adjusted to obtain the best fit to the experimental data, as shown.

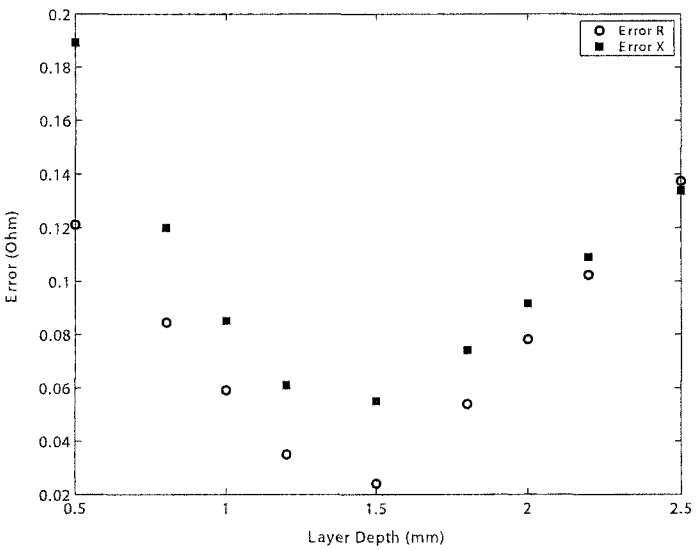

Figure A.5 Root mean square error between experimental and calculated values of coil resistance and reactance as a function of layer depth, for fixed conductivity and permeability values in the steel substrate and case-hardened layer.

parameter values. For example, if the relative permeability of the substrate is 58, then the best fit values for the surface layer are $\sigma = 4.4$ MS/m, $\mu_r = 65$ and $d = 1.5$ mm. In other words, the set of five model parameters which fits a given set of experimental data points is not unique. This demonstrates the need for independent determination of as many of the model parameters as possible before the fitting process begins.

Conclusion

The depth of a case-hardened layer in a steel rod has been determined by adjusting relevant parameters in a theoretical model and comparing calculated impedance values with experimental data obtained from a coil encircling the rod. The theoretical approach adopted here requires precise control of all relevant parameters in order to be successful. The probe must be well-characterized and the number of unknown sample parameters must be reduced to a minimum. By choosing specimens with cylindrical geometry, it is possible to measure the material conductivity directly. This reduces the number of unknowns sufficiently to allow model-based parameter fitting to work successfully.

These results indicate that the simple, two-layer model adopted here is sufficient to describe the structure of case-hardened steel. In future work, however, a more complicated model may be considered. For example, the material properties could be allowed to vary continuously with depth [3] .

Acknowledgement

This work was supported by the NSF Industry/University Cooperative Research Program.

Bibliography

[1] A.Ahmad, Eaton Co., Southfield, MI, private communication.

[2] Dodd, C. V. and Deeds, W. E., Journal of Applied Physics, *39*, 2829-2838, 1968.

[3] heodulidis, T. P., Tsiboukis, T. D. and Kriezis, E. E., IEEE Transactions on Magnetics, *39* (3), 1995.

APPENDIX B. ALTERNATING CURRENT POTENTIAL DROP ON A CONDUCTING ROD AND ITS USE FOR EVALUATION OF CASE HARDENED STEEL RODS

Haiyan Sun Yongqiang Huang John R. Bowler

Iowa State University, Center for Nondestructive Evaluation,

1915 Scholl Road, Ames, IA 50011, USA

Abstract

The case-hardening process modifies the near-surface permeability and conductivity of steel, as can be observed through changes in alternating current potential drop along a steel rod. In this work, a two-layer model is used approximating the case hardened rod as a homogeneous substrate with a single, uniformly thick, homogeneous surface layer, in which the conductivity and permeability values differ from those in the substrate. Analytical expressions showing the relationship between the alternating current potential drop along a homogeneous rod or a case hardened steel rod and its electrical and magnetic properties are provided. Potential drop measurements are performed on both homogeneous and case hardened steel rods over multi-frequency. By fitting model results to the experimental data, estimates of case depth and electromagnetic material properties are found. Case depth found by ACPD measurements are in reasonable agreement with the values obtained from hardness profile.

Introduction

Case hardening of steel components improves the resistance to wear by changing the carbon content and micro-structure of the surface region. In order to examine the results of case hardening and quantify the effect on components nondestructively, a number of methods have been developed [2–6]. These methods usually require an extensive calibration procedure using samples of known properties. Here an alternative approach, alternating current potential drop (ACPD) method, is presented in which the near surface material properties and the depth of penetration of the surface treatment is assessed using a model based approach. ACPD method and similarly, alternating current field measurement(ACFM), have already gained wide acceptance in crack measurements [7–12].

The case-hardening process produces a change in the electrical conductivity and magnetic permeability of the steel in the near surface region. Consequently, the electrical conductivity and magnetic permeability have different values near the surface compared with the substrate values. In this paper, the following assumptions are used. First, it is assumed that the conductivity and permeability variation with depth is indicative of the hardness profile allowing the case depth to be estimated from electromagnetic measurements. Second, cylindrical rod specimens are modelled as uniform in the axial direction having a homogeneous substrate surrounded by a homogeneous surface layer of uniform thickness. The transition zone between the two layers is neglected since it is very sharp (see Figure B.4). Third, it is assumed the process of case hardening does not modify the material properties below the case hardened layer. In other words, the conductivity and permeability of the substrate layer of a case hardened steel rod is the same as that of a non-hardened steel rod. Under these idealizations, the material properties can be evaluated by comparing alternating current potential drop (ACPD) measurements with theoretical prediction by adjusting the model parameters until their least-mean-square(LMS) errors are minimized. There are five unknown parameters in this model: the substrate conductivity σ_1 and relative permeability μ_{r1}, the surface conductivity σ_2 and relative permeability μ_{r2}

and the surface layer depth (case depth) d. They are determined separately in two steps. The substrate layer conductivity and permeability are found from non-hardened steel rod measurements. The surface layer conductivity, permeability and its layer depth are then estimated from case hardened steel rod measurements.

In this paper, analytical expressions for alternating current potential drop along a homogenous cylindrical rod and case hardened rod are derived. Then experimental results are given and material parameters are estimated based on the ACPD models and multi-frequency measurements.

Alternating current potential drop (ACPD) theory on conducting cylindrical rods

ACPD on a homogenous cylindrical rod

Suppose an alternating current is applied along an infinitely long cylindrical rod with a radius a. The current varies sinusoidally with time as the real part of $e^{\jmath\omega t}$.

The electromagnetic field inside the rod is governed by Maxwell's equations, which in the quasi-static limit,i.e., in the limit of negligible displacement current, can be written as:

$$\nabla \times \mathbf{H} = \mathbf{J} \tag{B.1}$$

$$\nabla \times \mathbf{E} = -\frac{\partial \mathbf{B}}{\partial t} \tag{B.2}$$

In addition Ohm's Law can be written as

$$\mathbf{J} = \sigma \mathbf{E} \tag{B.3}$$

It is assumed that there exist linear isotropic constitutive relations $\mathbf{D} = \epsilon \mathbf{E}$, $\mathbf{B} = \mu \mathbf{H}$. In these equations, ϵ,μ and σ are the permittivity, magnetic permeability and electrical conductivity of the metal rod. Equations (B.1),(B.2) and (B.3) can be used to give the following equation for $\mathbf{E}$

$$\nabla \times \nabla \times \mathbf{E} = -\mu\sigma \frac{\partial \mathbf{E}}{\partial t} \tag{B.4}$$

Note $\nabla \times \nabla \times \mathbf{E} = \nabla(\nabla \cdot \mathbf{E} - \nabla^2\mathbf{E})$. Since there's no free charges in the rod, $\nabla \cdot \mathbf{E} = 0$. Using the fact that $\mathbf{E}$ varies with time t as $e^{\jmath\omega t}$, (B.4) can be written as

$$\nabla^2\mathbf{E} = \jmath\omega\mu\sigma\mathbf{E} = -k^2\mathbf{E} \tag{B.5}$$

where $k^2 = -\jmath\omega\mu\sigma$, $k = (1-\jmath)/\delta$ and δ is the electromagnetic skin depth defined as $\delta = \sqrt{2/\omega\mu\sigma}$. Due to symmetry of the rod, $\mathbf{E}$ is a function of radial coordinate ρ only. Putting $\mathbf{E} = \hat{z}E(\rho, k)$, equation (B.5) gives

$$\frac{\partial^2 E}{\partial \rho^2} + \frac{1}{\rho}\frac{\partial E}{\partial \rho} + k^2 E = 0, \tag{B.6}$$

This is a modified form of the equation for the zeroth order Bessel function. On applying the boundary condition on the rod surface that $E = E_0$ where $\rho = a$, equation(B.6) has the following solution as:

$$E(\rho, k) = E_0 J_0(k\rho)/J_0(ka). \tag{B.7}$$

The total current passing through the rod can be expressed as

$$I = 2\pi\sigma \int_0^a E(\rho, k)\rho \, d\rho. \tag{B.8}$$

Using equation (B.7) and the following integration [1],

$$\int_0^a J_0(k\rho)\rho \, d\rho = \frac{a}{k} J_1(ka). \tag{B.9}$$

Equation (B.8) gives

$$I = \frac{2\pi\sigma \, aE_0}{kJ_0(ka)} J_1(ka). \tag{B.10}$$

Hence the surface electric field is related to the total current by

$$E_0(k) = \frac{kIJ_0(ka)}{2\pi\sigma \, aJ_1(ka)}. \tag{B.11}$$

Letting l be the length measured along the rod between the two contact points of the voltage electrodes(see Figure B.1), the potential drop between these two points is given by

$$V(k) = E_0(k)l = \frac{klIJ_0(ka)}{2\pi\sigma \, aJ_1(ka)}. \tag{B.12}$$

The measured voltage includes a contribution from the electromotive force(emf) induced in the voltage measurement circuit due to changing of magnetic flux linking this circuit. Express the induced emf in terms of the self inductance L, the total voltage, V_T, sensed across a length l of the rod is

$$V_T = \frac{klIJ_0(ka)}{2\pi\sigma\, aJ_1(ka)} + j\omega LI. \tag{B.13}$$

The rod impedance is defined as

$$Z_{\text{rod}} = \frac{klJ_0(ka)}{2\pi\sigma\, aJ_1(ka)} + j\omega L. \tag{B.14}$$

Equation (B.14) can be used to estimate material properties of a homogeneous rod from multi-frequency potential drop measurements.

ACPD on a case hardened steel rod

A case hardened steel rod with radius of b has a conductivity of σ_1 and permeability of μ_1 in its inner core where $\rho \leq a$. In its outer layer where $a \leq \rho \leq b$, the conductivity and permeability are σ_2 and μ_2 respectively. Using a cylindrical polar coordinate system, put the axis of the rod in z direction, the coordinates of ρ and ϕ can be defined consequently.

When applying an alternating current down the axis of the case hardened steel rod (z direction), the electric field intensity in the rod should be governed by equations similar to (B.5), with different conductivity and permeability for the two regions:

$$\nabla^2\mathbf{E_1} = -k_1^2\mathbf{E_1} \qquad (0 \leq \rho \leq a) \tag{B.15}$$

$$\nabla^2\mathbf{E_2} = -k_2^2\mathbf{E_2} \qquad (a \leq \rho \leq b), \tag{B.16}$$

where k_1,k_2 satisfy $k_i^2 = -j\omega\mu_i\sigma_i$ for $i = 1, 2$. Note that the direction of $\mathbf{E_1}$ and $\mathbf{E_2}$ are both in the z direction. The solution to equation (B.15) can be borrowed from equation (B.7),

$$E_1(\rho, k) = E_0AJ_0(k_1\rho). \tag{B.17}$$

Because Bessel function $Y_0(k_2\rho)$ goes to infinity while ρ goes to zero, it's not included in the solution (B.17). But it should be added to give the solution to the equation (B.16) in the surface layer:

$$E_2(\rho, k) = E_0[BJ_0(k_2\rho) + CY_0(k_2\rho)]. \tag{B.18}$$

Note that A, B, C above are scaling factors to be determined by the following boundary conditions.

First, assuming the electric field intensity on the rod surface is E_0, i.e. $E_2 = E_0$ when $\rho = b$, gives

$$BJ_0(k_2b) + CY_0(k_2b) = 1. \tag{B.19}$$

Next, the tangential part of electric fields are continuous on $\rho = a$, so,

$$BJ_0(k_2a) + CY_0(k_2a) = AJ_0(k_1a). \tag{B.20}$$

Third, from

$$\nabla \times \mathbf{E} = -\frac{\partial E}{\partial \rho}\hat{\phi} \tag{B.21}$$

and

$$\nabla \times \mathbf{E} = -\jmath\omega\mu H_\phi\hat{\phi} \tag{B.22}$$

and the fact that the tangential part of magnetic field intensity is continuous at $\rho = a$, one can get

$$\frac{1}{\mu_1}\frac{\partial E_1}{\partial \rho} = \frac{1}{\mu_2}\frac{\partial E_2}{\partial \rho}. \tag{B.23}$$

From (B.17) and (B.18),

$$\frac{\partial E_1}{\partial \rho} = -E_0Ak_1J_1(k_1\rho) \tag{B.24}$$

and

$$\frac{\partial E_2}{\partial \rho} = -E_0k_2[BJ_1(k_2\rho) + CY_1(k_2\rho)], \tag{B.25}$$

thus the third condition is given by,

$$A\mu_2k_1J_1(k_1a) = B\mu_1k_2J_1(k_2a) + C\mu_1k_2Y_1(k_2a) \tag{B.26}$$

The scaling factors A, B, C can now be obtained from equations (B.19), (B.20),and (B.26) where

$$A = \Delta_A/\Delta, \qquad B = \Delta_B/\Delta, \qquad C = \Delta_C/\Delta. \tag{B.27}$$

$$\Delta_A = E_0\mu_1 k_2[J_1(k_2a)Y_0(k_2a) - Y_1(k_2a)J_0(k_2a)] \tag{B.28}$$

$$\Delta_B = -E_0\mu_1 k_2 Y_1(k_2a)J_0(k_1a) + E_0\mu_2 k_1 J_1(k_1a)Y_0(k_2a) \tag{B.29}$$

$$\Delta_C = -E_0\mu_2 k_1 J_1(k_1a)J_0(k_2a) + E_0\mu_1 k_2 J_0(k_1a)J_1(k_2a) \tag{B.30}$$

$$\begin{aligned}\Delta &= -\mu_1 k_2 J_0(k_1a)J_0(k_2b)Y_1(k_2a) - \mu_2 k_1 J_1(k_1a)J_0(k_2a)Y_0(k_2b) \\ &\quad +\mu_2 k_1 J_1(k_1a)J_0(k_2b)Y_0(k_2a) + \mu_1 k_2 J_1(k_2a)Y_0(k_2b)J_0(k_1a) \qquad \text{(B.31)} \\ &= J_0(K_2b)\Delta_B + Y_0(k_2b)\Delta_C \qquad \text{(B.32)}\end{aligned}$$

Once the scaling factors A, B, and C are known, the electric field density inside the rod is also known from equations (B.17) and (B.18). Then the potential drop can be derived as follows. The current along the rod can be written as:

$$I = 2\pi\sigma_1 \int_0^a E_1(\rho)\rho\, d\rho + 2\pi\sigma_2 \int_a^b E_2(\rho)\rho\, d\rho \tag{B.33}$$

By applying equations (B.17) and (B.18), (B.33) becomes

$$\frac{I}{E_0} = 2\pi\sigma_1 A \int_0^a J_0(k_1\rho)\rho\, d\rho + 2\pi\sigma_2 B \int_a^b J_0(k_2\rho)\rho\, d\rho + 2\pi\sigma_2 C \int_a^b Y_0(k_2\rho)\rho\, d\rho \tag{B.34}$$

Use the result of the following integration [1],

$$\int_0^a xY_0(x)dx = aY_1(a) + \frac{2}{\pi} \tag{B.35}$$

one can easily get

$$\int_0^a Y_0(k\rho)\rho\, d\rho = \frac{aY_1(ka)}{k} + \frac{2}{k^2\pi}. \tag{B.36}$$

After integration, equation (B.34) becomes

$$\frac{I}{E_0} = 2\pi\sigma_1 AaJ_1(k_1a)/k_1 + 2\pi\sigma_2 B[bJ_1(k_2b) - aJ_1(k_2a)]/k_2 + 2\pi\sigma_2 C[bY_1(k_2b) - aY_1(k_2a)]/k_2. \tag{B.37}$$

Rearrange the above equation to give the electric field intensity on the surface of the rod:

$$E_0 = \frac{I}{2\pi\sigma_1 AaJ_1(k_1a)/k_1 + 2\pi\sigma_2 B[bJ_1(k_2b) - aJ_1(k_2a)]/k_2 + 2\pi\sigma_2 C[bY_1(k_2b) - aY_1(k_2a)]/k_2}. \tag{B.38}$$

Thus the potential drop including emf is

$$V_T = E_0 l + j\omega LI \tag{B.39}$$

where l is the length measured along the rod between the two contact points, and L is the self inductance of the measurement circuit. The rod impedance is defined as

$$Z_{\text{rod}} = \frac{E_0 l}{I} + j\omega L \tag{B.40}$$

.

Experimental arrangement and results

ACPD measurement system

A Kepco bipolar operational power supply/amplifier, driven by the internal function generator of a SR830 DSP lock-in amplifier, is used to inject constant AC sinusoidal current into the cylindrical rod. The current is injected into the rod through copper loops which are kept tight contact with the rod surface. A high precision resistor is connected in serial with the rest of the circuit to detect the current by measuring the voltage (V_{res}) across it using the lock-in amplifier. To measure the potential drop along the cylindrical rod (V_{rod}), two GSS-8-7-G probes from Interconnect Devices Inc. are kept point contact with the rod surface. The distance between the two probes is l. The two probes are connected to the lock-in amplifier by very thin copper wire (0.13mm in diameter). To minimize the self inductance in the voltage measurement circuit, the two copper wires are twisted together and are kept as close to the rod surface as possible. Since both V_{res} and V_{rod} are measured by one lock-in amplifier, an electrical switch is added to switch between the two signals. ACPD measurements are taken in the frequency range of 1 Hz to 10 KHz. A control

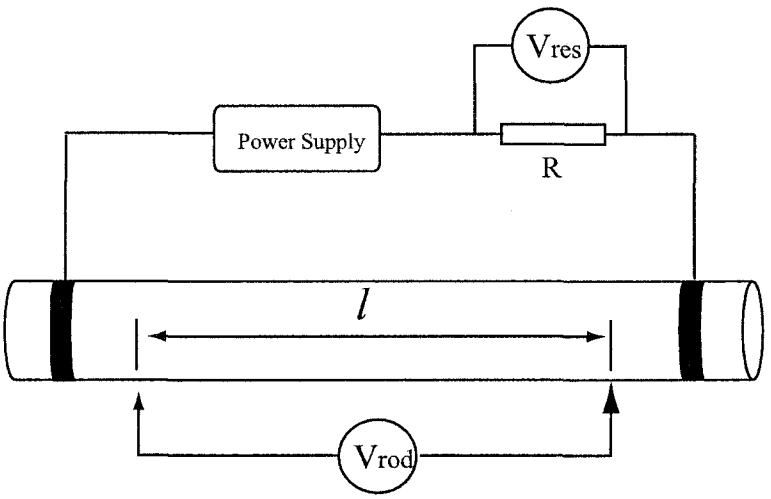

Figure B.1 Schematic diagram of the four-point ACPD measurement system.

program is developed to control the lock-in amplifier and the electrical switch and acquire multi-frequency data automatically. Six cylindrical rod specimens are measured by the ACPD system: 1 copper rod, 1 non-hardened steel rod and 4 case hardened steel rods. Their dimensions are shown in Table B.1.

Cylindrical copper rod

The accuracy of the ACPD system is test by taking multi-frequency measurements on a pure copper rod with a known conductivity of 58MS/m or 100% IACS. Since the relative permeability of copper is 1, experimental data and equation (B.13) are used to fit the conductivity σ of the rod and self inductance L in the circuit. Results are shown in Figure B.2. The fit values are $\sigma = 58.4$MS/m or 100.70% IACS and L = 3.20nH. It is clear that the system is accurate within 2% and the self inductance in the measurement is very small.

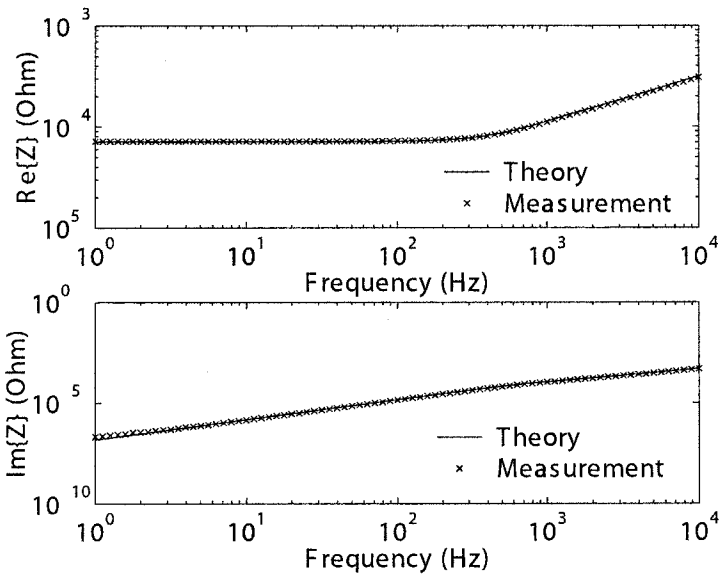

Figure B.2 Comparison between theory and the ACPD measurements on a copper rod with conductivity of 58.4MS/m.

Homogenous non-hardened cylindrical steel rod

The non-hardened cylindrical steel rod is assumed to be homogenous. Its conductivity and relative permeability are estimated by fitting the experimental data with theoretical model using equation (B.14). Self inductance L can vary in each measurement. Since it appears as a pure imaginary part in equation (B.14), to reduce error, only real part of the data are used to fit σ and μ_r. To give data in different frequencies the equal weight, the measured rod impedance is normalized by the theoretical rod impedance from the fitted parameters. Results are shown in Figure B.3. Fitted values are $\sigma = 4.84\text{MS/m}, \mu_\text{r} = 64.2$.

Case hardened cylindrical steel rod

Four 1045 carbon steel rods from McMaster-Carr are heat treated by inductance hardening. They have a nominal case depth of 0.5mm, 1.0mm, 1.5mm, and 2.0mm respectively. Their hardness profile, shown in Figure B.4, is obtained through hardness measurements. The effective case depth is determined from the hardness profile. Consider the hardness range of the whole steel rod, one hardness number is selected to calculate the effective case depth. For the 1045 carbon steel that is used in this experiment, effective case depths are defined from surface to the 50 HRC point (shown in Figure B.4). Since this definition is different from the case depth defined in the ACPD model, it is acceptable that the ACPD measurement will give a different values for the case depth.

For the case hardened steel rods, it is assumed that substrate conductivity σ_1 and relative permeability μ_{r1} of the case hardened rod are the same as the non-hardened homogenous steel rod. Thus $\sigma_1 = 4.84\text{MS/m}$ and $\mu_{r1} = 64.2$. ACPD measurements are taken on the case hardened steel rods to estimate the electrical conductivity σ_2, permeability μ_2 and case depth d of the outer layer by fitting experimental data to ACPD model using equation (B.14) and (B.40). Measured impedance data are normalized as $Z_n = Z/Z_0$ where Z is the measured data, and Z_0 is the theoretical rod impedance calculated using the σ and μ of the non-hardened steel rod and dimension of the case hardened steel rods. Again, only real

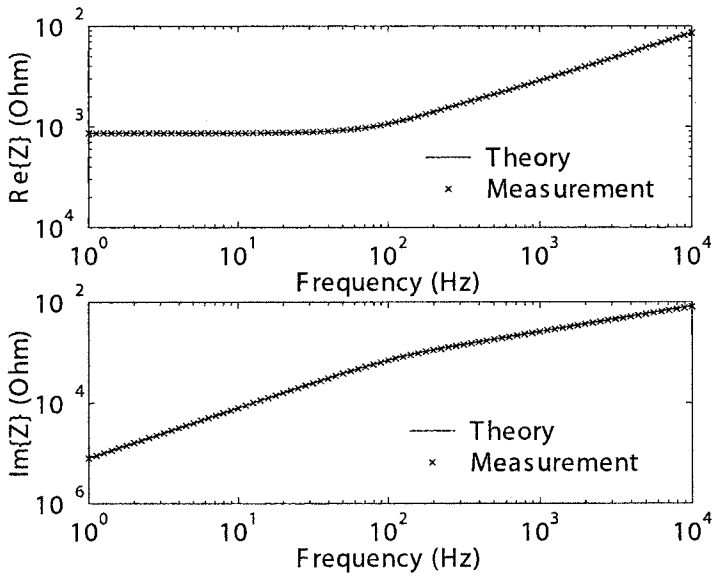

Figure B.3 Comparison between theory and the ACPD measurements on a homogeneous steel rod with $\sigma = 4.84$MS/m and $\mu_r = 70$ determined by data fitting of theoretical model predictions to multi-frequency ACPD measurements.

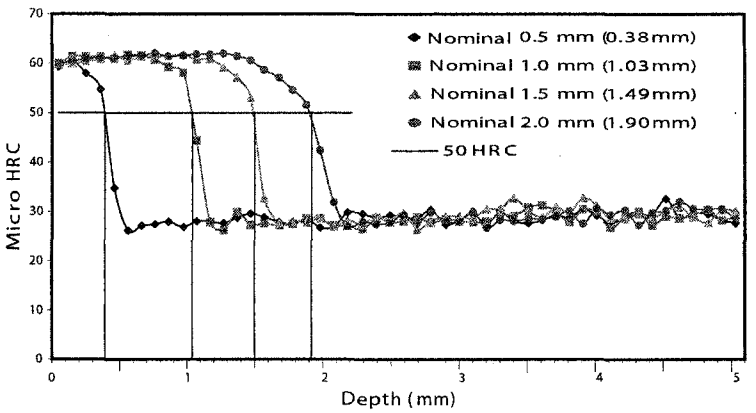

Figure B.4 Hardness profile of the four case hardened steel rods.

part of the data are used for fitting. Fitted values are shown in Table B.2. Figures are in Figure B.5 and Figure B.6. The effective case depths d_e obtained from hardness profile are also shown. Reasonable agreement is observed between the case depth evaluated from ACPD measurements and the effective case depth from hardness profile.

Table B.1 Measured dimensions of six cylindrical rods. The last four rows are for case hardened steel rods with nominal case depth of 0.5mm, 1.0mm, 1.5mm and 2.0mm respectively.

Rod Specimens	Length (cm)	Diameter (mm)
Copper rod	50.9	11.06
untreated rod	50.3	11.02
nominal case depth 0.5mm rod	50.2	11.00
nominal case depth 1.0mm rod	50.3	11.02
nominal case depth 1.5mm rod	50.2	11.02
nominal case depth 2.0mm rod	50.1	11.02

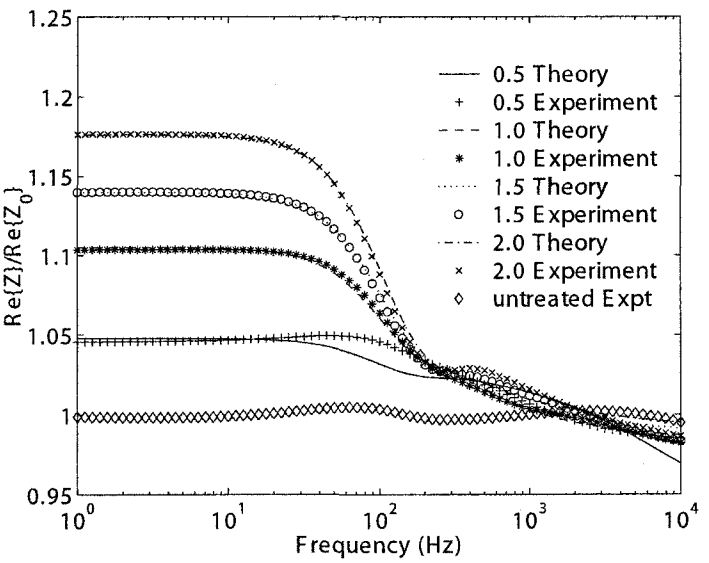

Figure B.5 Real part of experimental data and theoretical fit curve for case hardened steel rods. Numbers in the legend are the nominal case depth in mm.

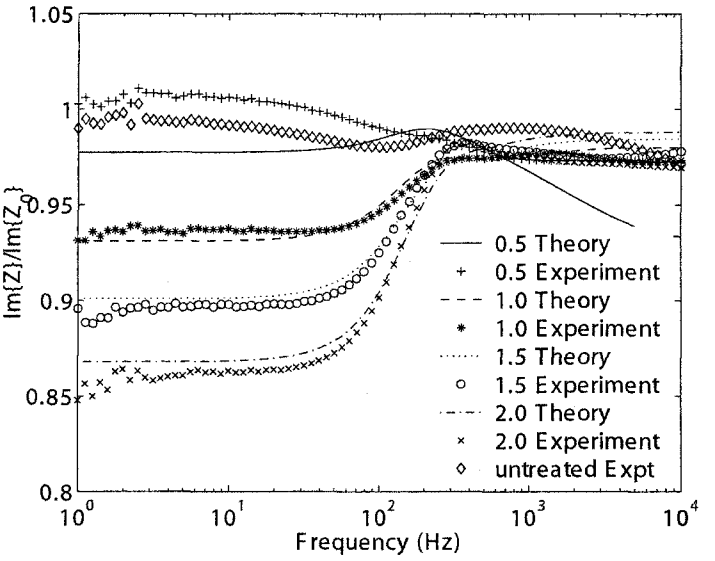

Figure B.6 Imaginary part of experimental data and theoretical curve fit by using real part of experimental data for case hardened steel rods. Numbers in the legend are the nominal case depth in mm.

Table B.2 Surface layer parameters found by data fitting between ACPD measurements and theoretical models. Their substrate parameters are fixed at $\sigma_1 = 4.84\text{MS/m}, \mu_{r1} = 64.2$. Effective case depth d_e is obtained from the hardness profile

Rod Specimens	μ_2	σ_2(Ms/m)	d(mm)	d_e(mm)
nominal case depth 0.5mm rod	37.1	3.14	0.37	0.38
nominal case depth 1.0mm rod	50.0	3.92	1.62	1.03
nominal case depth 1.5mm rod	50.6	3.93	2.27	1.49
nominal case depth 2.0mm rod	50.7	3.90	2.92	1.90

Conclusion

The ACPD theory for cylindrical rod is developed for both homogenous and layered rod. By fitting experimental data with the theoretical model, material electromagnetic properties can be found. ACPD measurement system is set up and its accuracy is verified to be accurate within 2%. ACPD measurements are taken on a copper rod, a homogeneous non-hardened steel rod and four case hardened rods. Conductivity, permeability, and case depth are evaluated by fitting multi-frequency ACPD measurements with the theoretical model. The estimated case depth using this method is in reasonable agreement with the effective case depth obtained from hardness profile.

Bibliography

[1] Abramowitz, M., A. Stegun, I. A., *Handbook of Mathematical Functions With Formulas, Graphs, and Mathematical Tables* (1970)

[2] Mihaa, T., Obata, M., Carburized case depth estimation by Rayleigh-wave backscattering, *Materials Evaluation, 49*(6), 696–700, 1991

[3] Addison, R. C., Safaeinili, A., McKie, A. D. W., Ultrasonic determination of case depth and surface hardness in axles,*Nondestructive Characterization of Materials VIII*, Plenum publishing corp., 211–216, 1998

[4] Good, M., Schuster, G., Skorpik, J., Ultrasonic material hardness depth measurement, United States patent 5646351, 1997

[5] Dubois, M., Fiset, M., Evaluation of case depth on steels by Barkhausen noise measurement, *Materials Science and Technology,11*(3), 264–267, 1995

[6] Vaidyanathan, S., Moorthy, V., Jayakumar, T., Raj, B., Evaluation of induction hardened case depth through microstructural characterization using magnetic Barkhausen emission technique, *Materials Science and Technology,16*(2),202–208,2000

[7] Dover, W. D., Charlesworth, F. D., Tayler, K. A., Collins, R., and Michael, D. H.,The use of AC Field Measurements to Determine the Shape and Size of a Crack in a Metal, *ASTM Special Technical Publication 722*, American Society for Testing and Materials, 401–427, 1981

[8] Venkatasubramanian, T. V., Unvala, B. A., AC potential drop system for monitoring crack length, *Journal of physics E: scientific instruments*, *17*(9), 765–771, 1984

[9] Taylor, H., Kilpatrick, I. M., Jolley, G., Developments in AC potential drop crack sizing, *British Journal of nondestructive testing*, *27*(2), 88–90, 1985

[10] Frise, P. R., Bell, R., Improved probe array for ACPD crack measurements, *British journal of nondestructive testing*, *34*(1), 15–19, 1992

[11] Dai, Y., Marchand, N. J., Hongoh, M., Fatigue crack growth measurements in TMF testing of titanium alloys using an ACPD technique, *ASTM Special Technical Publication 1251*, American Society for Testing and materials, 17–32, 1995

[12] Tiku, S., Marchand, N. J., Unvala, B., An advanced multiple frequency ACPD system for crack detection and calibration, *ASTM Special Technical Publication 1318*, American Society for Testing and materials, 56–70, 1997

BIBLIOGRAPHY

[1] Stanley R. K., Moore P. O. and McIntire P. M., Nondestructive testing handbook, Special nondestructive testing methods, second edition, V. 9, American Society for Nondestructive Testing: 378-397, 1995.

[2] Tada N., Monitoring of a surface crack in a finite body by means of electrical potential technique, *International Journal of Fracture*, 57 (3): 199-220, 1992.

[3] Oppermann W. and Keller H. P., An improved potential drop method for measuring and monitoring defects in metallic structures, *Nuclear Engineering and Design*, 144: 171-175, 1993.

[4] Riemelmoser F. O., Pippan R., Weinhandl H. and Kolednik O., The influence of irregularities in the crack shape on the crack extension measurement by means of the direct-current-potential-drop method, *Journal of Testing and Evaluation*, 27 (1): 42-46, 1999.

[5] Chen W. H., Chen J. S. and Fang H. L., A theoretical procedure for detection of simulated cracks in a pipe by the direct current potential drop technique, *Nuclear Engineering and Design*, 216 (1-3): 203-211, 2002.

[6] Cerny I., The use of DCPD method for measurement of growth of cracks in large components at normal and elevated temperatures, *Engineering Fracture Machanics*, 71 (4-6): 837-848, 2004.

[7] Yee R. and Lambert S. B., A reversing direct-current potential drop system for detecting and sizing fatigue cracks along weld toes, *Journal of Testing and Evaluation*, 23 (4): 254-260, 1995.

[8] Saka M., Oouchi A. and Abe H., NDE of a crack by using closely coupled probes for DCPD technique, *Journal of Pressure Vessel Technology - Transactions of the ASME*, 118 (2): 198-202, 1996.

[9] Saka M., Hirota D., Abe H. and Komura I., NDE of a 3-D surface crack using closely coupled probes for DCPD technique, *Journal of Pressure Vessel Technology - Transactions of the ASME*, 120 (4): 374-378, 1998.

[10] Akama M. and Saka M., Nondestructive sizing of a 3D surface crack generated in a railway component using closely coupled probes for direct-current potential drop technique, *Engineering Fracture Machanics*, 72 (4): 319-334, 2005.

[11] Swartzendruber L. J., 4-point probe measurement of non-uniformities in semiconductor sheet resistivity, *Solid-State Electronics*, 7 (6): 413-422, 1964.

[12] Perloff D. F., 4-point sheet resistance correction factors for thin rectangular samples, *Solid-State Electronics*, 20 (8): 681-687, 1977.

[13] Yamashita M. and Agu M., Geometrical correction factor for semiconductor resistivity measurements by 4-point probe method, *Japanese Journal of Applied Physics*, 23 (11): 1499-1504, 1984.

[14] Yamashita M., Resistivity correction factor for 4-probe method on circular semiconductors — I, *Japanese Journal of Applied Physics*, 26 (9): 1550-1554, 1987.

[15] Yamashita M., Resistivity correction factor for 4-probe method on circular semiconductors — II, *Japanese Journal of Applied Physics*, 27 (7): 1317-1321, 1988.

[16] Yamashita M., Toshifumi N. and Kurihara H., Resistivity correction factor for the four-point probe method on cylindrical materials, *Japanese Journal of Applied Physics*, 35: 1948-1953, 1996.

[17] Dover W. D., Charlesworth F. D. W., Taylor K. A., Collins R. and Michael D. H., The use of AC field measurements to determine the shape and size of a crack in metal, *Eddy-current Characterization of Materials and Structures, ASTM STP 722*, ASTM: 401-427, 1981.

[18] Frise P. R. and Bell R., Improved probe array for ACPD crack measurements, *British Journal of Nondestructive Testing*, 34 (1): 15-19, 1992.

[19] Collins R., Michael D. H. and Clark R., Measurement of crack depth in a transition weld using ACPD, *Review of Progress in Quantitative Nondestructive Evaluation*, 11 (A): 545-552, 1992.

[20] Venkatasubramanian, T. V. and Unvala B. A., AC potential drop system for monitoring crack length, *Journal of Physics E: Scientific Instruments*, 17 (9): 765-771, 1984.

[21] Taylor H., Kilpatrick I. M. and Jolley G., Developments in AC potential drop crack sizing, *British Journal of Nondestructive Testing*, 27 (2): 88-90, 1985.

[22] Dai Y., Marchand N. J., Hongoh M., Fatigue crack growth measurements in TMF testing of titanium alloys using an ACPD technique, *ASTM Special Technical Publication 1251*, American Society for Testing and Materials: 17-32, 1995.

[23] Tiku S., Marchand N. J. and Unvala B., An advanced multiple frequency ACPD system for crack detection and calibration, *ASTM Special Technical Publication 1318*, American Society for Testing and Materials: 56-70, 1997.

[24] Ditchburn D. J., Burke S. K. and Scala C. M., NDT of the welds: state of the art, *NDT and E International*, 29 (2): 111-117, 1996.

[25] Dover W. D. and Monahan C. C., The measurements of surface breaking cracks by the electrical systems ACPD/ACFM, *Fatigue and Fracture of Engineering Materials and Structures*, 17 (12): 1485-1492, 1994.

[26] Electromagnetic testing, *Nondestructive Testing Handbook*, V. 5, American Society for Nondestructive Testing: 248-268, 2004.

[27] Topp D. A. and Dover W. D., Review of ACPD/ACFM crack measurement system, *Review of Progress in Quantitative Nondestructive Evaluation*, 10 (A): 301-308, 1991.

[28] Lewis A. M., Michael D. H., Lugg M. C. and Collins R., Thin-skin electromagnetic-fields around surface-breaking cracks in metals, *Journal of Applied Physics*, 64 (8): 3777-3784, 1988.

[29] Fazouane A., Giordano P., Collins R. and Lugg M., ACFM above flaws near and edge in a ferromagnetic block: result, *Review of Progress in Quantitative Nondestructive Evaluation*, 13 (A): 1119-1126, 1994.

[30] LeTessier R., Coade R. W. and Beneve B., Sizing of cracks using the alternating current field measurement technique, *International Journal of Pressure Vessels and Piping*, 79 (8-10): 549-554, 2002.

[31] Laenen C. and Raine A., Additional applications with the alternating current field measurement (ACFM) technique, *Insight*, 40 (12): 860-863, 1998.

[32] Raine A., Cost benefit applications using the alternating current field measurement inspection technique, *Proceedings of 8th European Conference on Non-Destructive Testing*, Barcelona, Spain, June 2002.

[33] Huang Y., Alternating current potential drop and eddy current methods for nondestructive evaluation of case depth, *Doctor of Philosophy, Iowa State University*, Ames, Iowa, 2004.

[34] Johnson M. J., Chester L. O., Hentscher S. and Kinser E., Analysis of conductivity and permeability profiles in hardened steel, *10th International Workshop on Electromagnetic Nondestructive Evaluation*, Lansing, Michigan, 2004.

[35] Mihaa T. and Obata M., Carburized case depth estimation by Rayleigh-wave backscattering, *Materials Evaluation*, 49 (6): 696–700, 1991.

[36] Addison R. C., Safaeinili A. and McKie A. D. W., Ultrasonic determination of case depth and surface hardness in axles, *Nondestructive Characterization of Materials VIII*, Plenum Publishing Corporation: 211-216, 1998.

[37] Good, Morris S., Schuster and Gorge J., Ultrasonic material hardness depth measurement, *United States Patent* 5646351, 1997.

[38] Dubois M. and Fiset M., Evaluation of case depth on steels by Barkhausen noise measurement, *Materials Science and Technology*, 11 (3): 264-267, 1995.

[39] Vaidyanathan S., Moorthy V., Jayakumar T. and Raj B., Evaluation of induction hardened case depth through microstructural characterization using magnetic Barkhausen emission technique, *Materials Science and Technology*, 16 (2): 202-208, 2000.

[40] Mitrofanov V. A. and Gryazev S. G., Theoretical fundamentals of three-parameter testing of a hardened layer by an asymmetric electropotential quasi-DC probe: I. HL model, *Russian Journal of Nondestructive Testing*, 39 (11): 871-878, 2003.

[41] Mitrofanov V. A. and Gryazev S. G., Theoretical fundamentals of three-parameter testing of a hardened layer by an asymmetric electropotential quasi-DC probe: II. H and L models, *Russian Journal of Nondestructive Testing*, 39 (12): 948-957, 2003.

[42] Dodd C. V. and Deeds W. E., Analytical solutions to eddy-current probe-coil problems, *Journal of Applied Physics*, 39: 2829-2838, 1968.

[43] Dodd C. V., Cheng C. C. and Deeds W. E., Induction coils coaxial with an arbitrary number of cylindrical conductors, *Journal of Applied Physics*, 45: 638-647, 1974.

[44] Theodoulidis T. P., End effect modelling in eddy current tube testing, *International Journal of Applied Electromagnetics and Mechanics* 19 (1-4): 207-212, 2004.

[45] Bowler J. R. and Theodoulidis T. P., Eddy currents induced in a conducting rod of finite length by a coaxial encircling coil, To be submitted.

[46] Theodoulidis T. P., Model of ferrite-cored probes for eddy current nondestructive evaluation, *Journal of Applied Physics*, 93 (5): 3071-3078, 2003.

[47] Theodoulidis T. P. and Bowler J. R., Eddy current interaction of a long coil with a slot in a conductive plate, submitted to *IEEE Transaction of Magnetics*, 2004.

[48] Peng S. T. and Oliner A. A, Guidance and leakage properties of a class of open dielectric wave-guides, 1. Mathematical formulations, *IEEE Transactions on Microwave Theory and Techniques*, 29 (9): 843-855, 1981.

[49] Peng S.T. and Oliner A.A, Guidance and leakage properties of a class of open dielectric wave-guides, 2. new physical effects, *IEEE Transactions on Microwave Theory and Techniques*, 29 (9): 855-869, 1981.

[50] Alessandri F., Mongiardo M., and Sorrentino R., Rigorous mode matching analysis of mitered E-plane bends in rectangular wave-guide, *IEEE Microwave and Guided Wave Letters*, 4 (12): 408-410, 1994.

[51] Eleftheriades G. V., Omar A. S., Katehi L. P. B., Rebeiz and G. M., Some important properties of wave-guide junction generalized scattering matrices in the context of the mode matching technique, *IEEE Transactions on Microwave Theory and Techniques*, 42 (10): 1896-1903, 1994.

[52] Liang X. P., Zaki K. A. and Atia A. E., A rigorous 3 plane mode-matching technique for characterizing wave-guide T-junctions and its application in multiplexer design, *IEEE Transactions on Microwave Theory and Techniques*, 39 (12): 2138 - 2147, 1991.

[53] Huting W. A. and Webb K. J., Comparison of mode-matching and differential-equation techniques in the analysis of wave-guide transitions, *IEEE Transactions on Microwave Theory and Techniques*, 39 (2): 280-286, 1991.

[54] McGuire J. and Foucault J., Airworthiness Assurance Working Group, final report, Recommendations for regulatory action to prevent widespread fatigue damage in the commercial airplane fleet, 2002.

[55] Hurley D. C., Hedengren K. H., Howard P. J., Kornrumpf W. P., Sutton G. E. and Young J. D., Carburized case depth estimation by Rayleigh-wave backscattering, *Review of Progress in Quantitative Nondestructive Evaluation*, 13: 1111-1118, 1994.

[56] Smith R. A. and Harrison D. J., Hall sensor arrays for rapid large-area transient eddy current inspection, *Insight*, 46 (3): 142-146, 2004.

[57] Haned N. and Missous M., Nano-tesla magnetic field magnetometry using an InGaAs-AlGaAs-GaAs 2DEG Hall sensor, *Sensors and Actuators A: Physical*, 102 (3): 216-222, 2003.

[58] Van der Pauw L. J., A method of measuring specific resistivity and Hall effect of discs of arbitrary shape, *Philips Research Reports*, 13: 1-9, 1958.

[59] Decker M. R., GaAs and InAs Hall effect devices for nondestructive evaluation, *Master of Science, Iowa State University, Ames, Iowa*, 2003.

[60] Plummer J. D., Deal M. D. and Griffin P. B., Silicon VLSI Technology, Prentice Hall Inc., 510-512, 2000.

[61] Goldfine N., Zilberstein V., Shay I., Schlicker D., Windoloski M. and Washabaugh A., Multi-site damage imaging of 3rd layer crack in lapjoints using MWM-Arrays, *6th Joint FAA/DOD/NASA Aging Aircraft*, September 2002.

[62] InSb Hall element moel HW105A: data sheet, Asahi Kasei Electronics, http://www.asahi-kasei.co.jp/ake/en/ms/pdf/hw105a.pdf, 2004. (Last access date: December 10, 2004).

[63] GaAs Hall element model HG106C: data sheet, Asahi Kasei Electronics, http://www.asahi-kasei.co.jp/ake/en/ms/pdf/hg106c.pdf, 2004. (Last access date: December 10, 2004).

[64] Hall effect sensors catalog, F. W. Bell, http://www.sypris.com/library/documents/hallcatalog.pdf, 2004. (Last access date: December 10, 2004).

[65] Data sheet for P2 and P15A Hall sensors, obtained by private communication with Sly J. L., School of Electrical and Electronic Engineering, University of Manchester, Manchester, UK.

[66] Data sheet for monostable multivibrator 74HC123, htpp://www.fairchildsemi.com/ds/MM/MM74HC123A.pdf, 2005. (Last access date: Jan 18, 2005).

[67] Uesaka M., Hakuta K., Miya K., Aoki K. and Takahashi A., Eddy-current testing by flexible microloop magnetic sensor array, *IEEE Transactions on Magnetics*, 34 (4): 2287-2297, 1998.

[68] Smith R. A. and Harrison D. J., Hall sensor arrays for rapid large-area transient eddy current inspection, *Insight*, 46 (3), 2004.

[69] Schroder D. K., Semiconductor material and device characterization, second edition, 1998.

[70] Ward W. W. and Moulder J. C., Low frequency pulsed eddy currents for deep penetration, *Review of Progress in Quantitative Nondestructive Evaluation*, 17 (A): 291-298, 1998.

[71] Wincheski B. and Namkung M., Deep flaw detection with GMR based self nulling probe, *Review of Progress in Quantitative Nondestructive Evaluation*, 19 (A): 465-472, 2000.

[72] Smith R. A. and Hugo G. R., Transient eddy-current NDE for aging aircraft—capabilities and limitations, *Fourth Joint DoD/FAA/NASA Conference on Aging Aircraft*, May 2000.

[73] Burke S. K., Hugo G. R. and Harrison D. J., Transient eddy-current NDE for hidden corrosion in multilayer structure, *Review of Progress in Quantitative Nondestructive Evaluation*, 17 (A): 307-314, 1998.

[74] Bieber J. A., Tai C. C. and Moulder J. C., Quantitative assessment of corrosion in aircraft structures using scanning pulsed eddy current, *Review of Progress in Quantitative Nondestructive Evaluation*, 17 (A): 315-322, 1998.

[75] Moulder J. C., Kubovich M. W., Uzal E. and Rose J. H., Pulsed eddy-current measurements of corrosion-induced metal loss: theory and experiment, *Review of Progress in Quantitative Nondestructive Evaluation*, 14 (B): 2065-2072, 1995.

[76] Data sheet for AD633, Analog device, http://www.analog.com/UploadedFiles/DataSheets/277093686AD633e.pdf, 2005. (Last access date: Jan 14, 2005).

[77] Horowitz P., Hill W., The art of electronics, second edition, Cambridge University Press, 272-276, 1989.

[78] Sun H., Ali R., Johnson M. J. and Bowler J. R., Enhanced flaw detection using an eddy current probe with a linear array of hall sensors, *Review of Progress in Quantitative Nondestructive Evaluation*, Colorado, 2004.

ACKNOWLEDGEMENTS

I would like to thank my major adviser, professor John Bowler for leading me into electromagnetics and eddy current area, for his invaluable directions, encouragement and support throughout my PhD study. I'm grateful to Marcus Johnson for providing numerous suggestions and assistance on experiments. A special tribute is to Nicola Bowler for her guidance in ACPD method and studies of casehardened steel. I especially like to thank Marcus, Nicola and John for reading my dissertation and making valuable corrections and suggestions. I am indebted to Theodoros Theodoulidis, Greece, who answered a lot of my questions and helped solving difficult problems in calculating eigenvalues for the finite layered rod. I would like to thank Gary Tuttle for teaching me techniques and skills on semiconductor fabrications. I'm appreciative of suggestions from my committee members, Ronald Roberts and David Hsu. It is a pleasure to acknowledge Yongqiang Huang for his contribution in ACPD experiments, Raza Ali and Micah Decker for working together on the project of linear Hall array probe. Thanks are also due to a number of my colleagues, Fang-wei Fu, Vipul Katyal, Waqar Habib, Wei Zhang, Sanyi Zhan, Brent Eaton for discussions and spending time together in the same research group.

I would like to thank my parents and my husband for their supports and love, without which the completion of PhD study and dissertation is impossible. My husband helped me with some of the experiments and answered my questions whenever possible. He also proofread my dissertation.